Laser cooling of Yb on the intercombination line for experiments on localization of light

Álvaro Mitchell Galvão De Melo

Refroidissement laser de l'ytterbium sur la ligne d'intercombinaison pour des expériences sur la localisation de la lumière.

Álvaro Mitchell Galvão de Melo
Institut de Physique de Nice - INPHYNI

Présentée en vue de l'obtention du grade de docteur en Physique **d'** Université Côte d'Azur

Dirigée par : M. Robin Kaiser

Soutenue le : 19 juillet 2024

Devant le jury composé de :
Claus Zimmermann, Professeur, Universität Tübingen
Fabrice Mortessagne, Professeur, INPHYNI – Université Côte d'Azur
Lauriane Chomaz, Professeure, Universität Heidelberg
Leonardo Fallani, Professeur, Università degli Studi di Firenze
Robin Kaiser, Directeur de recherche CNRS, INPHYNI

European Research Council
Established by the European Commission

Refroidissement laser de l'ytterbium sur la ligne d'intercombinaison pour des expériences sur la localisation de la lumière.

Jury :

Rapporteurs

Lauriane Chomaz, Professeure, Universität Heidelberg
Leonardo Fallani, Professeur, Università degli Studi di Firenze

Examinateurs

Claus Zimmermann, Professeur, Universität Tübingen
Fabrice Mortessagne, Professeur, Université Côte d'Azur

Directeur de Thèse

Robin Kaiser, Directeur de Recherche, INPHYNI

Abstract

In this thesis, we study a magneto-optical trap (MOT) of ytterbium (Yb) atoms built to perform experiments aiming at observing the localization of light in three dimensions (3D). Anderson localization, i.e. the absence of diffusion due to disorder, was believed to be an ubiquitous wave phenomenon; however, recently, its mere existence for light waves is being questioned. The experimental observation of 3D localization of light has been intensively sought since the 1980s, and recently, cold atoms have emerged as promising samples to investigate it. Yb atoms are good candidates for the observation of localization effects due to the non-degenerate ground state for the bosonic isotopes and the linewidth of the $^1S_0 - {}^3P_1$ intercombination line (182 kHz), which is a good compromise between having negligible Doppler broadening and the possibility of performing time-resolved detection techniques.

We present a relatively compact experimental setup used to load up to 1×10^9 atoms in a MOT operating in the $^1S_0 - {}^1P_1$ transition without the use of a Zeeman slower. Particularly, the laser system that provides 2.5 W at 399 nm is discussed since high powers are needed due to the high saturation intensity of the transition. A detailed explanation of the system used to transfer up to 2×10^8 atoms from the MOT loaded in the $^1S_0 - {}^1P_1$ transition to the $^1S_0 - {}^3P_1$ transition is provided, with special attention to the setup used for laser frequency stabilization. We employ modulation transfer spectroscopy and balanced detection, enabling us to utilize a relatively weak yet convenient transition of molecular Iodine ($^{127}I_2$) as a frequency reference. We provide a characterization of the laser frequency stability, as well as of the $^{127}I_2$ line itself. A dense atomic cloud is obtained, which can be used to perform experiments on collective effects in cold atomic samples. Ideas for the optimization of the current setup in view of the observation of localization of light are discussed.

Finally, calculations of the position-dependent diffusion coefficient based on the self-consistent theory of localization are detailed for 2D systems. We compare the results obtained for different system sizes and disorder. These calculations will be used to study signatures of light localization in 2D, but they also pave the way for their extension into three dimensions, which could be used to interpret future experiments performed in the setup.

Keywords: cold atoms, laser frequency stabilization, molecular spectroscopy, Anderson localization.

Résumé

Dans cette thèse, nous étudions un piège magnéto-optique (MOT) d'atomes d'ytterbium (Yb) qui a été construit pour réaliser des expériences visant l'observation de la localisation de la lumière en trois dimensions (3D). La localisation d'Anderson, c'est-à-dire l'absence de diffusion due au disordre, était considéré comme un phénomène omniprésent, mais récemment son existence dans le cas des ondes lumineuses est remise en question. L'observation expérimentale de la localisation de la lumière en 3D a été intensément recherchée depuis les années 80 et récemment les atomes froids sont apparus comme des échantillons prometteurs pour l'étudier. Les atomes d'ytterbium sont bons candidats pour l'observation des effets de localisation en raison de leur état fondamental non dégénérés pour les isotopes bosoniques et la largeur de raie de la transition d'intercombinaison $^1S_0 - {}^3P_1$ (182 kHz) qui est un bon compromis entre un élargissement Doppler négligeable et la possibilité de recourir des techniques de détection résolues dans le temps.

Nous présentons une configuration expérimentale relativement compacte qui permet de charger jusqu'à 1×10^9 atomes dans un MOT fonctionnant sur la transition $^1S_0 - {}^1P_1$ sans utilisation d'un ralentisseur Zeeman. En particulier, le système laser qui fournit 2,5 W à 399 nm est discuté, car des puissances élevées sont nécessaires en raison de la forte intensité de saturation de la transition. Une explication détaillée du système pour transférer jusqu'à 2×10^8 atomes du MOT chargé sur la transition $^1S_0 - {}^1P_1$ vers la transition $^1S_0 - {}^3P_1$ est fournie, et une attention particulière est porté à la configuration utilisée pour la stabilisation de la fréquence laser. Nous employons la spectroscopie de transfert de modulation et détection équilibrée, nous permettant d'utiliser comme référence de fréquence une transition de l'iode moléculaire ($^{127}I_2$) relativement faible mais proche de la transition d'intercombinaison de l'ytterbium. Nous proposons une caractérisation de la stabilité de la fréquence du laser, ainsi que de la raie du $^{127}I_2$. Un nuage atomique dense et froid est obtenu, et peut être utilisé pour réaliser des expériences sur les effets collectifs dans des atomes froids. Des idées pour l'optimisation de la configuration actuelle en vue de l'observation de la localisation de la lumière sont discutés.

Enfin, des calculs du coefficient de diffusion dépendant de la position basés sur le la théorie auto-cohérente de la localisation sont détaillés pour les systèmes 2D. Nous comparons les résultats obtenus pour différentes tailles et désordres de systèmes. Ces calculs seront utilisés pour étudier les signatures de localisation de la lumière en 2D, mais ils ouvrent également la voie vers leur extension aux trois dimensions qui pourraient être utilisées pour interpréter les expériences futures.

Mots clés : atomes froids, stabilisation de fréquence laser, spectroscopie moléculaire, localisation d'Anderson.

Acknowledgements

I would like to begin by expressing my gratitude to those who directly contributed to this thesis. First, I extend my thanks to Robin Kaiser for entrusting me with this interesting project. His passion for science was a constant source of motivation, even during the most challenging phases of my work. I am also thankful to him for helping me connect with researchers around the world, either by recommending conferences or suggesting collaborations. I thank Raphaël Saint-Jalm for his invaluable support during the final year of this project, and for reviewing this manuscript. My sincere thanks go to the other members of the Yb team —Hector, Nahum, Apoorva, Antoine, Daniel, Anaïs, and Tristan— for their hard work throughout the experiment's construction, relocation, and operation.

I am particularly grateful to William Guerin, Mathilde Hugbart, and Guillaume Labeyrie for their constant assistance and attention. In addition to those mentioned above, I am thankful for the pleasant moments and coffee breaks shared with my colleagues at INPHYNI: Pierre A., Adrián, Jesús, Mateus, Stephan, Hamza, Pierre L., Nolan, Hodei, Ana, Alexis, Paolo, Pablo, Gianni, Antonin, Dilleys, Juan, Heitor, and Romain.

I would also like to acknowledge the support of the administrative, electronics, and IT teams at INPHYNI, especially Nathalie Hamel, François-Régis, Elvire Di Concetto, Sanaë Mahir, and Arnaud Dusaucy. I am equally grateful to the members of my thesis committee, Gian-Luca Lippi and Patrice Genevet, for their invaluable advice throughout different stages of my research. My thanks also go to the jury members for taking the time to evaluate this manuscript. I would also like to extend my gratitude to Romain Bachelard and João Vitor Ferreira for their collaboration on the theoretical aspects of this thesis, as well as to Sergey Skipetrov for welcoming me into his group in Grenoble for three weeks.

I am incredibly grateful to those who crossed the Atlantic to be with me during these past four years in France — my wife, Nathália, and my son, Benjamin - who made this journey unforgettable and were by my side through all the ups and downs. I also want to thank my family in Brazil for their constant support, especially my mother (Maria Antonieta), my father (Joaquim), and my brother (Jaime), who have been with me every step of the way.

To all my family and friends from Brazil, thank you for your encouragement and support, whether through visits to Antibes or at key moments in my academic career. I especially want to mention Mari, Cássia, José, Mateus, Diego, Danielle, Izabelle, and Cláudia.

Some of the figures included in this thesis utilize ComponentLibrary by Alexander Franzen, licensed under a Creative Commons Attribution-NonCommercial 3.0 Unported License, available at http://www.gwoptics.org/ComponentLibrary/.

Contents

Chapter 1

Introduction: towards 3D Anderson localization of light by cold atoms

1.1 Anderson localization

In 1958, Philip Anderson published his seminal paper "Absence of diffusion in certain random lattices" [1] in which he considered the diffusion of spins (or different particles) in a three dimensional lattice composed by sites that can be regularly or randomly distributed. If a particle occupies a site "i", then it has energy E_i. Anderson assumed that E_i is a stochastic variable with a probability distribution that is characterized by its width W. The transfer of the particles from one site (i) to another (j) is described by the interaction matrix element $V_{ij}(\mathbf{r_{ij}})$ (where $\mathbf{r_{ij}}$ is the distance between the two sites), which may be a stochastic variable with a probability distribution or not. We can write the Hamiltonian of the system as

$$\hat{H} = \sum_i E_i \left|i\right\rangle \left\langle i\right| + \sum_{i \neq j} V_{ij} \left|i\right\rangle \left\langle j\right| + c.c. \tag{1.1}$$

Anderson showed that if V (the average of V_{ij}) is smaller than a critical value V_c (of the order of magnitude of W) and it decays sufficiently fast, then transport does not occur. This phenomenon is nowadays known as Anderson localization. In summary, if the energy from site to site in the lattice varies randomly, at some conditions (spin) diffusion can vanish and a conductor to insulator transition is observed. Moreover, he showed that the wavefunctions can be localized in a small region of the space. In the context of disorder-induced localization of propagating classical waves, the "Ioffe-Regel criterion" is commonly used as the standard benchmark to determine the possibility for observing localization phenomena. [2]. The criterion assumes that if the mean free path l due to the scattering of a wave in a medium is of the order of its wavelength λ then the field does not perform one oscillation before that the wave is scattered. Then, another kind of transport, other then diffusive, may occur. We can summarize the criterion as $(kl)_c \approx 1$, where $(kl)_c$ is the value of kl at which a transition from conductor to insulator would occur.

Since its proposal, Anderson localization in three dimensions (3D) has been intensively sought for different types of waves. It has been observed for ultrasound [3] and matter-waves [4, 5]. For matter-waves, localized states analogous to 3D Anderson localization were also reported [6,7]. However, an indisputable experimental evidence of Anderson localization of light in three dimensions has not been reported so far. In one and two dimensions the situation is different, no phase-transition is expected to occur with all states being localized in 1D. In 2D all states can be localized provided that the system is large enough [8].

1.2 3D Anderson localization of light

Only in 1984 a theoretical study of Anderson localization of light was reported by Sajeev John [9]. The author argued that since a plane-polarized electromagnetic wave would lose its initial polarization due to multiple scattering, the scalar wave equation could be considered, neglecting the vectorial nature of light. Indeed, it was shown that by considering randomly distributed spheres, a regime where the Ioffe-Regel criterion is fulfilled could be achieved. Assuming that the disorder of the system can be varied, a rise in the absorption of light would arise as the energy that separates localized to extended states, known as the mobility edge, is approached from the diffusive to the localized regime. In 1985, Philip Anderson has also reported a study on localization of classical waves (such as microwave, acoustic, or light) [10]. The conclusion of Anderson's work is in agreement with John's in the sense that it should be possible to observe localization of classical waves, indeed Anderson stated that

> "In conclusion, I feel that localization in classical wave propagation is a phenomenon which should, in carefully prepared systems, be easily observed, and in such systems the basic laws of the localization phenomena could be conveniently studied, for example, the critical exponents and the phenomenon of anomalous fluctuations. In addition, although great complexity may be encountered, the work may impinge on a number of highly interesting and practical systems, such as paints, porous media, etc." Anderson, Philip [10].

However, differently from John's work, Anderson predicted a decrease of the absorption near the mobility edge. Despite their conclusions, indisputable experimental evidence of this phenomenon has not been reported since then.

The observation of Anderson localization of light in 3D was claimed in experimental works that were very important to the understanding of the phenomenon and its particularities with respect to other kind of waves. In [11], Wiersma *et al.* reported experiments performed on semiconductor powders (GaAs) where they prepared samples with kl values ranging from 76 down to 1.5 (a record at that time for optics). For diffusive light transport, the analogous of Ohm's law holds for photons,

i.e. the transmission of a light beam through the sample decreases linearly with the system size. At the transition from diffusion to localization it was expected that the transmission of the light (T) decreases as $\frac{1}{L^2}$, where L is the system's size; and for the localized case, the transmission coefficient decreases exponentially with the system size. The authors observed these behaviour in the experiments and then they reported the results as signatures of localization of light in 3D. However, their interpretation of the experimental results was questioned by Scheffold *et al*. in [12]. Scheffold *et al.* indicated that the the data shown by Wiersma *et al.* could be interpreted by considering light diffusion in the presence of absorption. The debate ended only 15 years after the publication of the results of Wiersma *et al.* in [13], when the authors showed that indeed absorption was playing an important role in the experiments performed with GaAs.

In 2006, the observation of a critical regime (near to Anderson localization) in TiO_2 samples was claimed by Störzer *et al.* [14]. The authors performed time-dependent measurements of the transmission of a laser pulse through TiO_2 samples for different values of (kl). They observed that for high kl the measurements indicate diffusive transport (exponential decay of light transmission at long times), but for low values of kl the measurements did not show a diffusive behaviour. The deviations could be explained by a time-dependent diffusion coefficient inside the sample, which is in agreement with theoretical prediction for light transport near the mobility edge presented in [15]. Additionally, in [16], direct evidence for localization of light in 3D and the localization transition was reported. The authors studied the propagation of optical pulses through the sample. They looked at the spread (in time) of the transverse width of this pulse. In the presence of localization effects the width is expected to linearly increase with time, until it reaches a plateau, which was exactly what was observed. Again, the results were questioned by Scheffold *et al.* [17] that argued that the evidences of localization reported in [14, 16] could be due to inelastic scattering of light. Indeed, it was concluded in [18] that a consequence of fluorescence was being observed in TiO_2 and not localization of light.

We can conclude that experimental observation of Anderson localization of light in three dimensions is still an open problem. However, recently, its mere existence was questioned. Skipetrov *et al.* [19] showed that Anderson localization of light could not be achieved in a random three dimensional ensemble of point scatters, which is the model used for ensembles of cold atoms. The authors' results led to the presence of localization only when the vectorial character of light was not considered (scalar approximation), which was not in disagreement with the first theoretical results on this subject [9,10]. However, the authors concluded that the vectorial nature of light alongside dipole-dipole interactions prevents localization effects.

1.3 State of the art

A way to circumvent the issue pointed out in [19] was proposed by the same authors in [20]. They have shown that the application of a static magnetic field on an atomic system where the relevant optical transition is composed by a ground state with total angular momentum $J_g = 0$ and an excited state with total angular momentum $J_e = 1$, could lead to a transition to a localized regime. In [21], Sergey Skipetrov calculated the number density of atoms (ρ) at which this transition occurs ($\rho = 0.1k^3$). This leads to a critical density for the $^1S_0 - {}^3P_1$ Yb transition of

$$\rho_{c,Yb} = 1.4 \times 10^{14}\,\text{atoms}\,\text{cm}^{-3}. \tag{1.2}$$

Besides achieving such high densities, a bias field of the order of 100 G should be applied. Attention should be paid to the temporal control of this bias field (which should not perturb the loading of the magneto-optical trap) and to the induction of eddy currents in the (metallic) structure that composes the vacuum system.

Inspired by the original Anderson model eq. (1.1), Celardo *et al.* [22] showed that a new type of localization arises in cold atomic systems in the presence of positional and diagonal disorder. Diagonal disorder is exactly what is assumed in eq. (1.1), i.e. disorder on the atomic energy levels. The implementation of diagonal disorder can be made by applying a laser beam with a randomly distributed intensity profile. The beam would couple two atomic transitions and by adjusting frequency and intensity, a randomly distributed light-shift would mimic the diagonal disorder of eq. (1.1).

1.4 The choice of ytterbium atoms

Cold atoms are promising samples to study localization of light. The lack of absorption of light in cold atomic samples is an advantage with respect to other kind of samples [13]. The simplicity of the discrete energy levels allows a control of nonlinear effects in comparison to materials whose energy bands are complicated and depend on the sample's manufacturing [18]. Theoretical proposals for the observation of localization in cold atomic samples are also available [20, 22]. However, the choice of the atomic species to be used is indeed critical. Cold atoms experiments tend to be expensive due to the need of narrow linewidth lasers and ultra-high vacuum (UHV) material. Once the experiment is built, it is not easy to adapt it to a different atomic species, due to the use of diode lasers which are only tunable by a few units of nm and also the UHV system as well.

Choosing the appropriate atomic species from the outset is crucial, as the characteristics of an atom (such as the energy of optical transitions and magnetic properties) determine its suitability for a specific application. One important feature to be considered is the atomic structure. The first group of chemical elements to be laser cooled and trapped by magneto-optical traps (see chapter 3) were alkali metals, namely rubidium (Rb), cesium (Cs), sodium (Na), potassium (K) and lithium

(Li). These elements have similar chemical properties because they have an unpaired valence electron in a S-orbital. The energy needed to excite these atoms (stimulate a transition of the valence electron to a higher sub-shell) matches the energy provided by the light emitted by the first types of diode lasers, which emitted light in the near-infrared [23]. Magneto-optical traps (MOTs) of alkali metals are, therefore, easily obtainable in comparison to atoms of other groups of the periodic table, and cheaper due to the need of less lasers. The good quantum number for the description of these atoms is $F = J + I$, where I is the nuclear angular momentum quantum number and J is the total electron quantum number, which is the sum of the electron angular orbital momentum (L) and the electron spin angular momentum (S). For example, for ^{87}Rb ground state F can be either 1 or 2. Each energy level has $2F + 1$ magnetic (Zeeman) sublevels. However, Zeeman sublevels of the ground states of optically available transitions are not considered in the theoretical proposals for localization of light by cold atoms. A relatively complex atomic internal structure could turn the analysis of experimental results difficult.

Therefore, the use of alkaline earth metals is envisaged. The bosonic isotopes of these metals, including strontium (Sr), calcium (Ca), beryllium (Be), magnesium (Mg), barium (Ba), and radium (Ra), exhibit a level structure consisting of a nondegenerate ground state and a threefold degenerate excited state for the cooling transitions. This relatively simpler level structure was taken into account in the theoretical proposals for magnetic-field-driven localization [20, 21] and localization due to position and diagonal disorder [22]. Additionally, MOTs of five out of the six alkaline earth metals have already been realized [24–28]. These elements have two laser cooling transitions, namely the transition from the ground to a singlet state $^1S_0 - {}^1P_1$ and an intercombination transition $^1S_0 - {}^3P_1$.

The $^1S_0 - {}^1P_1$ transitions have broad linewidths (tens of MHz), while laser cooling of alkaline earth metals in the $^1S_0 - {}^3P_1$ transition remains a challenge, the usual choice is Sr, which has a linewidth of $2\pi{\cdot}7\,$kHz. Therefore, the choice of Sr can look promising, because the density of the atomic cloud loaded by a MOT is inversely proportional to the square of the linewidth of the transition (see chapter 3). However, a major issue is that the natural linewidth of the transition is of the order of the corresponding recoil frequency. For example, Sr has a natural linewidth of the order of the recoil frequency [29]. Therefore, single photon scattering would already drive the photons out of resonance to the atomic transition. A solution is the use of ytterbium (Yb), which - although it is a lanthanide - has an electronic structure similar to the alkaline earth metals. The bosonic isotopes of Yb have a nondegenerate ground state and a three-folded degenerate excited state and the natural linewidth of its $^1S_0 - {}^3P_1$ transition is $\Gamma_g = 2\pi{\cdot}182\,$kHz. This linewidth is a good compromise to achieve robust laser frequency stabilization and neglect atomic recoil effects. MOTs operating on the $^1S_0 - {}^1P_1$ transitions have not been considered for localization experiments because the fast decay time of the excited state, of the order of 10 ns, makes the realization of time-dependent measurements difficult.

In fig. 1.1, a simplified energy level diagram is shown with relevant quantities. The $^3P_1 - {}^3D_1$ transition that is shown will only be discussed in chapter 6. Ytterbium has five bosonic isotopes (^{168}Yb, ^{170}Yb, ^{172}Yb, ^{174}Yb, and ^{176}Yb). We have decided to trap the ^{174}Yb isotope, because it is the most naturally abundant (the natural abundance is 31.8%). A table with certain relevant characteristics for laser cooling of Yb is shown in table 1.1. The values shown in the table are valid for all Yb isotopes, small differences due to isotope shifts are small for the purposes of this thesis and are neglected.

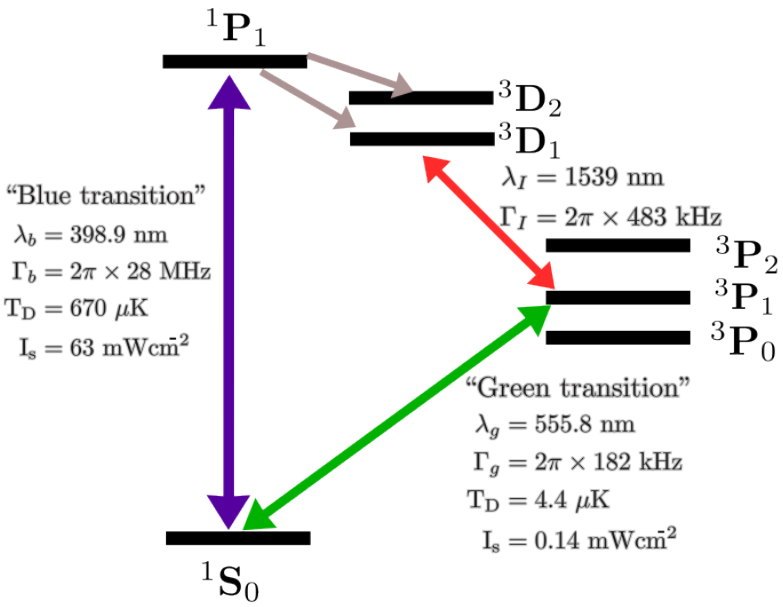

FIGURE 1.1: Simplified energy level diagram of neutral Yb. The wavelengths and linewidths of the two cooling transitions and the $^3P_1 - {}^3D_1$ transition are shown, alongside the saturation intensity (I_{sat}) and the Doppler temperature T_D for the cooling transitions. The values were taken from [30, 31]

.

	Blue transition	Green transition	
v_r	5.7 mm s^{-1}	4.1 mm s^{-1}	recoil velocity ($\frac{\hbar k}{M}$)
$\frac{\omega_r}{2\pi}$	7.5 kHz	3.7 kHz	recoil frequency ($\frac{v_r k}{4\pi}$)
a_{max}	5.2×10^5 m s^{-2}	2.3×10^3 m s^{-2}	maximum atomic deceleration ($\frac{v_r \Gamma}{2}$)
g_L	1.035	1.493	Landé factor of the excited state

TABLE 1.1: Recoil velocity, recoil frequency, maximum atomic deceleration and the Landé factor of the excited states for the two cooling transitions for neutral ytterbium atoms.

It is important to emphasize that this thesis was developed in parallel to another one. Hector Letellier started his thesis three months before me in the same project. Therefore, the work of building the experiment was split in two and both thesis have

different content. The present thesis is focused on the laser systems and on the MOT obtained in the $^1S_0 - {}^3P_1$ by transferring from the $^1S_0 - {}^1P_1$ transition (blue MOT), while his thesis is focused on a characterization and optimization of the blue MOT itself, alongside details on the MOT apparatus (vacuum system, atomic beam, time control of the experiment, etc.). Additionally, theoretical results based on the self-consistent theory of localization are also discussed in the end of the present thesis. The results will be used to study signatures of localization of light in 2D, but an adaptation of the calculations for 3D is also envisaged. The Yb MOT described in this thesis will be used to perform experiments aiming at the observation of localization of light in 3D.

1.5 Thesis outlook

In **chapter 2**, four different laser frequency stabilization techniques are discussed. Two of them are used to stabilize the laser frequency to a stable optical cavity (Pound-Drever-Hall and Hänsch-Couillaud techniques) and the other two are used for laser frequency stabilization to an atomic (or molecular) resonance (frequency modulation spectroscopy and modulation transfer spectroscopy). These techniques were important during this thesis work because during the conception of the experiment, we had to reflect on which technique to use to stabilize the frequency of the lasers. Additionally, the two main lasers used in the experiment have second-harmonic generation cavities that are stabilized by two different methods. The optimization of the lasers was frequently made by myself due to the lack of personal assistance of the manufacturers due to the COVID pandemic, and additionally due to adversities imposed by the moving of the laboratory to a new building. Therefore, understanding these techniques was necessary for the construction and operation of the experiment. Additionally, a derivation of the signal generated by modulation transfer spectroscopy is included. The motivation was the absence of this calculation in recently published material.

Chapter 3 is an introduction to the experimental apparatus. The chapter starts by introducing important features of laser cooling that justify decisions made for the experiment. One of these decisions was the loading of a MOT on the $^1S_0 - {}^1P_1$ transition and the subsequent transfer to the $^1S_0 - {}^3P_1$ transition. The laser system used to trap atoms on the $^1S_0 - {}^1P_1$ transition is described, including its optimization. Finally, it is shown a MOT loaded in the $^1S_0 - {}^1P_1$ transition with up to 1×10^9 atoms and with a loading rate of 3×10^9 atoms s^{-1}.

The transfer of 2×10^8 atoms to a MOT operating in the $^1S_0 - {}^3P_1$ transition is described in **chapter 4**. The laser system is also introduced, with special attention to the laser frequency stabilization. Modulation transfer spectroscopy and balanced detection of a relatively weak molecular iodine line is shown, alongside details of the chosen line. This simple technique can be useful not only for Yb atoms, but

whenever a relatively weak line is chosen as frequency reference. A characterization of the MOT is performed by employing the absorption imaging technique.

Chapter 5 introduces the calculation of a position-dependent diffusion coefficient in 2D. The calculations are based in the self-consistent theory of localization and it was already performed for infinitely large 3D systems and quasi-1D systems. The goal of this theory is to calculate signatures of localization.

Chapter 2

Laser frequency stabilization techniques

The main goal of the thesis was to build a magneto-optical trap of ytterbium atoms operating on the ${}^1S_0 - {}^3P_1$ transition. During the construction of the experiment, I had to perform and optimize different laser frequency stabilization schemes. In our experiment, two lasers have second-harmonic generation (SHG) cavities. One of this cavities is stabilized by the Pound-Drever Hall method, while the other one by the Hänsch-Couillaud technique. Although these are commercial cavities, they had to be installed and re-optimized during the thesis work. Therefore, it was mandatory to understand these techniques for the building and maintenance of the experiment.

Two techniques based on the spectroscopy of atomic or molecular transitions are also covered in this chapter. Frequency modulated spectroscopy can be seen as the analogous of the Pound-Drever Hall technique. It is also the precursor of modulation transfer spectroscopy, which was the technique chosen to stabilize the laser that is used to perform a magneto-optical trap of ytterbium in the ${}^1S_0 - {}^3P_1$ transition, as will be shown in chapter 4.

This chapter exposes simple experimental configurations for the implementation of each of these four techniques and shows how the error signals are generated for all of them. The literature on laser frequency stabilization techniques is vast, but a summary and a comparison of these four techniques can be valuable for people that will enroll in this project in the near future, as well as for the ones that will build similar experiments.

2.1 Pound-Drever-Hall

Pound-Drever-Hall (PDH) is a laser frequency stabilization technique that was proposed and demonstrated by Drever and Hall in 1983 [34] based on a previously known technique of frequency stabilization of microwave oscillators developed by Pound in 1946 [35]. Such a technique consists in modulating the phase or frequency (see appendix A) of the laser field incident on a cavity and measure the cavity reflection. The retrieved error signal can be used for stabilization of the laser frequency, assuming that the cavity is stable enough.

Another application is the use of this technique for cavity stabilization, using the laser as a reference. This is widely used to stabilize second-harmonic generation (SHG) cavities and is one of the methods used for cavity stabilization used in this work. PDH was, for example, used to stabilize the interferometers used for gravitational wave detection [36] due to its capacity to suppress frequency noise.

2.1.1 Experimental setup

The basic experimental scheme of the PDH technique is shown in fig. 2.1. The linearly polarized laser field is phase-modulated by an electro-optic modulator (EOM). The beam polarization is chosen so that it is transmitted by a polarizing beamsplitter (PBS) cube, and a quarter-wave ($\frac{\lambda}{4}$) plate is inserted between the PBS and the cavity so that the light reflected by the cavity is measured by a photodiode (PD_{refl}). The signal generated by PD_{refl} is sent to the radiofrequency (RF) input of a RF mixer, while the signal used to generate the modulation (after adjusting its phase) is sent to the local-oscillator (LO) port of the RF mixer. The frequency of a diode laser generally can be controlled by the voltage applied to a piezoelectric actuator that holds the laser grating or by the current that is applied to the diode (assuming that the temperature of the diode is kept constant). Tuning the frequency by the diode's current is faster than by the voltage applied to the piezo. Therefore, the output of the mixer passes through a lowpass filter before a PID controller that is used to send a feedback to the laser current controller and a function generator scan the laser frequency sending a triangular signal to the piezo controller.

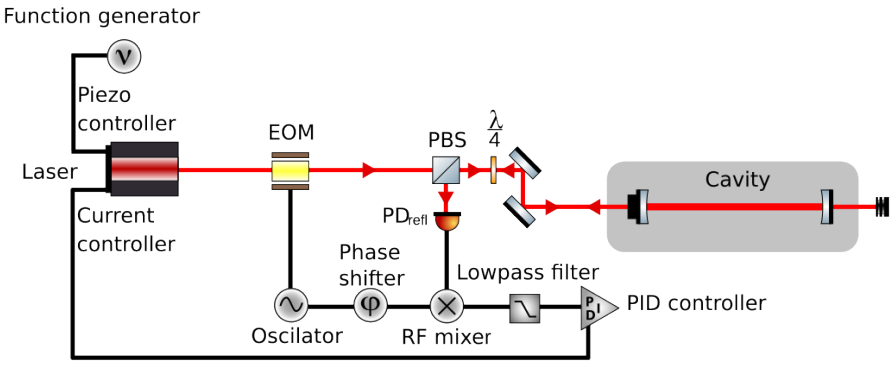

FIGURE 2.1: Simplified experimental scheme for laser frequency stabilization by PDH technique. A linearly polarized laser beam is phase modulated by an electro-optic modulator (EOM) and transmitted through the PBS. A quarter-wave plate is inserted after the PBS so that the light reflected from the cavity is also reflected by the PBS to the photodiode (PD_{refl}). The signal is demodulated by the RF mixer and sent to a lowpass filter before a proportional-integral-derivative (PID) controller and fed back to laser's current controller. A function generator scans the laser frequency by controlling the tension applied to a piezoelectric actuator that holds the laser grating.

2.1.2 Derivation of the error signal

The goal of this section is to show how the error signals are generated by the PDH method, a more complete review on PDH laser frequency stabilization can be found in [37]. It will be assumed that a phase modulated laser field is incident into a cavity, and the power measured on the reflection of the cavity will be calculated to retrieve the error signal, by demodulation, from the remaining terms that oscillate at the modulation frequency. Let's assume the incident laser field is represented as $E_{inc} = E_0 e^{i\omega t}$. The reflected field (measured at the same point) is given by $E_{ref} = E_1 e^{i\omega t}$ and both fields are linked by the cavity reflection coefficient $F(\omega) = \frac{E_{ref}}{E_{inc}}$. After passing through a phase modulator (e.g. Pockels cell), the incident electric field becomes

$$E_{inc} = E_0 e^{i(\omega t + \beta \sin \delta t)}, \tag{2.1}$$

where δ is the modulation frequency and β the modulation depth. we can expand eq. (2.1) in terms of Bessel functions (J_n)

$$E_{inc} = E_0 \sum_{n=-\infty}^{\infty} J_n(\beta) e^{in\delta t + \omega t}. \tag{2.2}$$

For $\beta \ll 1$ (i.e. narrowband modulation), the terms $n > 1$ in eq. (2.2) are much smaller than the others, so we neglect them. Then, the incident field can be written as

$$E_{inc} = E_0[J_0(\beta) e^{i(\omega t)} + J_1(\beta) e^{i(\omega+\delta)t} - J_1(\beta) e^{i(\omega-\delta)t}]. \tag{2.3}$$

Therefore, the incident field can be treated as three different fields of different frequencies (one carrier and two sidebands), and to calculate the reflected field we will multiply each term by the reflection coefficient at its own frequency.

$$E_{ref} = E_0[F(\omega) J_0(\beta) e^{i(\omega t)} + F(\omega+\delta) J_1(\beta) e^{i(\omega+\delta)t} - F(\omega-\delta) J_1(\beta) e^{i(\omega-\delta)t}]. \tag{2.4}$$

But, what we measure is the power of the reflected laser beam($P_{ref} = |E_{ref}|^2$) given by

$$\begin{aligned} P_{ref} =& P_0\{|F(\omega)|^2 |J_0(\beta)|^2 + |F(\omega+\delta)|^2 |J_1(\beta)|^2 - |F(\omega-\delta)|^2 |J_1(\beta)|^2 \\ &+ 2J_0(\beta) J_1(\beta)\, \mathrm{Re}[R(\omega)] \cos\delta t + 2J_0(\beta) J_1(\beta)\, \mathrm{Im}[R(\omega)] \sin\delta t \\ &- 2|J_1(\beta)|^2\, \mathrm{Re}[F(\omega+\delta) F^*(\omega-\delta)] \cos 2\delta t \\ &+ 2|J_1(\beta)|^2\, \mathrm{Im}[F(\omega+\delta) F^*(\omega-\delta)] \sin 2\delta t\}, \end{aligned} \tag{2.5}$$

where P_0 is the initial beam power,

$$R(\omega) = F(\omega) F^*(\omega+\delta) - F^*(\omega) F(\omega-\delta) \tag{2.6}$$

is called the **readout function** and $\mathrm{Re}[R(\omega)]$ and $\mathrm{Im}[R(\omega)]$ denote, respectively, the

real and imaginary parts of $R(\omega)$, and the superscript * denotes the complex conjugate.

In order to obtain the desired error signal one should retrieve the readout function (terms that oscillates at frequency δ). This will be done assuming that the reflection coefficient (r) for both cavity mirrors are the same, so that

$$F(\omega) = -\frac{r(1 - e^{\frac{i\omega}{\Delta_{fsr}}})}{1 - r^2 e^{\frac{-i\omega}{\Delta_{fsr}}}}. \tag{2.7}$$

The cavity linewidth (Γ) is related to the cavity free spectral range (Δ_{fsr}) by $\Delta_{fsr} = \Gamma\mathcal{F}$, where $\mathcal{F}$ is the cavity finesse. $\mathrm{Re}[R(\omega)]$ and $\mathrm{Im}[R(\omega)]$ are shown in fig. 2.2 for three different modulation frequencies ($\delta = 0.1\Gamma, \Gamma, 10\Gamma$). Although both real and imaginary parts of $R(\omega)$ have similar lineshapes, their amplitude depends on the modulation frequency (δ). For small frequency modulation ($\delta \ll \Gamma$) the amplitude of $\mathrm{Re}[R(\omega)]$ is higher than $\mathrm{Im}[R(\omega)]$, defining which term should be retrieved by demodulation from eq. (2.5). If the modulation frequency is of the order of the cavity linewidth ($\delta \approx \Gamma$), $\mathrm{Re}[R(\omega)]$ and $\mathrm{Im}[R(\omega)]$ have similar amplitudes as shown in fig. 2.2b. When $\delta \gg \Gamma$, the central dispersive signal of $\mathrm{Im}[R(\omega)]$ has a larger amplitude than the one of $\mathrm{Re}[R(\omega)]$. Therefore, for large values of δ, $\mathrm{Im}[R(\omega)]$ is the best error signal. Moreover, the wings of $\mathrm{Im}[R(\omega)]$ shown in fig. 2.2c provides a better capture range (i.e. the maximum deviation in frequency that the laser can experience with respect to the reference cavity that can be compensated by the stabilization feedback loop) than can be achieved with slow modulation, emphasizing the advantage of faster modulation frequencies over slow ones in addition to a larger amplitude of the error signal itself.

2.1.3 PDH cavity stabilization

One important application of the PDH technique is that it can be used to stabilize an optical cavity to the laser frequency. This can be done, for example, to enhance second-harmonic generation (SHG) by inserting a crystal inside a cavity. Such a method is used in the present work to generate up to 1.3 W at 556 nm for laser cooling of ^{174}Yb , more details on this laser system are given in chapter 4. A typical experimental scheme is shown in fig. 2.3. The laser frequency modulation is performed by modulation of the laser current, and the reflection of the cavity is measured by PD_{refl}. After the demodulation, the error signal is sent to a PID controller and the feedback is sent to a piezoelectric that actuates on one mirror of the cavity.

2.2 Hänsch-Couillaud

A modulation-free technique for laser frequency stabilization to an optical cavity was reported by T. Hänsch and B. Couillaud in 1980 [38]. In the so-called "Hänsch-Couillaud technique" the reflection of a linearly polarized laser beam by a cavity is

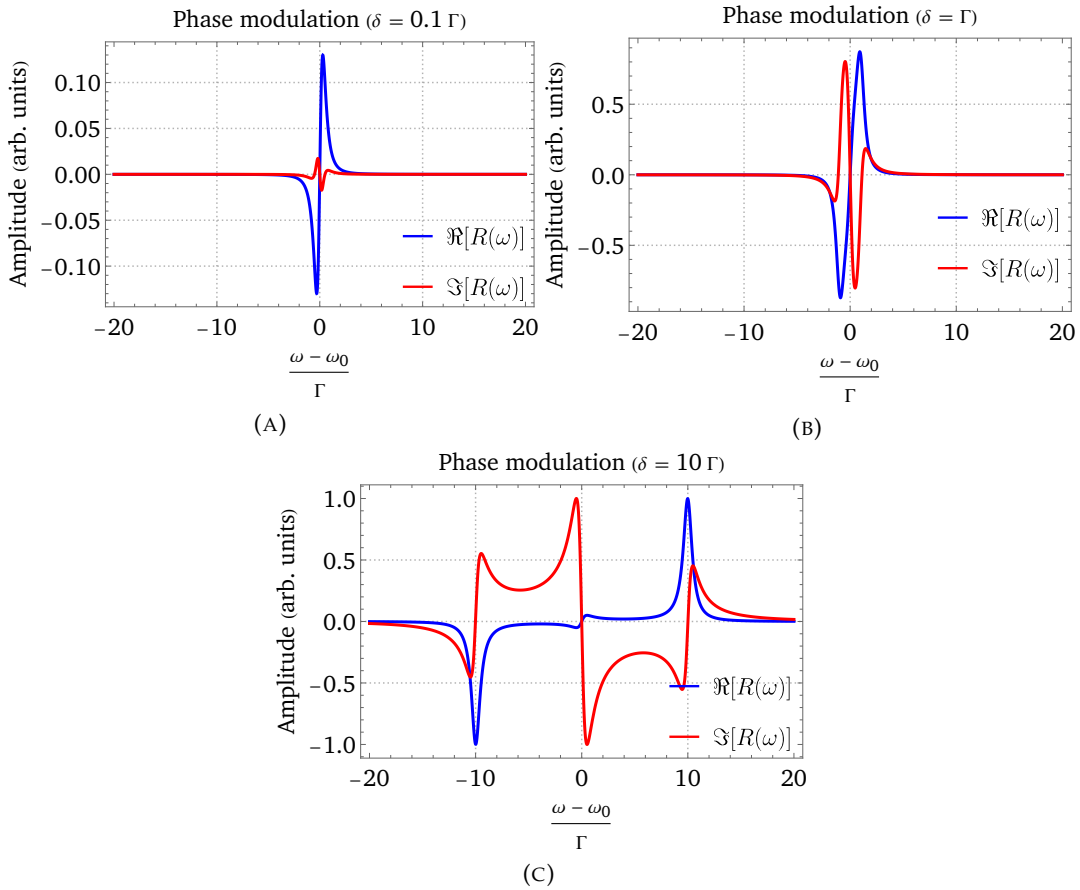

FIGURE 2.2: Real and imaginary part of the readout function for different values of δ.

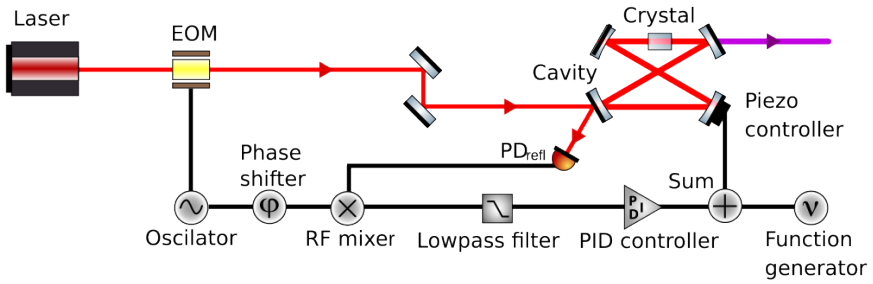

FIGURE 2.3: Simplified experimental scheme for stabilization of a bow-tie cavity by PDH technique.

measured, while a linear polarizer is placed inside the cavity. Phase variations of the light component that is parallel to the axis of the linear polarizer are measured by a polarization analyzer, that generates the error signal used for laser stabilization.

Hänsch-Couillaud technique is widely used for laser frequency stabilization, as well as for the stabilization of SHG cavities. Its advantage over techniques based on frequency modulation, lies on its simple electronics and in the achievement of an

error signal that remains strong in its wings, leading to a good capture range without the need of high frequency modulation of the laser.

2.2.1 Experimental setup

The experimental setup for Hänsch-Couillaud frequency stabilization is shown in fig. 2.4. In this scheme, a linearly polarized laser beam is reflected by a bow-tie cavity (it can be performed with a confocal Fabry-Perot cavity). A linear polarizer is inserted inside the cavity, so that the polarization of the electric field can be decomposed in one component parallel to the axis of the linear polarizer ($E_{\parallel}$) and other perpendicular to it ($E_{\perp}$). Therefore, $E_{\parallel}$ experiences a low-loss cavity and it is reflected by the cavity with a frequency-dependent phase shift. A polarization analyzer is used to analyze the light reflected by the first mirror and the cavity. The analyzer is composed by a $\frac{\lambda}{4}$ plate, a PBS cube and two photodiodes (PD+ and PD-). In this method the $E_{\perp}$ component reflected by the first mirror acts as a reference and the total reflected beam becomes elliptically polarized due to any phase change of $E_{\parallel}$. The intensities measured by the two photodetectors are subtracted and amplified, to generate the error signal, before been sent as a feedback to control laser frequency fluctuations. The details on the generation of the error signal are given below.

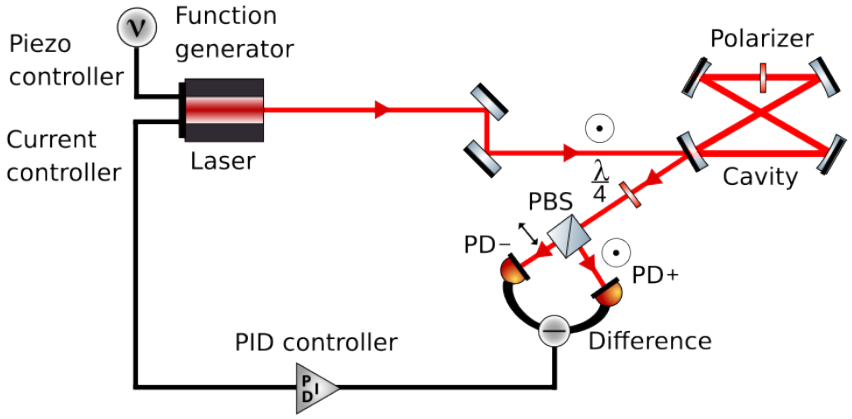

FIGURE 2.4: Simplified experimental scheme for laser frequency stabilization by the Hänsch-Couillaud technique.

2.2.2 Derivation of the error signal

In order to show how the error signal is generated by the Hänsch-Couillaud method, the calculations presented in [38] are detailed here. The incident light field amplitudes are described in the plane wave approximation as

$$E^i_{\parallel} = E^i \cos\theta, \tag{2.8}$$

$$E^i_{\perp} = E^i \sin\theta. \tag{2.9}$$

E^i is the amplitude of the incident beam. The amplitude of the perpendicular component that is reflected by the cavity is given by

$$E^r_\perp = E^i_\perp \sqrt{R_1}, \tag{2.10}$$

where R_1 is the reflectance of the first mirror. The amplitude of the parallel component is given by a sum of its component that is reflected by the first cavity mirror and the reflection of the cavity, as follows

$$E^r_\parallel = E^i_\parallel \left[\sqrt{R_1} - \left(T_1 \frac{R}{\sqrt{R_1}} e^{i\Delta} + T_1 \frac{R}{\sqrt{R_1}} R e^{2i\Delta} + ... \right) \right], \tag{2.11}$$

where T_1 is the transmittance of the first mirror. R represents the ratio of the amplitude between successive roundtrips, taking into account all of the sources of losses (both mirrors + linear polarizer). The first term on the right side of eq. (2.11) represents the field reflected by the first mirror with polarization parallel to the axis of the intracavity polarizer. The right part of eq. (2.11) represents the field reflected by the cavity, which is a geometric series with coefficient $T_1 \frac{R}{\sqrt{R_1}} e^{i\Delta}$ and ratio $Re^{i\Delta}$. The whole expression can be written as

$$E^r_\parallel = E^i_\parallel \left[\sqrt{R_1} - T_1 \frac{R}{\sqrt{R_1}} \left(\frac{e^{i\Delta}}{1 - Re^{i\Delta}} \right) \right]. \tag{2.12}$$

By multiplying the right side of the equation by $\frac{1-e^{-i\Delta}R}{1-e^{-i\Delta}R}$ and making use of the identity $\cos 2\Delta = 1 - 2\sin^2 \Delta$, it becomes

$$E^r_\parallel = E^i_\parallel \left[\sqrt{R_1} - T_1 \frac{R}{\sqrt{R_1}} \left(\frac{\cos\Delta - R + i\sin\Delta}{(1-R)^2 + 4R\sin^2 \frac{\Delta}{2}} \right) \right]. \tag{2.13}$$

If the field is at resonance with the cavity, then $\sin\Delta = 0$ and the total field is linearly polarized. However, out of resonance ($\sin\Delta \neq 0$) the phase shift of $E^r_\parallel$ with respect to $E^r_\perp$ makes the total reflected beam elliptically polarized. The polarization analyzer consists in a $\frac{\lambda}{4}$ waveplate and a PBS cube. The axis of the $\frac{\lambda}{4}$ waveplate is rotated by 45° with respect to the axis defined by the light polarization after reflection from the PBS. The whole analyzer could be rotated with respect to the direction of propagation of the beam, however the calculation shown here is performed for the case at which the axis of the $\frac{\lambda}{4}$ waveplate is parallel to the axis of the linear polarizer inside the cavity. To better understand the role of the analyzer, we make use of the Jones formalism [39] and consider the light incident to the $\frac{\lambda}{4}$ waveplate as a superposition of two circularly polarized light. Circularly polarized light will be denoted here as E_{σ_+} for right-handed and E_{σ_-} for left-handed. The field is written in the basis defined by linearly polarized light parallel and perpendicular to the intracavity polarizer as follows

$$E^r = A \begin{pmatrix} 1 \\ -i \end{pmatrix} + B \begin{pmatrix} 1 \\ i \end{pmatrix}, \tag{2.14}$$

where A and B represent the amplitude of E_{σ_+} and E_{σ_-}, respectively. After passing through the $\frac{\lambda}{4}$ waveplate, these components are transformed into two linearly polarized components that are orthogonal to each other, and the total field can be calculated by

$$E^r_{\frac{\lambda}{4}} = \frac{e^{i\frac{\pi}{4}}}{2}\begin{pmatrix}1 & 0\\ 0 & i\end{pmatrix}\left[A\begin{pmatrix}1\\ -i\end{pmatrix} + B\begin{pmatrix}1\\ i\end{pmatrix}\right], \tag{2.15}$$

which results in

$$E^r_{\frac{\lambda}{4}} = \frac{e^{i\frac{\pi}{4}}}{2}\left[A\begin{pmatrix}1\\ 1\end{pmatrix} + B\begin{pmatrix}1\\ -1\end{pmatrix}\right]. \tag{2.16}$$

Hence, the reflection of the PBS cube is given by

$$E_+ = \frac{e^{i\frac{\pi}{4}}}{2}\begin{pmatrix}1 & 1\\ 1 & 1\end{pmatrix}\left[A\begin{pmatrix}1\\ 1\end{pmatrix} + B\begin{pmatrix}1\\ -1\end{pmatrix}\right] = \frac{e^{i\frac{\pi}{4}}}{2}\left[A\begin{pmatrix}2\\ 2\end{pmatrix} + B\begin{pmatrix}0\\ 0\end{pmatrix}\right]. \tag{2.17}$$

While the transmission of the PBS cube is

$$E_- = \frac{e^{i\frac{\pi}{4}}}{2}\begin{pmatrix}1 & -1\\ -1 & 1\end{pmatrix}\left[A\begin{pmatrix}1\\ 1\end{pmatrix} + B\begin{pmatrix}1\\ -1\end{pmatrix}\right] = \frac{e^{i\frac{\pi}{4}}}{2}\left[A\begin{pmatrix}0\\ 0\end{pmatrix} + B\begin{pmatrix}2\\ 2\end{pmatrix}\right]. \tag{2.18}$$

A photodetector measures the intensity of the light. Hence, PD+ and PD- on fig. 2.4 measure, respectively, intensities proportional to $|A|^2$ and $|B|^2$. When the cavity is at resonance E^r is linearly polarized, resulting in $|A|^2 - |B|^2 = 0$. For elliptically polarized light, i.e. when the light is not resonant with respect to the cavity, $|A|^2 - |B|^2 \neq 0$ with the sign of this difference depending on the handedness of the polarization ellipse that depends on the sign of detuning of the laser (in other terms, the phase shift of $E^r_{\parallel}$ with respect to $E^r_{\perp}$). In terms of $E^r_{\parallel}$ and $E^r_{\perp}$, E_+ and E_- are given by

$$E_\pm = \frac{1}{2}\begin{pmatrix}1 & \pm 1\\ \pm 1 & 1\end{pmatrix}\begin{pmatrix}1 & 0\\ 0 & i\end{pmatrix}\begin{pmatrix}E^r_{\parallel}\\ E^r_{\perp}\end{pmatrix}. \tag{2.19}$$

Finally, $I_+ - I_-$ in terms of $E^r_{\parallel}$ and $E^r_{\perp}$ is

$$I_+ - I_- = \frac{iv\varepsilon}{2}\left[E^{*r}_{\parallel}E^r_{\perp} - E^{*r}_{\perp}E^r_{\parallel}\right], \tag{2.20}$$

where v is the speed of light, ε is the permittivity. From eqs. (2.8) to (2.10), (2.13) and (2.20)

$$I_+ - I_- = 2I_0\cos\theta\sin\theta\frac{T_1 R\sin\Delta}{(1-R)^2 + 4R\sin^2\frac{\Delta}{2}}, \tag{2.21}$$

where $I_0 = \frac{1}{2}v\varepsilon|E^{(i)}|^2$ is the initial intensity of the laser beam. A plot of eq. (2.21) is shown in fig. 2.5, the parameters chosen to this plot ($T_1 = 1\times10^{-4}$, R = 0.97) were chosen to be realistic values, i.e. they are typical parameters of commercial optical elements. We can compare the signal shown in fig. 2.5 to the ones shown in fig. 2.2. Although very simple in terms of electronic components, the Hänsch-Couillaud (HC) technique generates error signals that have a good capture range

comparing to PDH technique performed at modulation frequencies below the cavity linewidth (see fig. 2.2). A comparison of the expected attributes of the error signals generated by PDH and HC technique will be shown further in this section.

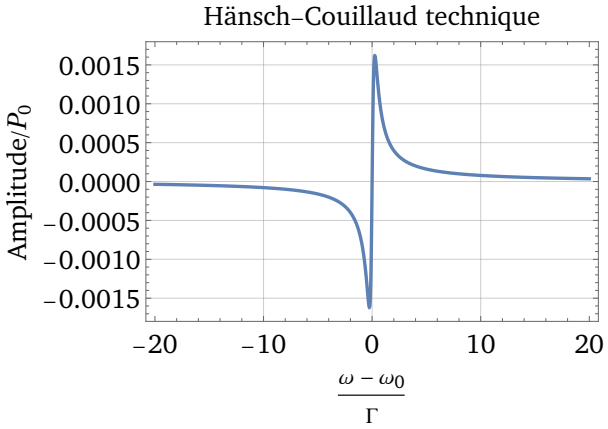

FIGURE 2.5: Theoretical error signal generated by Hänsch-Couillaud technique. The parameters used for this graph were $T_1 = 4.9 \times 10^{-4}$ and $R = 0.97$ and $\theta = \frac{\pi}{4}$. P_0 denotes the initial power of the laser beam.

2.2.3 SHG cavity locking by Hänsch-Couillaud technique

The HC technique can be also used, as shown for PDH technique, to stabilize a cavity to the frequency mode of a previously stabilized laser [40]. This is particularly useful for the stabilization of SHG cavities to the frequency of the fundamental (input) laser beam. This method is used in the present work for the stabilization of a SHG cavity that delivers up to 2.5 W of light at 399 nm, that is used for laser cooling of Yb in the ${}^1S_0 - {}^1P_1$ transition as will be detailed in the next chapter. In terms of optical components, the important difference of the scheme shown in fig. 2.4 to fig. 2.6 is that in the latter one the nonlinear crystal also plays the role of the intracavity polarizer, due to typical birefringent properties of the nonlinear crystal. In order to stabilize the cavity, one of the cavity mirrors is controlled by a piezoelectric controller that receives the feedback signal (the error signal) from a PID controller. The signal from the PID controller is summed with the signal from a function generator that is used to scan the frequency of the cavity.

2.2.4 Comparison of PDH and HC techniques

In order to decide which frequency stabilization technique to use, it is important to take into account their differences regarding implementation and performance. The differences regarding the practical implementation were previously mentioned and lie on the fact that HC technique makes use of simpler electronics. Indeed, PDH technique lies on frequency modulation of the optical beam which requires fast electronic components (RF drivers, mixers, RF amplifiers and filters) and acousto-optic (AOM) or electro-optic (EOM) devices.

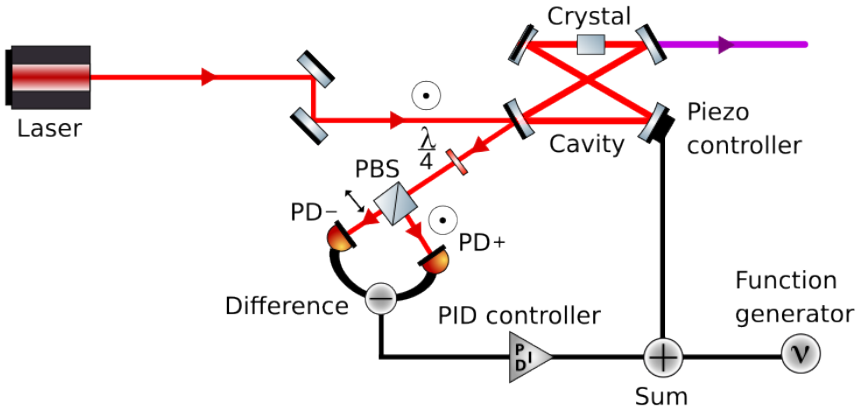

FIGURE 2.6: Simplified experimental scheme for a bow-tie cavity stabilization by the Hänsch-Couillaud technique.

For comparison, it will be considered the optimization of the PDH technique with respect to the modulation frequency (δ), assuming that $\beta = 1.1$. This value of β does not fulfill the requirement for narrowband modulation (section 2.1.2), however it nearly maximizes $J_0(\beta)J_1(\beta)$ in eq. (2.5) and it will be used here for illustration. It will be also assumed that the cavity is composed by two identical mirrors with $|r|^2 = 0.99$ and without losses, i.e. $|r|^2 + |t|^2 = 1$. The data shown here is obtained numerically with the software *Wolfram Mathematica*, that is used to obtain the slope (at $\omega = \omega_0$) and capture range of the terms oscillating at frequency δ in eq. (2.5). The capture range shown here is a relative quantity, defined here as the frequency at which the error signal drops to a value that is 10% of its maximum value. The cavity linewidth is given by the relation $\Gamma_{PDH} = \frac{\Delta_{fsr}}{F_{PDH}}$, where the subscript PDH is used to distinguish from the Hänsch-Couillaud situation that will be described in this section, and F_{PDH} is the cavity finesse defined by $F_{PDH} = \frac{\pi|r|}{1-|r|^2}$. Fig. 2.7a is a log-log plot of the error signal slope (in units of $\frac{P_0}{\Gamma_{PDH}}$), with respect to the modulation frequency (in units of Γ_{PDH}). P_0 is the initial beam power, therefore the results do not take into account any electronic losses (photodetector efficiency, losses due to signal propagation, RF mixer, etc.). In blue, the signal slope of the real part of the readout function shows that it reaches a maximum for modulation frequencies close to $0.6\Gamma_{PDH}$ when it starts to decrease. On the other hand, the slope at $\omega = \omega_0$ of the imaginary part of $R(\delta)$, in red, only increases until it reaches a plateau for modulation frequencies higher than Γ_{PDH}. Fig. 2.7b shows the capture range (in units of Γ_{PDH}) with respect to the modulation frequency. The quantities for $\mathrm{Re}\{[R(\omega)]\}$ are not depicted for modulation frequencies higher than 1.5Γ because the maximum and the minimum of the error signal are split and only a much smaller dispersive feature remains in the center of the curve, as illustrated in fig. 2.2c. It can be seen in fig. 2.7b that the capture range for $\mathrm{Re}\{[R(\omega)]\}$ is larger than for $\mathrm{Im}\{[R(\omega)]\}$ for the depicted modulation frequencies. In summary, for modulation frequencies below

Γ_{PDH} it is advantageous to use $\mathrm{Re}\{[R(\omega)]\}$ as error signal, while for higher modulation frequencies $\mathrm{Im}\{[R(\omega)]\}$ offers a better slope and a capture range that is defined by the modulation frequency itself, as can be observed in fig. 2.2c.

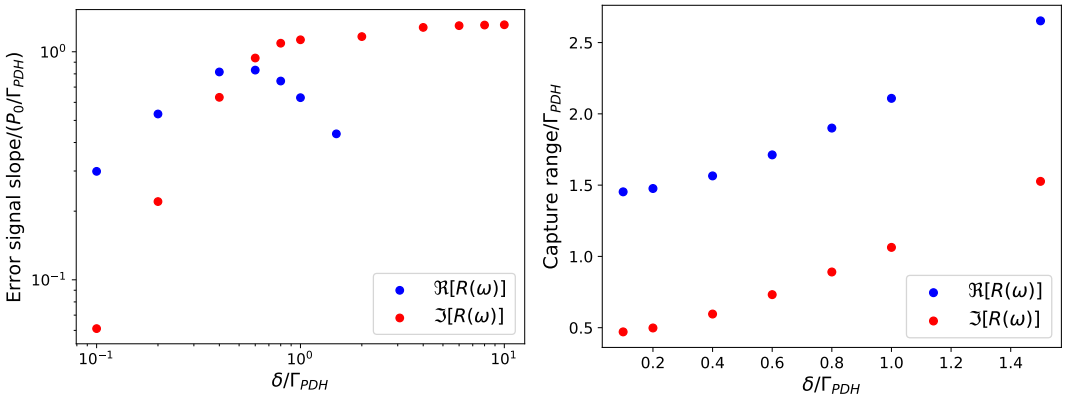

(A) (B)

FIGURE 2.7: (A) PDH Error signal slope in units of $\frac{P_0}{\Gamma}$ for $\mathrm{Re}\{[R(\omega)]\}$ (in blue) and $\mathrm{Im}\{[R(\omega)]\}$ (in red) as a function of the modulation frequency, the plot is shown in log-log scale. (B) Capture range, as defined in the text, as a function of the modulation frequency. For both figures it was assumed a modulation index (β) of 1.1 and a that the two cavity mirrors are identical with $|r^2| = 0.99$.

For the HC technique, the parameter chosen to be optimized is $|t_1|^2$, the other parameters are $R = 0.99(1 - |t_1|)$ and $\Delta = \frac{\pi}{4}$. As $|t_1|^2$ is changed, the cavity finesse is also changed. Therefore, the results will be given in terms of the previously defined cavity linewidth for the PDH case (Γ_{PDH}) to facilitate a comparison with the PDH case. The HC cavity finesse is given by $F_{HC} = \frac{\pi R}{1-R^2}$ and its linewidth (Γ_{HC}) is given in terms of the linewidth for the PDH case, by assuming cavities of same free spectral range, as follows $\Gamma_{HC} = \frac{\Gamma_{PDH} F_{PDH}}{F_{HC}}$. The data shown here is also numerically obtained with the software *Wolfram Mathematica*, that is used to obtain the slope and capture range of eq. (2.21). The HC error signal slope as a function of the first mirror transmittance is shown in fig. 2.8a for values of $|t_1|^2$ from 4.9×10^{-3} to 0.64, where 4.9×10^{-3} corresponds to the $|t_1|^2$ used for the PDH case. It can be seen that the slope increases by increasing the mirror transmittance, for low transmitances, reaching a maximum at around $|t_1|^2 = 0.04$. However, in fig. 2.8b it is shown that the capture range (in units of Γ_{PDH}) increases by increasing the first mirror transmittance. It is assumed that the linear polarizer does not introduce any losses.

We conclude that for applications that need high finesse cavities, it is advantageous to make use of PDH technique with modulation frequencies higher than the cavity linewidth. This way, a high error signal slope is obtained and the capture range is determined by the modulation frequency itself. The HC technique is not well suited for this kind of application because the finesse of the cavity would be limited by losses due to the polarizer (or birefringent element), leading to a decay of the error signal slope. For applications that do not need a high finesse cavity (as SHG), the HC technique can achieve an error signal slope of the order of the PDH

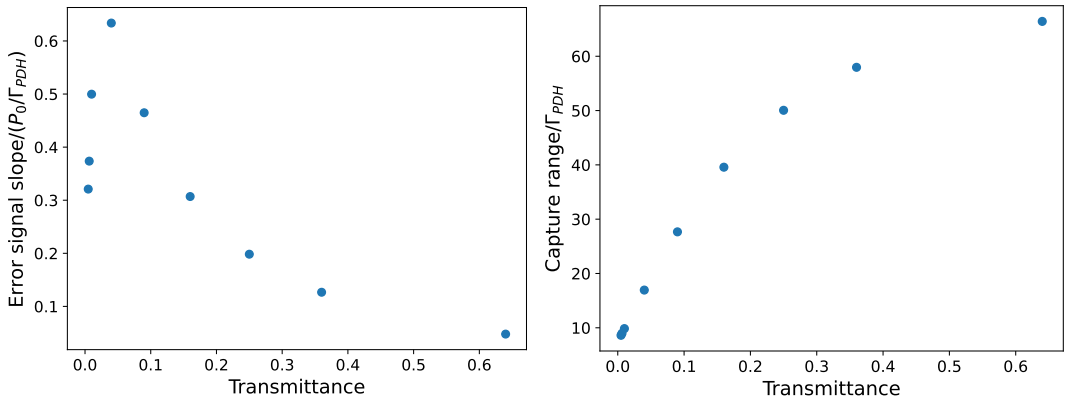

(A) (B)

FIGURE 2.8: A) HC Error signal slope in units of $\frac{P_0}{\Gamma_{PDH}}$ as a function of the first mirror transmittance. (B) Capture range, as defined in the text, as a function of the first mirror transmittance. For both figures it was assumed that the first mirror transmittance is changed while the three other mirrors are identical with $|r^2| = 0.99$.

one but with a high capture range without the need of high frequency modulation. The power consumption is also an advantage of the HC technique. Frequency modulation requires RF drivers and amplifiers delivering powers of the order of 10 W, while HC only requires two photodetectors.

2.3 Frequency modulated spectroscopy

The two methods introduced above are widely used and very important in modern optics laboratories. In atomic physics experiments, they are used to stabilize a laser frequency close to an atomic or molecular transition that will be probed. However, although optical cavities are not absolute frequency references, many applications, such as precision spectroscopy, require the use of absolute references (atomic or molecular transitions). In other cases they are more convenient because they can be more cost-effective and compact. In this section two similar spectroscopic techniques used for laser frequency stabilization are going to be introduced, they are frequency modulation (FM) spectroscopy and modulation transfer spectroscopy (MTS). FM spectroscopy is indeed not used in the experiment that is described in this thesis, but it is the precursor of MTS which is the laser frequency stabilization technique used for laser cooling of ^{174}Yb on the $^1S_0 - {}^3P_1$ transition in the present work, as will be shown in the next chapter.

2.3.1 Experimental scheme

The principle of FM spectroscopy is the same of the PDH technique. The interference of 3 fields of different frequencies (one carrier and two sidebands) when the carrier frequency is scanned around a frequency reference generates a dispersive signal, which can be retrieved and used in a feedback loop for the laser stabilization. A

simple experimental scheme is shown in fig. 2.9 for the case of a linear absorption experiment. The beam generated by the laser is modulated by an EOM (AOM) and its transmission (the fluorescence signal can also be used) is measured by a photodetector. The measured signal is sent to an RF mixer to be demodulated. After the mixer the signal passes through a PID controller that controls the current of the laser diode. In this scheme, the synthesizer generates a sinusoidal wave at a given frequency that is modulated at a frequency defined by another sinusoidal wave generated by the function generator. The output of the function generator (which can have its phase tuned) is sent to an input of the RF mixer in order to perform the demodulation of the signal.

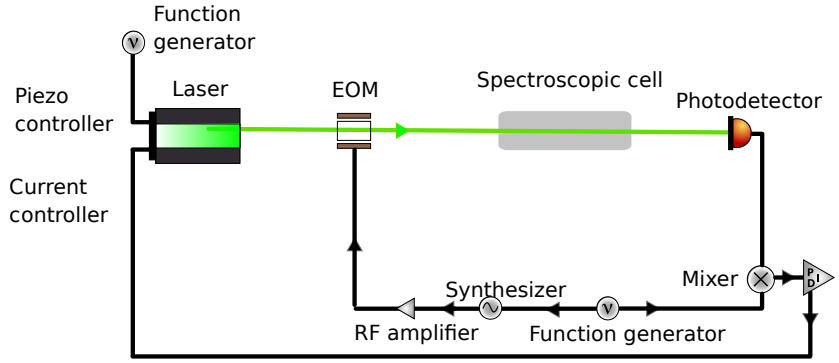

FIGURE 2.9: Experimental scheme for laser frequency stabilization by FM spectroscopy.

2.3.2 Error signal

The calculation for the generation of the error signal is completely analogous to the PDH case, it is described in [41, 42] and it will be simply summarized here. Therefore, assuming an incident plane wave that is frequency (phase) modulated in the narrowband regime, the power measured by the photodiode is also given by eq. (2.5). In the case of FM spectroscopy the readout function (R(ω)) is written in terms of the amplitude transmission coefficient $T(\omega)$. A sample (spectroscopic cell) of length L, intensity absorption coefficent $\alpha(\omega)$ and index of refraction $\eta(\omega)$ has an amplitude transmission coefficient at a given frequency ω given by

$$T(\omega) = e^{-\frac{\alpha(\omega)L}{2} - i\frac{\eta(\omega)L\omega}{c}}. \tag{2.22}$$

The error signal is generated by the demodulation of the real and/or imaginary parts of

$$R(\omega) = T(\omega)T^*(\omega+\delta) - T^*(\omega)T(\omega-\delta). \tag{2.23}$$

The resulted error signals are very similar to the ones shown in fig. 2.2 and were reported in [42].

The scheme shown in fig. 2.9 generates an error signal with a peak-to-valley width determined by the Doppler-broadened linewidth of the transition at which the spectroscopy is being performed. For many applications it is needed to use transitions between hyperfine atomic/molecular levels as reference. Hence, FM spectroscopic can be used in combination with saturated absorption spectroscopy to obtain narrower error signals centered at the center of the hyperfine spectral line. Experimentally, the sub-Doppler version of FM spectroscopy differ from fig. 2.9 by the addition of a beam counterpropagating (pump beam) to the probe beam, that is the one modulated and measured by the photodiode. Throughout the thesis, the "probe beam" of a saturated absorption spectroscopy will be distinguished from the "pump beam" by the fact that the probe is the one that is measured. $\alpha(\omega)$ and $\eta(\omega)$ in such cases are given by the differences between the Doppler-broadened contribution to the sub-Doppler one. This generates error signals with a background that is not flat due to the contribution of the Doppler signal. Fig. 2.10 shows the sub-Doppler spectrum for the case where the hyperfine (Lorentzian) spectrum of linewidth Γ is centered at a frequency shift of 10Γ from the center of the Doppler (Gaussian) spectrum that has a linewidth of 20Γ and an amplitude 10 times bigger. The linewidths of the hyperfine and Doppler-broadened signal, as well as the frequency shift of the hyperfine line with respect to the center of the Doppler-broadened one were arbitrarily chosen by the author for illustration purposes.

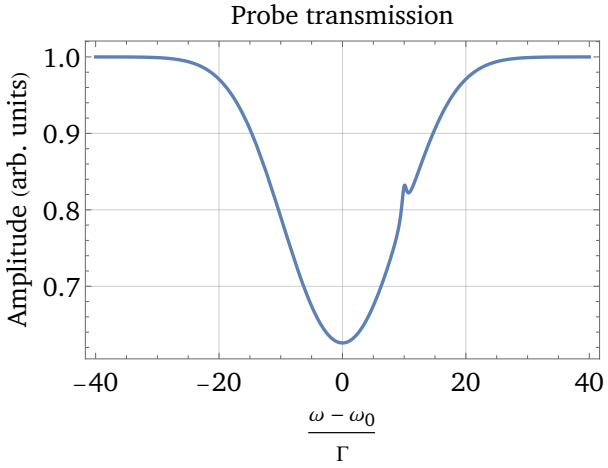

FIGURE 2.10: Typical theoretical transmission of a saturated absorption spectroscopy.

Assuming $|L\left[\eta(\omega)\omega \pm \eta(\omega \pm \delta)(\omega \pm \delta)\right]| << c$, it can be shown that

$$\mathrm{Re}[R(\omega)] = e^{\frac{L}{2}[\alpha(\omega)+\alpha(\omega+\delta)]} - e^{\frac{L}{2}[\alpha(\omega-\delta)-\alpha(\omega)]}. \tag{2.24}$$

$\mathrm{Re}[R(\omega)]$ is shown in fig. 2.11, for the same parameters as fig. 2.10 and a modulation frequency $\delta = 0.1\Gamma$. A background due to the Doppler contribution can be seen. The absence of such background in MTS is one of the main motivations for its use instead of FM spectroscopy.

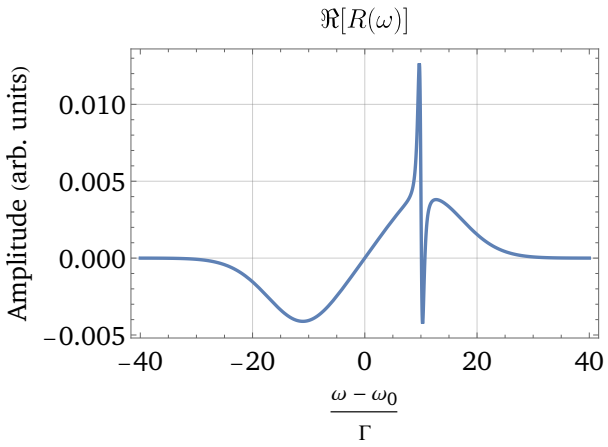

FIGURE 2.11: Typical error signal generated by sub-Doppler FM spectroscopy for a modulation frequency of $\delta = 0.1\Gamma$.

2.4 Modulation transfer spectroscopy

It can be seen in fig. 2.11 that the error signal generated by FM spectroscopy of a hyperfine transition has a Doppler background contribution. It was shown [43] that by applying the modulation to the pump beam in a saturated absorption spectroscopy scheme, the Doppler contribution is eliminated and a flat spectrum is observed. Such a technique, called modulation transfer spectroscopy (MTS), lies on the generation of sidebands in the probe direction by four-wave mixing proccesses.

2.4.1 Experimental scheme

MTS differs from FMS because in MTS the sidebands that interfere with the probe beam are not generated by the probe beam frequency modulation. Instead, the pump beam is frequency modulated and the interaction of the probe, the carrier component of the pump and its sidebands with the atomic/molecular medium gives rise to a third-order nonlinear effect (four-wave mixing) that generates electric fields in the direction of propagation of the probe beam. The probe field interferes with the generated sidebands in the vapour cell and the measurement of the beams by a photodiode after the propagation through the atomic medium generates a signal with dispersive-like shape that can be used as error signals for laser frequency stabilization.

A typical MTS experiment is shown in fig. 2.12. The laser beam is divided in two by the combination of a half-wave plate and PBS 1, the reflection of PBS 1 is reflected by two mirrors before enter the vapour cell where it plays the role of a probe beam in a saturated absorption spectroscopy scheme. The transmission of PBS 1 is frequency shifted and modulated by an AOM, and the carrier and its sidebands are also transmitted by PBS 3 to pass through the vapour cell counterpropagating to the probe beam. The nonlinear interaction of the carrier and sidebands of the pump field with the atomic medium and the probe field generates electric fields that propagate in the direction of the probe beam and that are frequency shift from it by the value of

the frequency modulation of the carrier field that drives the AOM. The interference of the generated fields with the probe one is measured by a photodetector (PD). The role of PBS 2 is to allow an independent control of the probe beam power.

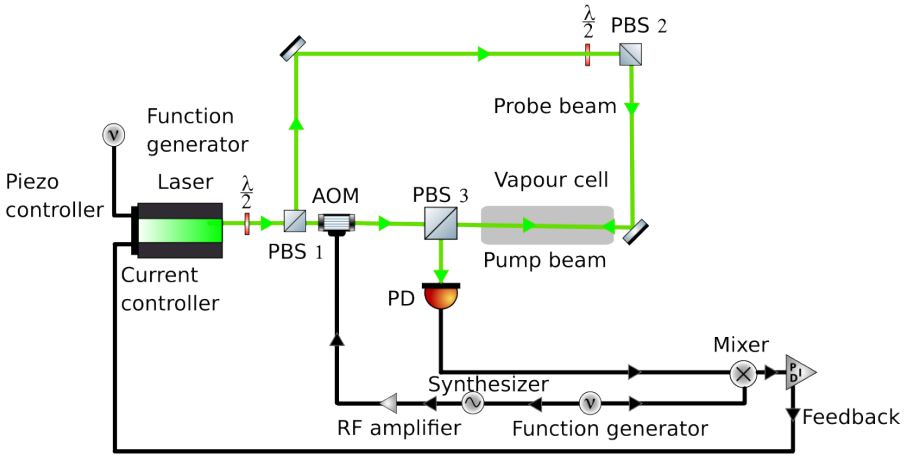

FIGURE 2.12: Simplified experimental scheme for laser frequency stabilization by the modulation transfer spectroscopy.

2.4.2 Derivation of the error signal

In fig. 2.12 it can be seen that the error signal is generated by the demodulation of the beating between the probe beam and the sidebands that are generated at its direction. The lineshape of the signal will be derived by assuming that all of the beams involved are collinear, the modulation of the pump field is narrowband (i.e. we can consider only the first sidebands) and the atoms are described by an ensemble of two-level systems. Density matrix formalism will be used to calculate by a perturbative approach the coherence between the ground and excited states, which allows the calculation of the frequency shifted fields that propagate in the direction of the probe beam. The incident pump (E_c) and probe (E_p) fields are assumed linearly polarized and described by:

$$E_c(t) = \frac{1}{2}E_{c,0}[J_0(\beta)e^{i[(\omega+\Delta)t+kz]} + J_1(\beta)e^{i[(\omega+\Delta+\delta)t+kz]} - J_1(\beta)e^{[i(\omega+\Delta-\delta)t+kz]}] + c.c, \tag{2.25}$$

$$E_p(t) = \frac{1}{2}E_{p,0}e^{i[\omega t-kz+\phi_p]} + c.c. \tag{2.26}$$

Where Δ denotes the carrier frequency of the EOM/AOM, c.c the complex conjugate, $E_{c,0}$ the amplitude of the non-modulated pump field, $E_{p,0}$ the amplitude of the probe field, δ the modulation frequency and β the modulation index. It is also assumed that the wavenumbers of the fields are approximately the same (k), and that the positive sideband is in phase with the carrier, while the negative one is out of phase by a factor π.

The time evolution of the density matrix components is described by the Liouville-von Neumman equation, as follows

$$i\hbar\frac{\mathrm{d}\hat{\rho}}{\mathrm{d}t} = \left[\hat{H}, \hat{\rho}\right]. \tag{2.27}$$

$\hbar$ is given by $\frac{h}{2\pi}$ where h is the Planck constant. The matrix representation of the density operator is

$$\hat{\rho} = \begin{pmatrix} \rho_{gg} & \rho_{ge} \\ \rho_{eg} & \rho_{ee} \end{pmatrix}. \tag{2.28}$$

The diagonal terms of eq. (2.28) represent the populations of the levels and the off-diagonal terms represent the coherences between them. $\hat{H}$ is the hamiltonian of the system that is composed by two terms, as follows

$$\hat{H} = \hat{H}_0 + \hat{V}. \tag{2.29}$$

$\hat{H}_0$ is the hamiltonian for the two-level system, and $\hat{V}$ describes the interaction of the atoms with the light. They can be written as

$$\hat{H}_0 = \hbar\omega_e \left|e\right\rangle \left\langle e\right| + \hbar\omega_g \left|g\right\rangle \left\langle g\right| \tag{2.30}$$

$$\hat{V} = -\hat{\mu}\cdot\vec{E}. \tag{2.31}$$

Where $\hat{\mu}$ is the electric dipole operator, "e" and "g" represents the atomic excited and ground states and $\vec{E}$ represents the sum of the input fields. It is convenient to define the Rabi frequencies of the different field components, where the component is represented by the subscript "i", as

$$\Omega_i = \frac{\mu_{ge}E_{i,0}}{\hbar}. \tag{2.32}$$

The subscripts $+$ and $-$ will denote, respectively, the first sidebands of higher and low frequency of the pump field, while the subscript "c" denotes the carrier of the pump field and "p" the probe field. The eq. (2.27) is developed, terms that represent the loss of population from the states ($\Gamma_{ii}(\rho_{ii}^{eq} - \rho_{ii})$) and the relaxation rate for the coherence ($\Gamma_{ge}\rho_{ge}$) are phenomenologically introduced. ρ_{ii}^{eq} represents the population of level "i" at equilibrium, and finally applying the rotating-wave approximation (RWA), the rate equations for the density matrix components become

$$\begin{aligned}\dot{\rho}_{gg} = -\frac{1}{2}\{i\rho_{ge}^{*}[\Omega_c e^{i[(\omega+\Delta)t+kz]} + \Omega_+ e^{i[(\omega+\Delta+\delta)t+kz]} - \Omega_- e^{i[(\omega+\Delta-\delta)t+kz]} + \\ + \Omega_p e^{i\left[\omega t-kz+\phi_p\right]}] + c.c\} + \Gamma_{gg}(\rho_{gg}^{eq} - \rho_{gg}),\end{aligned} \tag{2.33}$$

$$\begin{aligned}\dot{\rho}_{ee} = \frac{1}{2}\{i\rho_{ge}^{*}[\Omega_c e^{i[(\omega+\Delta)t+kz]} + \Omega_+ e^{i[(\omega+\Delta+\delta)t+kz]} - \Omega_- e^{i[(\omega+\Delta-\delta)t+kz]} + \\ - \Omega_p e^{i\left[\omega t-kz+\phi_p\right]}] + c.c\} + \Gamma_{ee}(\rho_{ee}^{eq} - \rho_{ee}),\end{aligned} \tag{2.34}$$

$$\begin{aligned}\dot{\rho}_{ge} = -\frac{i}{2}[&\Omega_c e^{i[(\omega+\Delta)t+kz]} + \Omega_+ e^{i[(\omega+\Delta+\delta)t+kz]} - \Omega_- e^{i[(\omega+\Delta-\delta)t+kz]} + \\ &- \Omega_p e^{i\left[\omega t - kz + \phi_p\right]}](\rho_{ee} - \rho_{gg}) - i\rho_{ge}\omega_{ge} - \Gamma_{ge}\rho_{ge}.\end{aligned} \tag{2.35}$$

The equation for ρ_{eg} is given by $\rho_{eg} = \rho^*_{ge}$, and $\omega_{ge} = \omega_g - \omega_e$.

If we assume that $\hat{\rho}$ is also position-dependent, the total derivative is written as

$$\frac{\mathrm{d}\rho(\hat{z},t)}{\mathrm{d}t} = \frac{\partial\rho(\hat{z},t)}{\partial t} + v\frac{\partial\rho(\hat{z},t)}{\partial z} \tag{2.36}$$

in which v represents the velocity component along the z axis.

The interaction between the fields and the atomic system gives rise to a nonlinear macroscopic polarization, which re-radiates fields that act as sidebands for the probe beam and that propagate in its direction. Indeed, this nonlinear process also generates fields of different frequencies [44] but we are only interested in the ones mentioned above and depicted in fig. 2.13.

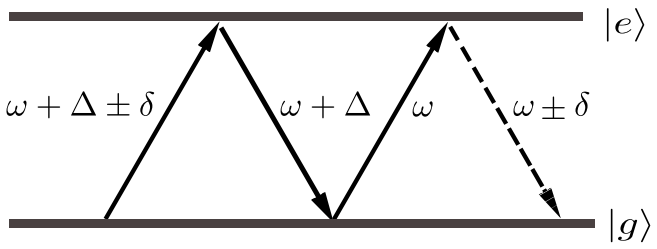

(A)

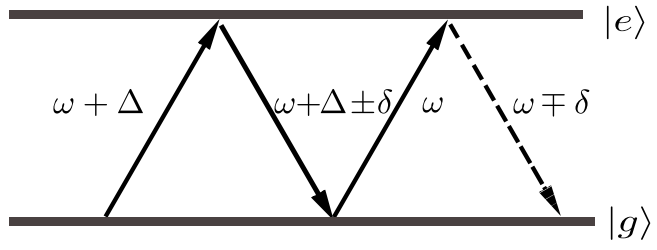

(B)

FIGURE 2.13: Four-wave mixing processes that generate fields of frequencies $\omega \pm \delta$ in the direction of propagation of the probe beam.

To solve eqs. (2.33) to (2.35) it is convenient to define the following variables

$$\mathcal{E} = z + vt, \tag{2.37}$$

$$\eta = z - vt. \tag{2.38}$$

Then, $\frac{\partial}{\partial t} + v\frac{\partial}{\partial z}$ can be written as

$$\frac{\partial}{\partial t} + v\frac{\partial}{\partial z} = 2v\frac{\partial}{\partial \mathcal{E}}. \tag{2.39}$$

Defining $\omega_c = \omega + \Delta$, $\omega_+ = \omega + \Delta + \delta$ and $\omega_- = \omega + \Delta - \delta$, eqs. (2.33) to (2.35) can now be written as a function of $\mathcal{E}$ and η

$$\begin{aligned} 2v\frac{\partial \rho_{gg}}{\partial \mathcal{E}} &= -\frac{1}{2}\{i\rho^*_{ge}[\Omega_c e^{i\left[(\omega_c+kv)\frac{\mathcal{E}}{2v}+(kv-\omega_c)\frac{\eta}{2v}\right]} + \Omega_+ e^{i\left[(\omega_++kv)\frac{\mathcal{E}}{2v}+(kv-\omega_+)\frac{\eta}{2v}\right]}+ \\ &\quad - \Omega_- e^{i\left[(\omega_-+kv)\frac{\mathcal{E}}{2v}+(kv-\omega_-)\frac{\eta}{2v}\right]} + \Omega_p e^{i\left[(\omega-kv)\frac{\mathcal{E}}{2v}-(kv+\omega)\frac{\eta}{2v}+\phi_p\right]}] + c.c\}+ \\ &\quad + \Gamma_{gg}(\rho^{eq}_{gg} - \rho_{gg}), \end{aligned} \tag{2.40}$$

$$\begin{aligned} 2v\frac{\partial \rho_{ee}}{\partial \mathcal{E}} &= \frac{1}{2}\{i\rho^*_{ge}[\Omega_c e^{i\left[(\omega_c+kv)\frac{\mathcal{E}}{2v}+(kv-\omega_c)\frac{\eta}{2v}\right]} + \Omega_+ e^{i\left[(\omega_++kv)\frac{\mathcal{E}}{2v}+(kv-\omega_+)\frac{\eta}{2v}\right]}+ \\ &\quad - \Omega_- e^{i\left[(\omega_-+kv)\frac{\mathcal{E}}{2v}+(kv-\omega_-)\frac{\eta}{2v}\right]} + \Omega_p e^{i\left[(\omega-kv)\frac{\mathcal{E}}{2v}-(kv+\omega)\frac{\eta}{2v}+\phi_p\right]}] + c.c\}+ \\ &\quad + \Gamma_{ee}(\rho^{eq}_{ee} - \rho_{ee}), \end{aligned} \tag{2.41}$$

$$\begin{aligned} 2v\frac{\partial \rho_{ge}}{\partial \mathcal{E}} &= -\frac{i}{2}[\Omega_c e^{i\left[(\omega_c+kv)\frac{\mathcal{E}}{2v}+(kv-\omega_c)\frac{\eta}{2v}\right]} + \Omega_+ e^{i\left[(\omega_++kv)\frac{\mathcal{E}}{2v}+(kv-\omega_+)\frac{\eta}{2v}\right]}+ \\ &\quad - \Omega_- e^{i\left[(\omega_-+kv)\frac{\mathcal{E}}{2v}+(kv-\omega_-)\frac{\eta}{2v}\right]} + \Omega_p e^{i\left[(\omega-kv)\frac{\mathcal{E}}{2v}-(kv+\omega)\frac{\eta}{2v}+\phi_p\right]}](\rho_{ee} - \rho_{gg})+ \\ &\quad - i\rho_{ge}\omega_{ge} - \Gamma_{ge}\rho_{ge}. \end{aligned} \tag{2.42}$$

From Eqs. (2.40) to (2.42), it is observed that the density matrix component ρ_{lm}, where l and m can be either g or e, can be written in a compact form as

$$2v\frac{\partial \rho_{lm}}{\partial \mathcal{E}} = -i\omega_{lm}\rho_{lm} - \frac{i}{\hbar}\left[\hat{V}, \hat{\rho}\right]_{lm} - \Gamma_{lm}(\rho_{lm} - \rho^{eq}_{lm}). \tag{2.43}$$

Where $\omega_{lm} = \omega_l - \omega_m$ and $\Gamma_{lm} = \Gamma_{ml}$.

Four-wave mixing is a third-order nonlinear process. Therefore, the fields generated by the processes depicted in fig. 2.13 are proportional to the third-order optical coherence. Moreover, assuming an optically thin gas sample, the re-radiated fields due to third-order nonlinear processes have their amplitudes defined by [44, 45]

$$E_r = -i\frac{kL}{2\epsilon_0}\mu_{eg}\langle\rho^{(3)}_{ge}\rangle + c.c. \tag{2.44}$$

$\langle\rho^{(3)}_{ge}\rangle$ denotes the velocity-averaged third-order optical coherence, ϵ_0 the vacuum permittivity and L the length of the medium. The calculation of $\rho^{(3)}_{ge}$ can be performed in the framework of perturbation theory. Indeed, it can be shown that by assuming a perturbation expansion in the incident fields, the element of order $n+1$ (i.e. $\rho^{(n+1)}_{lm}$) can be calculated in terms of the element of order n (i.e. $\rho^{(n)}_{lm}$) as below [46]

$$\rho^{(n+1)}_{lm} = -\frac{1}{2v}\int_{-\infty}^{\mathcal{E}} \frac{i}{\hbar}\left[\hat{V}, \hat{\rho}^{(n)}\right]_{lm} e^{\frac{1}{2v}(i\omega_{lm}+\Gamma_{lm})(\mathcal{E}'-\mathcal{E})} d\mathcal{E}' \tag{2.45}$$

Where $\hat{V}$ can be written in the matricial form as

$$\hat{V} = \begin{pmatrix} 0 & V_{ge} \\ V_{eg} & 0 \end{pmatrix}, \tag{2.46}$$

and its elements are given by eq. (2.31)

$$\begin{aligned} V_{ge} = \frac{\hbar}{2}[&\Omega_c e^{i\left[(\omega_c + kv)\frac{\mathcal{E}}{2v} + (kv - \omega_c)\frac{\eta}{2v}\right]} + \Omega_+ e^{i\left[(\omega_+ + kv)\frac{\mathcal{E}}{2v} + (kv - \omega_+)\frac{\eta}{2v}\right]} + \\ &- \Omega_- e^{i\left[(\omega_- + kv)\frac{\mathcal{E}}{2v} + (kv - \omega_-)\frac{\eta}{2v}\right]} + \Omega_p e^{i\left[(\omega - kv)\frac{\mathcal{E}}{2v} - (kv + \omega)\frac{\eta}{2v} + \phi_p\right]}], \end{aligned} \tag{2.47}$$

$$V_{eg} = V_{ge}^*. \tag{2.48}$$

Therefore,

$$\left[\hat{V}, \hat{\rho}^{(n)}\right] = \begin{pmatrix} V_{ge}\rho_{eg}^{(n)} - V_{eg}\rho_{ge}^{(n)} & V_{ge}(\rho_{ee}^{(n)} - \rho_{gg}^{(n)}) \\ V_{eg}(\rho_{gg}^{(n)} - \rho_{ee}^{(n)}) & V_{eg}\rho_{ge}^{(n)} - V_{ge}\rho_{eg}^{(n)}. \end{pmatrix} \tag{2.49}$$

$\rho_{lm}^{(0)}$ are defined as the solutions of eq. (2.43) without interaction, which is assumed to be ρ_{lm}^{eq}. Thermal excitation is assumed to be a fully incoherent process, making $\rho_{ll}^{eq} = 0$. In summary

$$\rho_{ll}^{(0)} = \rho_{ll}^{eq}, \tag{2.50}$$

$$\rho_{lm}^{eq} = 0, \text{ for } l \neq m. \tag{2.51}$$

We note from eqs. (2.45), (2.50) and (2.51) that $\rho_{ll}^{(1)} = 0$, the other terms can be calculated by

$$\rho_{ge}^{(1)} = -\frac{i}{2v\hbar}\int_{-\infty}^{\mathcal{E}} V_{ge}(\rho_{ee}^{eq} - \rho_{gg}^{eq}) e^{\frac{1}{2v}(i\omega_{ge} + \Gamma_{ge})(\mathcal{E}' - \mathcal{E})} d\mathcal{E}'. \tag{2.52}$$

The expressions for the populations in the second order of perturbation are

$$\rho_{gg}^{(2)} = -\frac{i}{2v\hbar}\int_{-\infty}^{\mathcal{E}} (V_{ge}\rho_{eg}^{(1)} - \rho_{ge}^{(1)}V_{eg}) e^{\frac{1}{2v}\Gamma_{gg}(\mathcal{E}' - \mathcal{E})} d\mathcal{E}', \tag{2.53}$$

$$\rho_{ee}^{(2)} = -\frac{i}{2v\hbar}\int_{-\infty}^{\mathcal{E}} (V_{eg}\rho_{ge}^{(1)} - \rho_{eg}^{(1)}V_{ge}) e^{\frac{1}{2v}\Gamma_{ee}(\mathcal{E}' - \mathcal{E})} d\mathcal{E}'. \tag{2.54}$$

Since $\rho_{gg}^{(1)} = \rho_{ee}^{(1)} = 0$, then $\rho_{eg}^{(2)} = 0$. Consequently, from eqs. (2.45) and (2.49) we also conclude that $\rho_{ee}^{(3)} = \rho_{gg}^{(3)} = 0$ and that the third-order optical coherence can be retrieved in terms of the second-order populations by

$$\rho_{ge}^{(3)} = -\frac{i}{2v\hbar}\int_{-\infty}^{\mathcal{E}} V_{ge}(\rho_{ee}^{(2)} - \rho_{gg}^{(2)}) e^{\frac{1}{2v}(i\omega_{ge} + \Gamma_{ge})(\mathcal{E}' - \mathcal{E})} d\mathcal{E}'. \tag{2.55}$$

In summary, eqs. (2.52) to (2.55) can be used in sequence to calculate $\rho_{ge}^{(3)}$. The results for each step will be given below without further algebraic details, remembering that $\rho_{ge}^{(n)} = \rho_{eg}^{(n)*}$, where the superscript * denotes complex conjugation. We also introduce the subscript q in k so that $k_p = -k$ and $k_q = k$ when $q = c, +, -$; which

leads to

$$\rho_{ge}^{(1)} = \frac{i}{2}(\rho_{gg}^{eq} - \rho_{ee}^{eq}) \sum_{q} \frac{\Omega_q e^{i(\omega_q + k_q v)\frac{\mathcal{E}}{2v} + i(k_q v - \omega_q)\frac{\eta}{2v} + \phi_q}}{i(\omega_{ge} + \omega_q + k_q v) + \Gamma_{ge}}, \tag{2.56}$$

$$\begin{aligned}\rho_{gg}^{(2)} = &-\frac{1}{4}(\rho_{gg}^{eq} - \rho_{ee}^{eq}) \sum_{q'}\sum_{q} \frac{\Omega_q \Omega_{q'} e^{i(\omega_q - \omega_{q'} + k_q v - k_{q'} v)\frac{\mathcal{E}}{2v} + i(k_q v - k_{q'} v - \omega_q + \omega_{q'})\frac{\eta}{2v} + \phi_q - \phi_{q'}}}{i(\omega_q - \omega_{q'} + k_q v - k_{q'} v) + \Gamma_{gg}} \\ &\times \left\{ \frac{1}{i(-\omega_{q'} - k_{q'} v + \omega_{eg}) + \Gamma_{eg}} + \frac{1}{i(\omega_q + k_q v + \omega_{ge}) + \Gamma_{eg}} \right\},\end{aligned} \tag{2.57}$$

$$\begin{aligned}\rho_{ee}^{(2)} = &\frac{1}{4}(\rho_{gg}^{eq} - \rho_{ee}^{eq}) \sum_{q'}\sum_{q} \frac{\Omega_q \Omega_{q'} e^{i(\omega_q - \omega_{q'} + k_q v - k_{q'} v)\frac{\mathcal{E}}{2v} + i(k_q v - k_{q'} v - \omega_q + \omega_{q'})\frac{\eta}{2v} + \phi_q - \phi_{q'}}}{i(\omega_q - \omega_{q'} + k_q v - k_{q'} v) + \Gamma_{ee}} \\ &\times \left\{ \frac{1}{i(-\omega_{q'} - k_{q'} v + \omega_{eg}) + \Gamma_{eg}} + \frac{1}{i(\omega_q + k_q v + \omega_{ge}) + \Gamma_{eg}} \right\},\end{aligned} \tag{2.58}$$

$$\begin{aligned}\rho_{ge}^{(3)} = &\frac{i}{8}(\rho_{ee}^{eq} - \rho_{gg}^{eq}) \\ &\times \sum_{q''}\sum_{q'}\sum_{q} \frac{\Omega_q \Omega_{q'} \Omega_{q''} e^{i(\omega_q - \omega_{q'} - \omega_{q''} + k_q v - k_{q'} v - k_{q''} v)\frac{\mathcal{E}}{2v} + i(k_q v - k_{q'} v - k_{q''} v - \omega_q + \omega_{q'} + \omega_{q''})\frac{\eta}{2v} + \phi_q - \phi_{q'} - \phi_{q''}}}{i(\omega_{ge} - \omega_{q''} - \omega_{q'} + \omega_q - k_{q''} v - k_{q'} v + k_q v) + \Gamma_{ge}} \\ &\times \left\{ \frac{1}{i(\omega_q - \omega_{q'} + k_q v - k_{q'} v) + \Gamma_{ee}} + \frac{1}{i(\omega_q - \omega_{q'} + k_q v - k_{q'} v) + \Gamma_{gg}} \right\} \\ &\times \left\{ \frac{1}{i(-\omega_{q'} - k_{q'} v + \omega_{eg}) + \Gamma_{eg}} + \frac{1}{i(\omega_q + k_q v + \omega_{ge}) + \Gamma_{eg}} \right\}.\end{aligned} \tag{2.59}$$

The summations over q, q' and q'' are performed over all of the incident fields (i.e. c, p, $+$ and $-$). Eq. (2.59) represents the third-order optical coherence between ground and excited states as a function of the variables $\mathcal{E}$ and η. To calculate $\rho_{ge}^{(3)}$ as a function of t and z one just needs to apply eq. (2.38) in eq. (2.59), which results in

$$\begin{aligned}\rho_{ge}^{(3)} = &\frac{i}{8}(\rho_{ee}^{eq} - \rho_{gg}^{eq}) \\ &\times \sum_{q''}\sum_{q'}\sum_{q} \frac{\Omega_q \Omega_{q'} \Omega_{q''} e^{\left[i(\omega_q - \omega_{q'} + \omega_{q''})t + i(k_q - k_{q'} + k_{q''})z + \phi_q - \phi_{q'} + \phi_{q''}\right]}}{\left[i(\omega_{ge} + \omega_{q''} - \omega_{q'} + \omega_q + k_{q''} v - k_{q'} v + k_q v) + \Gamma_{ge}\right]} \\ &\times \left\{ \frac{1}{\left[i(\omega_q - \omega_{q'} + k_q v - k_{q'} v) + \Gamma_{ee}\right]} + \frac{1}{\left[i(\omega_q - \omega_{q'} + k_q v - k_{q'} v) + \Gamma_{gg}\right]} \right\} \\ &\times \left\{ \frac{1}{\left[i(-\omega_{q'} - k_{q'} v + \omega_{eg}) + \Gamma_{eg}\right]} + \frac{1}{\left[i(\omega_q + k_q v + \omega_{ge}) + \Gamma_{eg}\right]} \right\}.\end{aligned} \tag{2.60}$$

Eq. (2.60) is a general expression for $\rho_{ge}^{(3)}$, however we are only interested in the

coherence generated by the processes illustrated in fig. 2.13. The amplitude of the term of $\rho_{ge}^{(3)}$ that oscillates at a frequency $\omega+\delta$ in the direction of propagation of the probe field will be denoted by $\rho_{ge}^{(3)}(\omega+\delta)$ and it is given by

$$\begin{aligned}\rho_{ge}^{(3)}(\omega+\delta) = \frac{i}{8}(\rho_{ee}^{eq}-\rho_{gg}^{eq})\frac{\Omega_p\Omega_c\Omega_\pm}{i(\omega_{ge}+\omega+\delta-kv)+\Gamma_{ge}}\sum_{l=g,e}\Bigg\{\frac{1}{i(\Delta+2kv)+\Gamma_{ll}}\\ \times\left[\frac{1}{i(-\omega-\Delta-kv+\omega_{eg})+\Gamma_{eg}}+\frac{1}{i(\omega-kv+\omega_{ge})+\Gamma_{eg}}\right]+\frac{1}{i\delta+\Gamma_{ll}}\\ \times\Bigg[\frac{1}{i(\omega+\Delta+\delta+kv+\omega_{ge})+\Gamma_{eg}}+\frac{1}{i(-\omega-\Delta-kv+\omega_{eg})+\Gamma_{eg}}+\\ +\frac{1}{i(\omega+\Delta+kv+\omega_{ge})+\Gamma_{eg}}+\frac{1}{i(-\omega-\Delta+\delta-kv+\omega_{eg})+\Gamma_{eg}}\Bigg]+\\ +\frac{1}{-i((\Delta-\delta)+2kv)+\Gamma_{ll}}\Bigg[\frac{1}{i(-\omega-\Delta+\delta-kv+\omega_{eg})+\Gamma_{eg}}+\\ +\frac{1}{i(\omega-kv+\omega_{ge})+\Gamma_{eg}}\Bigg]\Bigg\},\end{aligned} \tag{2.61}$$

where it is assumed that $\Omega_+ = \Omega_-$ and their values is denoted by $\Omega_\pm$. Now it is needed to perform a velocity-integration by assuming a Maxwell-Boltzmann distribution of the velocities (with rms value u), the total coherence is then given by

$$\langle\rho_{ge}^{(3)}(\omega+\delta)\rangle = \int_{-\infty}^{+\infty}\frac{e^{\frac{-v^2}{u^2}}\rho_{ge}^{(3)}(v)dv}{u\sqrt{\pi}}. \tag{2.62}$$

This integral will be performed in the Doppler limit (i.e. $ku \gg \Gamma_{eg},\Gamma_{gg},\Gamma_{ee}$). An expression similar to eq. (2.62) is solved in [44] by using the properties of the plasma dispersion function [47] and it can be shown that only the third and fifth terms on eq. (2.61) (the only terms that contain $+ikv$ on the denominator) are proportional to $\Gamma^{-2}(ku)^{-1}$, while the other terms are proportional to $\Gamma^{-1}(ku)^{-2}$ and $(ku)^{-3}$. Such integrals can also be performed by the software *Mathematica*, which was done for the present work. Therefore, by neglecting the integrals that are proportional to $(ku)^{-2}$ and $(ku)^{-3}$ eq. (2.61) results in

$$\begin{aligned}\langle\rho_{ge}^{(3)}(\omega+\delta)\rangle \approx \frac{i}{8}\frac{(\rho_{ee}^{eq}-\rho_{gg}^{eq})}{u\sqrt{\pi}}\int_{-\infty}^{+\infty}\frac{\Omega_\pm\Omega_p\Omega_c e^{\frac{-v^2}{u^2}}dv}{i(\omega_{ge}+\omega+\delta-kv)+\Gamma_{ge}}\sum_{l=g,e}\Bigg\{\frac{1}{i\delta+\Gamma_{ll}}\\ \times\left[\frac{1}{i(\omega+\Delta+\delta+kv+\omega_{ge})+\Gamma_{eg}}+\frac{1}{i(\omega+\Delta+kv+\omega_{ge})+\Gamma_{eg}}\right]\Bigg\}.\end{aligned} \tag{2.63}$$

We can further simplify the denominators of the integration in eq. (2.63)

$$\begin{aligned}\langle \rho_{ge}^{(3)}(\omega+\delta)\rangle \approx \frac{i(\rho_{ee}^{eq}-\rho_{gg}^{eq})\Omega_{\pm}\Omega_p\Omega_c}{16u\sqrt{\pi}} \int_{-\infty}^{+\infty} e^{\frac{-v^2}{u^2}} dv \sum_{l=g,e} \frac{1}{i\delta+\Gamma_{ll}} \\ \times \left\{ \frac{1}{\Gamma_{eg}+i(\omega_{ge}+\omega+\frac{\Delta}{2}+\delta)} \left[\frac{1}{i(\omega+\Delta+\delta+kv+\omega_{ge})+\Gamma_{eg}} + \right.\right. \\ \left.\left. + \frac{1}{i(\omega_{ge}+\omega+\delta-kv)+\Gamma_{ge}} \right] - \frac{1}{\Gamma_{eg}+i(\omega_{ge}+\omega+\frac{\Delta}{2}+\frac{\delta}{2})} \right. \\ \left. \times \left[\frac{1}{i(\omega+\Delta+kv+\omega_{ge})+\Gamma_{eg}} + \frac{1}{i(\omega_{ge}+\omega+\delta-kv)+\Gamma_{ge}} \right] \right\}.\end{aligned} \tag{2.64}$$

The result of the integration is

$$\begin{aligned}\langle \rho_{ge}^{(3)}(\omega+\delta)\rangle \approx \frac{i(\rho_{ee}^{eq}-\rho_{gg}^{eq})\Omega_{\pm}\Omega_p\Omega_c\sqrt{\pi}}{8ku} \sum_{l=g,e} \frac{1}{i\delta+\Gamma_{ll}} \\ \times \left\{ \frac{1}{\Gamma_{eg}+i(\omega_{ge}+\omega+\frac{\Delta}{2}+\delta)} - \frac{1}{\Gamma_{eg}+i(\omega_{ge}+\omega+\frac{\Delta}{2}+\frac{\delta}{2})} \right\}.\end{aligned} \tag{2.65}$$

The calculation of the amplitude of the coherence that oscillates at frequency $\omega-\delta$ is done by the same procedure. The result is retrieved by just changing δ by $-\delta$ in eq. (2.65) (one also has to take into account a phase shift of π). The amplitude of the generated fields are given by eq. (2.44) and the detector measures the interference between the probe field and the two sidebands that are generated by the FWM process (they are denoted as $E_{r,+}(t)$ and $E_{r,-}(t)$) , that is

$$I = c\epsilon_0 |E_p(t)+E_{r,+}(t)+E_{r,-}(t))|^2. \tag{2.66}$$

The components of the intensity that oscillates at a frequency δ are

$$\begin{aligned}I = \frac{\hbar\omega L(\rho_{ee}^{eq}-\rho_{gg}^{eq})\Omega_{\pm}\Omega_p^2\Omega_c\sqrt{\pi}e^{i\delta t+\phi_t}}{16ku} \sum_{l=g,e} \frac{1}{i\delta+\Gamma_{ll}} \\ \times \left\{ \frac{1}{\Gamma_{eg}+i(\omega_{ge}+\omega+\frac{\Delta}{2}+\delta)} - \frac{1}{\Gamma_{eg}+i(\omega_{ge}+\omega+\frac{\Delta}{2}+\frac{\delta}{2})} - \right. \\ \left. - \frac{1}{\Gamma_{eg}-i(\omega_{ge}+\omega+\frac{\Delta}{2}-\delta)} + \frac{1}{\Gamma_{eg}-i(\omega_{ge}+\omega+\frac{\Delta}{2}-\frac{\delta}{2})} \right\} + c.c.\end{aligned} \tag{2.67}$$

Therefore, the probe field act as a local oscillator and the intensity retrieved after demodulation at frequency ω can be, as usual, decomposed in two terms. One term is proportional to $\cos(\delta t+\phi_T)$ and the other to $\sin(\delta t+\phi_T)$ (ϕ_T is the summation of

the phases that appear in eq. (2.60)). By defining the functions $L_n = \frac{1}{1+\frac{(\omega+\frac{\Delta}{2}-\omega_{eg}-n\delta)^2}{\Gamma_{eg}^2}}$ and $D_n = \frac{(\omega+\frac{\Delta}{2}-\omega_{eg}-n\delta)}{1+\frac{(\omega+\frac{\Delta}{2}-\omega_{eg}-n\delta)^2}{\Gamma_{eg}^2}}$, we can write eq. (2.67) as

$$I = \frac{\hbar\omega L(\rho_{ee}^{eq}-\rho_{gg}^{eq})\Omega_{\pm}\Omega_p^2\Omega_c\sqrt{\pi}e^{i\delta t+\phi_t}}{16ku\Gamma_{eg}^2}\sum_{l=g,e}\frac{1}{\delta^2+\Gamma_{ll}^2}$$
$$\times\,(L_1 - L_{\frac{1}{2}} + L_{-\frac{1}{2}} - L_{-1})\cos(\delta t+\phi_T) + (-D_1 + D_{\frac{1}{2}} + D_{-\frac{1}{2}} - D_{-1})\sin(\delta t+\phi_T). \tag{2.68}$$

The expression in eq. (2.68) was introduced in [48]. The lineshape that is retrieved by demodulation of the signal proportional to $\cos(\delta t+\phi_T)$ represented in eq. (2.68) is shown in fig. 2.14. The dispersive signal is shown in a flat background, which is one of the main features of this type of spectroscopy, i.e. the absence of a Doppler structure. This fact makes the present signal less sensitive to temperature fluctuations of the vapour cell than signals generated by FM spectroscopy. Finally, the signal is not centered at the origin of the frequency axis because the resonance condition is shifted by $\frac{\Delta}{2}$. This shift in the resonance condition due to a difference in frequency between pump and probe beam is well known and was reported in [49].

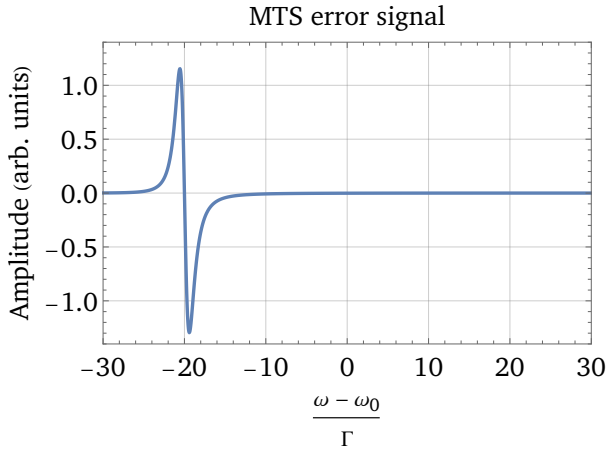

FIGURE 2.14: Typical error signal generated by MTS for a modulation frequency of $\delta = 0.1\Gamma$ and $\Delta = 40\Gamma$. The width of the Doppler profile is 20Γ.

2.5 Conclusion of the chapter

Four frequency stabilization techniques were presented. Typical experimental schemes and the derivation of the error signals were shown for all of them. The error signal slope and capture range for the two cavity-based techniques (PDH and HC) were shown and, therefore, a comparison between them could be performed. It was shown that the error signal slope for typical cavities is higher for the PDH technique when high modulation frequencies are applied. However, it can be advantageous to use HC technique if one looks for a good compromise between error

signal slope and capture range. Another advantage of the HC technique is that it consumes less energy, because it does not lie on frequency modulation, avoiding RF electronic equipment.

FM spectroscopy and MTS were also introduced. They are laser frequency stabilization methods that lie on the spectroscopy of atomic or molecular transitions. They have the advantage of being based on the spectroscopy of absolute frequency references. However, modern optical cavities can have linewidths well below typical linewidths of atoms and molecules that are suitable for vapour cell spectroscopy at room temperature [50]. A calculation of the generation of the error signal by MTS was performed for the two-level case. It was shown that the advantage of MTS over FM spectroscopy is that it is less sensitive to the Doppler contribution to the error signal background, which makes it less sensitive to fluctuations of the temperature of the vapour cell. MTS is used in chapter 4 to stabilize the frequency of the laser used to load a magneto-optical trap of ^{174}Yb operating on the $^1S_0 - {}^3P_1$ transition.

Chapter 3

Magneto-optical trapping of ^{174}Yb atoms on the $^1S_0 - {}^1P_1$ transition

The main objective of the present doctoral thesis is the building of an ytterbium magneto-optical trap (MOT) to perform experiments aiming at the observation of localization of light in three dimensions. The choice of Yb instead of other atomic species is justified in Chapter 1, alongside its relevant properties. Details on the oven system and atomic beam, as well as a deep analysis and optimization of the MOT on the $^1S_0 - {}^1P_1$ transition (that will be called "blue MOT" in the thesis) are available in [51]. In this chapter I will introduce the experimental scheme, together with the results on the blue MOT. However, the focus of the chapter is the laser system used to load the blue MOT. The strategy adopted by us consists in firstly optimizing the number of atoms in the blue MOT, then an optimization of the transfer from the blue to a MOT operating in the $^1S_0 - {}^3P_1$ (green MOT) is performed. However, directly loading of a green MOT was reported by other groups [30, 52] and has advantages that will be mentioned in the next chapter.

The first section of the chapter is designed to justify the use of the $^1S_0 - {}^1P_1$ transition for a reader that is not familiar with laser cooling of alkaline-earth type atoms. The basic equations that explain the forces that arise from the light-matter interactions described here will not be derived. The literature covering general and basic topics on laser cooling and trapping of neutral atoms is vast and will be cited as the results are used.

The experimental apparatus is introduced in the second section. Special attention is paid to the laser system, which is composed of three subsystems (a pump laser, one titanium-Sapphire laser and a SHG cavity). Details on the laser scheme and the optimization of the two last subsystems are given alongside data describing the output power of these systems when optimized. This section is important because it shows the benchmark of our laser system and can be useful to other groups working with similar high-power laser systems.

The results on the Yb magneto-optical trap obtained in the $^1S_0 - {}^1P_1$ transition are shown in the third section. The data shows that up to 1×10^9 atoms are trapped with a loading rate of up to $3 \times 10^9\,\mathrm{s}^{-1}$. It is finally concluded that the number of captured atoms in the blue transition is higher than what was previously reported.

However, different experimental schemes could be used to load more atoms directly on the $^1S_0 - {}^3P_1$ transition.

3.1 Fundamentals

The achievement of the MOT was a milestone in the atomic physics community. Since its first observation in 1987 [53] it has been widely used for numerous applications such as quantum information [54] and gravimetry [55, 56]. It was also crucial for the first observations of Bose-Einstein condensates [57, 58]. The first observation of collective effects in cold atomic samples was reported in the beginning of the 90's [59], by the observation of long-range repulsive force between the atoms.

3.1.1 Laser cooling of neutral atoms

The possibility of using light to slow down atoms in a vapor was reported by Theodor Hänsch and Arthur Schawlow in 1975 [60]. Such idea was based on a previous experiment by Arthur Ashkin that showed the deflection of an atomic beam due to radiation pressure [61]. The first, and main, role of the blue laser in this experiment is to cool down the maximum number of atoms from an atomic beam that is generated by an oven filled with ytterbium.

An atom with velocity v interacts with three pairs of counterpropagating laser beams (one pair for each spatial direction) described by plane waves of wavenumber k. The mean radiation pressure force acting on the atom is [62, 63]

$$F(v) = \pm\frac{\hbar k\Gamma}{2}\frac{I}{I_{sat}}\frac{1}{\{1+\frac{I}{I_{sat}}+[2(\Delta\mp kv)/\Gamma]^2\}}. \tag{3.1}$$

The upper sign indicates the force by a light beam that propagates in the same direction as the atom and the lower sign the force exerted by a light beam that propagates in the opposite direction. Δ represents the detuning of the light with respect to the atomic transition, i.e. $\Delta = \omega_0 - \omega$, where ω_0 is the resonant frequency of the atomic transition and ω is the laser frequency. Γ represents the transition linewidth, $\hbar = \frac{h}{2\pi}$ where h is the Planck constant, I is the beam intensity and I_{sat} is the saturation intensity of the transition.

For $I << I_{sat}$, one can see on eq. (3.1) that $F(v) \propto I$. However, if $I >> I_{sat}$ the force becomes independent of I. The maximum deceleration that an atom can experience occurs when $\Delta + kv = 0$, and is given by $|a| = \frac{\hbar k\Gamma}{2m(1+\frac{I_{sat}}{I})}$ where m is the mass of the atom. In the limit $I >> I_{sat}$ the modulus of the deceleration is reduced to

$$|a| = \frac{\hbar k\Gamma}{2m}. \tag{3.2}$$

Hence, the maximum deceleration depends linearly with respect to the transition linewidth. In the case of ytterbium atoms, the linewidth of the $^1S_0 - {}^1P_1$ transition (Γ_b) is about 160 times larger than the one of the $^1S_0 - {}^3P_1$ transition (Γ_g). Due to

this result, the blue laser is often used in Zeeman slowers [64] in order to decelerate atoms from an atomic beam. In our experiment, we have decided to not employ a Zeeman slower to have a more compact experimental system and also to avoid unwanted magnetic field around the MOT region. Instead, we make use of a single frequency blue laser beam that is (nearly) counterpropagating to the atomic beam. We call this laser beam as "slowing beam", and its effectiveness will be shown later in this chapter.

The equilibrium temperature of an atomic cloud that is under the action of a force like eq. (3.1) is [63]

$$T = \frac{\hbar\Gamma}{8k_B}\frac{\Gamma}{|\Delta|}\left(1 + \frac{I_{tot}}{I_{sat}} + \frac{4\Delta^2}{\Gamma^2}\right). \tag{3.3}$$

Where k_B is the Boltzmann constant and I_{tot} is the sum of all MOT beam intensities. This temperature is minimum for low intensities (i.e. $I \ll I_{sat}$) and $\Delta = \frac{\Gamma}{2}$, this minimum temperature is called Doppler temperature and it is given by

$$T_D = \frac{\hbar\Gamma}{2K_B}. \tag{3.4}$$

Eq. (3.4) shows that the minimum temperature achieved by Doppler cooling mechanisms depends linearly with respect to the linewidth of the cooling transition (Γ). This is one of the reasons why a MOT in the $^1S_0 - {}^3P_1$ Yb intercombination transition is more convenient for experiments on localization of light by cold atoms. The Doppler temperature for laser cooling on the $^1S_0 - {}^1P_1$ Yb transition is more than 160 times bigger than for the $^1S_0 - {}^3P_1$ Yb transition. This means that the atoms cooled down by the blue transition would move faster than atoms cooled down by the green one, which could affect localization effects in typical time scales of experiments (limited by the response time of currently available detectors).

3.1.2 Magneto-optical trap

A MOT consists of three pairs of circularly polarized counterpropagating beams and a pair of coils in the anti-Helmholtz configuration that generates a spatial gradient of magnetic field in the three spatial directions. The laser should be red-detuned with respect to the atomic transition (i.e. $\Delta < 0$). Such scheme is represented in fig. 3.1 for the 1D case and for atoms with a nondegenerate ground state ($J = 0$) and three-fold degenerate excited state ($J = 1$).

The spatial gradient of magnetic field breaks the degeneracy of the excited state and makes the radiation pressure force spatially dependent. Limiting our analysis to one dimension, introducing the term related to the Zeeman shift, i.e. $\pm\gamma_J \nabla B_z z$ for $\gamma_J = \frac{g_J \mu_B}{\hbar}$ where g_J is the Landé factor of the excited state and μ_B the Bohr magneton, in eq. (3.1) and expanding the remaining expression in a Taylor series until the first order in velocity and position (assuming that the Doppler and Zeeman shifts are

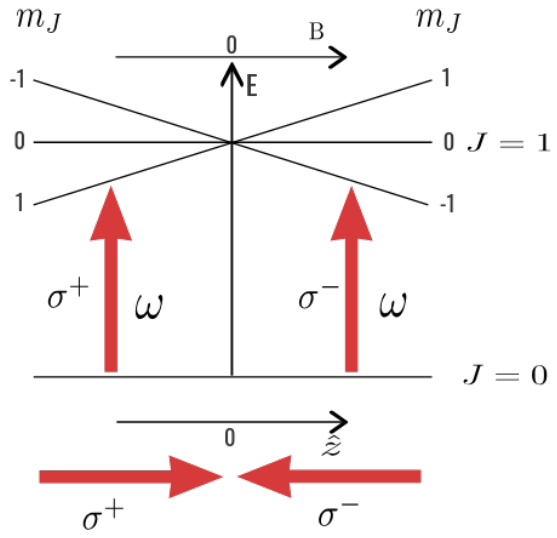

FIGURE 3.1: Representation of the interaction between an atom with a nondegenerate ground state and a 3-fold degenerate excited state with a pair of counterpropagating circularly polarized laser beams that couples transitions between the ground state and two different magnetic sublevels in the presence of a magnetic field that varies linearly with respect to the position. **Source:** [65]

.

small with respect to Γ), we obtain for the net force acting in the atom [62, 63]

$$F(z,v) = -\alpha v - \beta z. \tag{3.5}$$

Where

$$\alpha = 8\hbar k^2 \frac{|\Delta|}{\Gamma} \frac{I}{I_{sat}} \left\{ \frac{1}{1 + \frac{2I}{I_{sat}} + (\frac{2\Delta}{\Gamma})^2} \right\}^2, \tag{3.6}$$

$$\beta = 8\hbar k \gamma_J \nabla B_z \frac{|\Delta|}{\Gamma} \frac{I}{I_{sat}} \left\{ \frac{1}{1 + \frac{2I}{I_{sat}} + (\frac{2\Delta}{\Gamma})^2} \right\}^2. \tag{3.7}$$

The restoring force is derived from a potential ($\frac{\beta\langle z^2\rangle}{2}$), therefore for a low density MOT (i.e. no collective effects) at equilibrium

$$\Delta z = \sqrt{\frac{k_B T}{\beta}}. \tag{3.8}$$

Assuming that the Doppler temperature is achieved, the size along the z axis is given by

$$\Delta z = \sqrt{\frac{\Gamma I_{sat}}{2k\gamma_J \nabla B_z I}}. \tag{3.9}$$

In this case, the size of the cloud does not depend on the number of trapped atoms. Thus, the density of the atomic cloud is proportional to Δz^{-3}. We can now conclude

that in the low density case the density of the cloud is proportional to $\Gamma^{-\frac{3}{2}}$, which indicates the advantage of narrow transitions over broad ones for experiments at which high atomic densities are desired.

To calculate the density of the atomic cloud at the limit of higher densities one should consider the excitation of one atom by a photon that was scattered by another atom. It is also assumed that the photons scattered by an atom have the same frequency of the incident ones. This effect gives rise to a repulsive interaction that increases the size of the MOT. This model is known as the Wieman model and shows that the maximum atomic density (n_0) of the cloud is given by [66, 67]

$$n_0 = \frac{16\pi\gamma_J \nabla B_z |\Delta|}{3\hbar\lambda^2\Gamma^2}, \tag{3.10}$$

where λ is the wavelength of the MOT beams. From eq. (3.10), we still conclude that higher densities can be achieved for narrower lines, i.e. the smaller the Γ of the transition the bigger the atomic density will be if the other parameters remain the same. We can also conclude that the atomic density has a linear dependence with respect to the magnetic field gradient and laser detuning. Then, in principle, it is possible to achieve high atomic densities even for transitions with broad linewidths. A limitation regarding the laser detuning is given by eq. (3.3), which states that the temperature of the cloud increases if the laser detuning is increased.

Eqs. (3.9) and (3.10) emphasizes that we should use the Yb $^1S_0 - {}^3P_1$ transition to achieve MOTs that may be suitable to perform experiments aiming at the observation of localization effects. However, we are also interested in trapping a large number of atoms. Then, we load a blue MOT, that is, in principle, able to trap more atoms than a green MOT, due to the larger damping force that is applied to the atoms (eq. (3.6)). After loading the blue MOT, the atoms are transferred to a green MOT to achieve higher densities. The first results on the transfer of a blue to a green MOT will be shown in the next chapter. Whereas, in the end of this chapter a brief description of the blue MOT will be given.

3.2 Experimental apparatus

One important part of this thesis work was the installation and maintenance of the laser system. Since the saturation intensity of the blue transition is $63\,\mathrm{mW/cm^2}$, which is high in comparison to the green one ($0.14\,\mathrm{mW/cm^2}$), the blue laser system plays an important role for the experiment. Regular maintenance and optimization of this laser system was required during four years, especially due to the moving of the laboratory from one building (in Sophia-Antipolis) to a new one (in Nice). The high saturation intensity of the blue transition is also the reason why a system that can deliver up to 2.5 W at around 399 nm was chosen for this project. This section will describe the laser system, the details of the oven and the design of the vacuum

system are a part of the PhD thesis of Hector Letellier [68] that was developed in parallel to the present one and on the same system.

The oven and vacuum setup is shown in fig. 3.2. The oven (OEM S40 DZ35 K, Riber) can be heated to up to 1000 °C, however the maximum temperature at which we operate it is 500 °C. With this oven we can heat a crucible body and the output nozzle separately. A shutter is included in front of the oven and can be opened or closed mechanically from the outside. A bellow is used to correct a small misalignment of the oven with the central axis of the science cell. An array of stainless steel micro-tubes (AISI-304) is placed in the oven output to increase its lifetime.

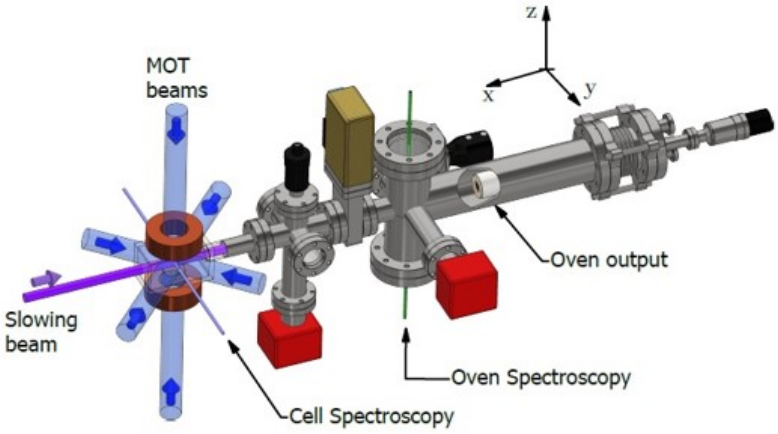

.

FIGURE 3.2: Representation of the vacuum setup. From the right to the left: oven flange and bellow; oven output; UHV cross with two window ports used for spectroscopy, one ion-getter pump and a mechanical valve; pneumatic valve; a second UHV cross with two additional window ports, a mechanical shutter and a second ion-getter pump; science cell .with a pair of coils in the anti-Helmholtz configuration, three pairs of counterpropagating beams (MOT beams) and the slowing beam. **Modified from:** [51].

An ultra-high vacuum (UHV) cross connects an ion-getter pump (75L/s-N2, NEXTorrZ200, SAES) to a manual UHV valve (mini UHV Gate Valve CF40, VAT). The UHV cross also contains two window ports, that were used to perform transverse spectroscopy of the atomic beam. A pneumatic valve (mini UHV Gate Valve CF40, VAT) separates the oven from the science cell part, this allows the preservation of the vacuum in the cell part while the oven is being heated and when the oven needs to be refilled with ytterbium. Two differential pumping tubes with 40 mm of length and 12 mm of diameter are placed before and after the pneumatic valve. Before the science cell, a second UHV cross is connected to add another ion getter pump (75L/s-N2, NEXTorrZ200, SAES), one mechanical shutter and two additional window ports. Finally, the science cell (Japan cell) which is broadband coated for 399 nm to 700 nm and has a rectangular shape (50 mm X 50 mm X 100 mm). Two coils in the anti-Helmholtz configuration are positioned below and above the cell.

In fig. 3.2 we can also see the three pairs of counterpropagating MOT beams and the slowing beam. Their color difference is only for illustrative purposes, since their difference in frequency is only of a few hundreds of MHz.

3.2.1 Laser system

To generate the beams depicted in fig. 3.2 a long laser setup is used, as shown in fig. 3.3. A laser (Verdi V18) with an output power of up to 18.5 W at 532 nm is used to pump a Titanium-sapphire laser (M Squared SolsTiS) that delivers up to 6 W at 798 nm. The optical power of the pump laser can be measured by a photodiode (PD 1) due to the reflection of a polarizing beamsplitter (PBS 1) that can be adjusted by a $\frac{\lambda}{2}$ plate. The mirrors M1 and M2 are used to align the pump beam to the Titanium-sapphire (Ti:Sa) cavity and between M2 and the Ti:Sa laser there are two lenses to match the mode of the pump beam to the desired cavity mode.

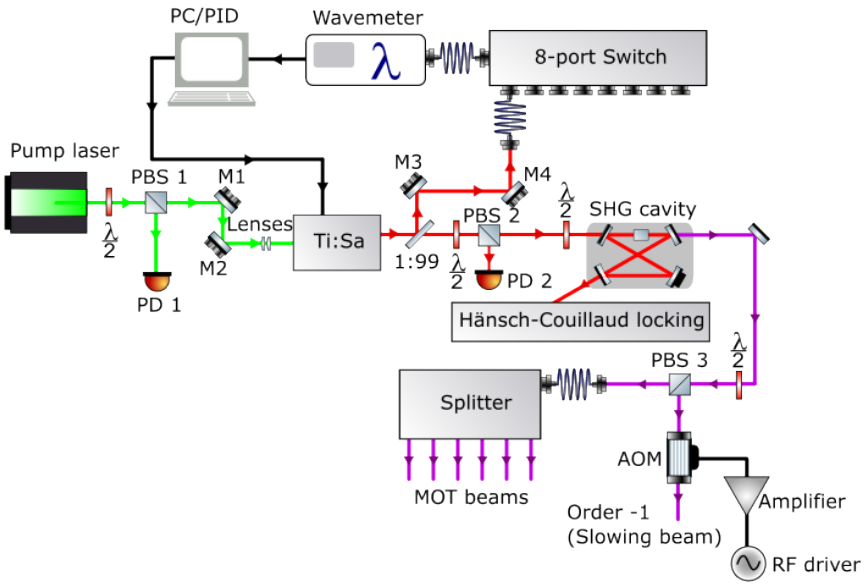

FIGURE 3.3: Simplified scheme of the blue laser system. The Ti:Sa laser is pumped by a laser that delivers up to 18.5 W at 532 nm. The Ti:Sa output is split in two by a 1:99 plate. The reflection of the plate is sent to a fibered 8-port switch that is connected to a wavelength meter to perform the frequency stabilization, the transmission (whose total power can be measured by PD 2) is sent to the SHG cavity. The cavity is stabilized by the Hänsch-Couillaud technique and it delivers up to 2.5 W at 399 nm. The cavity output passes through PBS 3, the reflection is diffracted by an AOM and used as the slowing beam, while the transmission is sent to a splitter at which it is diffracted by another AOM (not depicted) and split in six independent beams that are used as the MOT beams.

The output of the Ti:Sa is split by a plate and about 1% of the reflection is aligned by the mirrors M3 and M4 to be injected in a single-mode fiber. The fiber output is connected to an 8-port photonic crystal fiber (PCF) switch, which is connected to a commercial wavemeter (HighFinesse WS8-2). The wavemeter measures the wavelength of the Ti:Sa output and it is connected to a personal computer (PC) which has

a PID installed. The PID is connected to the Ti:Sa cavity and due to its feedback the laser frequency is stabilized. The transmission of the plate (around 99%) is either transmitted by PBS 2 or reflected. The $\frac{\lambda}{2}$ plate in front of PBS 2 can be rotated for the measurement of the Ti:Sa output power by PD 2. In daily operation the transmission of PBS 2 is maximized by the $\frac{\lambda}{2}$ plate and the laser beam passes through an additional $\frac{\lambda}{2}$ before entering the SHG cavity. The cavity is stabilized by the Hänsch-Couillaud technique (see chapter 2). The maximum output power obtained from this cavity was 2.5 W at 399 nm.

The output of the SHG cavity is split in two by PBS 3. The reflection is diffracted by an AOM and the -1 diffraction order is used as the slowing beam. The frequency delivered to the AOM by the RF driver and the amplifier is 110 MHz. The transmission of PBS 3 is coupled to a fiber that is the input of a splitter. This splitter (Muquans UFS399-1*7-01) contains two AOMs and seven beam outputs. In fig. 3.3 just the six MOT beams outputs are shown, but there is additionally one output to be used as a probe beam. The MOT beams are divided inside the splitter after being diffracted by one AOM (+1 diffracted order) that is driven by a sinusoidal signal of frequency 110 MHz. This configuration allows the frequencies of the MOT and slowing beams to be tuned simultaneously, but does not allow them to be independently tuned by frequencies that are large in comparison to the linewidth of the transition (Γ_b). The frequency difference of 220 MHz between the MOT beams and the slowing beam is sufficient to increase the number of trapped atoms compared to a MOT loaded without a slower. However, it is envisaged to use a multiple-frequency slowing beam in the future.

3.2.2 Laser optimization

It can be seen in fig. 3.3 that the system is long and has many different parameters to adjust (many coupling mirrors and three different lasers). Therefore, it is important to routinely monitor the specifications of the lasers to guarantee that no damage occurred to any of their parts during operation. It is equally important to optimize the alignment of the lasers and record the results, which would help in diagnosing any issues that may occur in the future.

The alignment of the input of the Ti:Sa and the SHG cavity will be briefly explained and the achieved results shown. This kind of data was important during this thesis work because we could identify exactly which of the parts of the system (lasers or SHG cavity) was degrading, once it happens. Indeed, the Ti:Sa laser needed two interventions from the manufacturer during this PhD work. Thus, once we needed to reinstall the laser we knew which were the standards to achieve.

The Ti:Sa input is optimized by 2 mirrors and a pair of lenses, as depicted in fig. 3.4. A typical alignment procedure is described below.

- Verify that the beam hits mirror 1 in its center and adjust the mirror position if needed (using minimum pump power for security reasons);

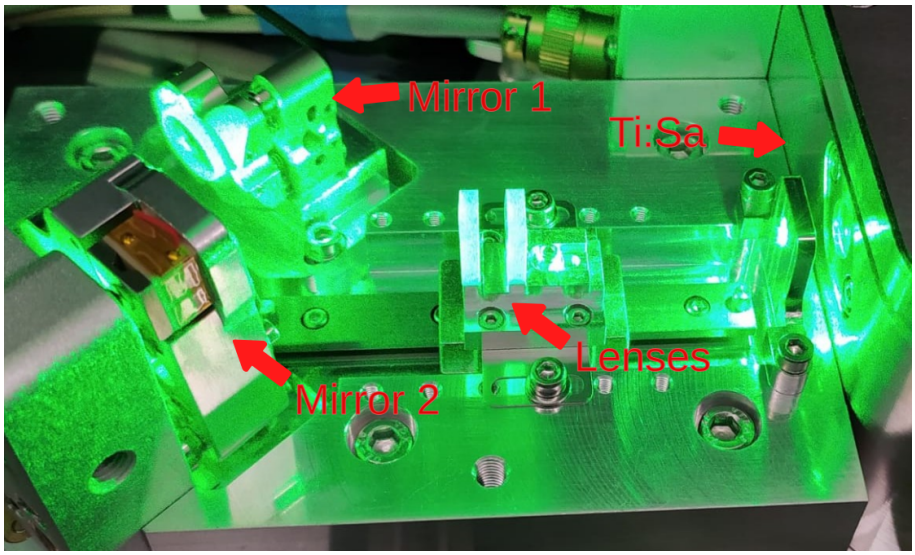

FIGURE 3.4: Photo of the input of the Ti:Sa laser. The beam propagation occurs from the left to the right. The beam hits mirror 1 and mirror 2 before passing through a pair of lenses in front of the Ti:Sa input. An aperture positioned in front of the Ti:Sa input is also visible and its role is to indicate that a good alignment of the beam should be when it is centered on mirror 2 and it passes through the aperture.

- Verify that the beam hits mirror 2 in its center and, if needed, adjust it by the screws that controls vertical (y) and horizontal (x) axis of mirror 1 (using minimum pump power for security reasons);
- Make the beam pass through the center of the aperture that is in front of the Ti:Sa in fig. 3.4 by adjusting the x and y screws of mirror 2 (using minimum pump power for security reasons);
- Increase the pump power until the expected laser threshold (about 6 W) and tune x and y screws by very small angle steps until that the system starts to lase (more IR fluorescence can be observed when the system is close to the lasing threshold).
- Insert a hex key in the x axis screw of the mirror 1 and write down the angular position of the screw. Then, rotate the screw by 90° clock wisely and optimize the output power with mirror 2. Write down the output power that was obtained.
- Repeat the previous step many times, until the laser power decreases by two consecutive steps. Then, return the screw to the position of maximum power.
- If by rotating the hex key in the clockwise direction does not improve the output power, then return the hex key to the initial angular position and perform the last two steps by rotating the hex key in the counterclockwise direction.
- Repeat the last three steps for the y axis screw.

- Once the output power is maximized, then the position of the lenses can be optimized. The screws on the border of the lenses support should be carefully loosen by assuring that the Ti:Sa remains lasing, one possibility is to loose one screw by a small amount and then loose the other by the same amount, repetitively.

- When the lenses support can be slid, this should be done by a small amount in a given direction. Then, mirror 2 should be tilted to maximize the output power. If the laser output power increases, this should be repeated until it stops to increase. If the output power decreases, the other direction should be chosen. One should not forget to write down the output of each step in order to be able to return to the initial configuration.

- Once the optimum position of the two lenses is reached, the screws should by carefully tighten again by making sure that the lasing is not interrupted.

- The second lens (from the left to the right) can be individually translated by carefully loosing the screw that holds it and sliding it in a given direction. Again, mirror 2 should be tilted to optimize the output power after each step.

This optimization steps were carefully performed after the installation of the laser and the Ti:Sa output as a function of the pump input power was recorded. The result is shown in fig. 3.5 alongside a linear fit of the data. For this Ti:Sa laser the lasing threshold was 3 W and the output power for 18.5 W of pump power was slightly above 6 W.

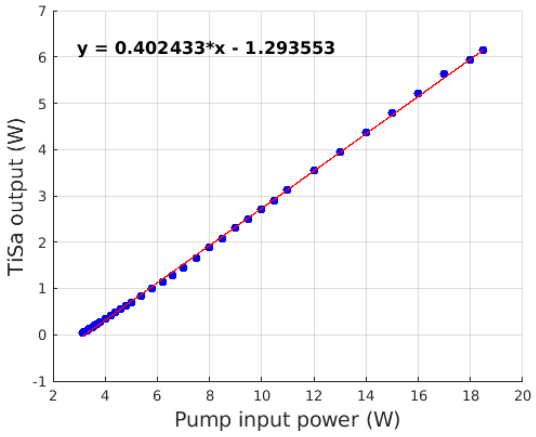

FIGURE 3.5: Ti:Sa output power with respect to the pump input power with a linear fit of the data. This data was taken after careful installation and alignment of the laser system.

Fig. 3.5 shows that for the range of pump input power that was used, the Ti:Sa output continues to increase. That is, for this range, no saturation effect was observed. We can conclude that the limitation for the Ti:Sa output is the pump input power. However, accordingly to the manufacturer of the Ti:Sa laser, damage can occur to optical components inside the laser if higher input power is used.

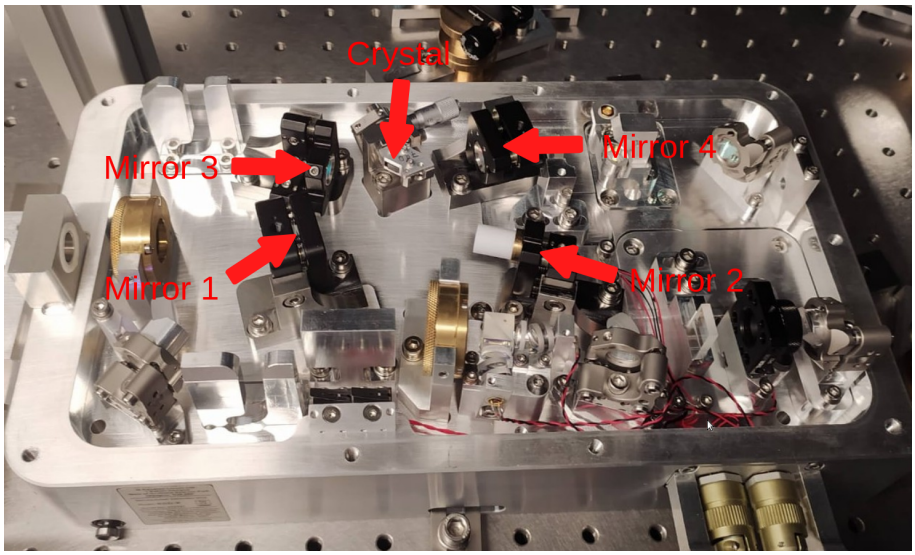

FIGURE 3.6: Photo of the SHG cavity. The mirrors are numbered accordingly to the direction of propagation of the incident beam. The beam enters the cavity by Mirror 1, Mirror 2 can be modulated by a piezo and the SHG crystal is placed between Mirror 3 and Mirror 4. The beam output is through Mirror 4.

FIGURE 3.7: Photo of the fundamental beam in the surface of the SHG crystal. The amount of light that can be seen is an indication that the crystal needs to be cleaned.

After optimizing the Ti:Sa laser, the alignment of the SHG cavity needs to be performed. Fig. 3.6 is a photo of the SHG cavity. The mirrors can be tilted by hex keys and the crystal can also be tilted by rotating a micrometer that is in its mount. It is important to emphasize that during operation dust can adhere to the SHG crystal facet, meaning that the crystal should be cleaned (the manufacturer provides the instructions for cleaning the crystal). The first indication that the crystal needs to be cleaned is a decrease in the efficiency of the SHG process, which can be confirmed by observing the input of the beam into the crystal. Fig. 3.7 is a photo of the SHG crystal before being cleaned. The brightening of the beam when hiting the crystal's facet indicates that the crystal should be cleaned (meaning that more light is being

scattered by the surface).

The alignment of the cavity is performed after the optimization of the Ti:Sa output power, and should be done as follows

- Ensure that the beam is hitting Mirror 2 on its center.
- The cavity should be scanning, which is possible by the application of a triangular signal to a piezoelectric actuator that holds mirror 2. The signal generated by the detection of the beam transmitted by the cavity should be continuously measured during the alignment. The goal is the maximization of the peak of the cavity transmission signal.
- Slightly rotate the x-axis screw of Mirror 2 in a given direction, try to maximize the signal by rotating x-axis screw of Mirror 3 in any direction. If the peak of the signal increases continue to slightly rotate the x-axis screw of Mirror 2 in the same direction and optimizing the signal with Mirror 3. If the peak decreases, rotate Mirror 3 x-axis screw in the other direction. Repeat this process for the y-axis screw of the mirrors. This step is know as **beam walking** by Mirrors 3 and 4.
- Walk the beam by Mirrors 1 and 4.
- Walk the beam by Mirrors 2 and 3.
- Carefully tilt the angle of the Crystal until the height of the transmission peak is maximized.
- Repeat the last 4 steps until no improvement is achieved anymore.
- If the height of the signal is still below the expected value, it may be needed to clean the Mirrors and/or the Crystal.

Fig. 3.8 shows the SHG output power and efficiency as functions of the incident power, after optimization. A maximum power of 2.5 W for an input power of 6 W was measured, which corresponds to a SHG efficiency of more than 40%. Fig. 3.8b shows that the SHG efficiency increases by increasing the input power for the whole range that was measured.

3.3 Blue MOT

The laser optimization and maintenance discussed before is important for the long-term usage of the laser system. The main objective in acquiring a laser system that delivers up to 2.5 W of power at 399 nm was to trap the maximum amount of atoms in the Yb $^1S_0 - {}^1P_1$ transition.

The MOT beams shown in fig. 3.3 are sent to six independent optical cage systems that contains $\frac{\lambda}{2}$ and $\frac{\lambda}{4}$ plate to adjust the polarizations and two lenses (one

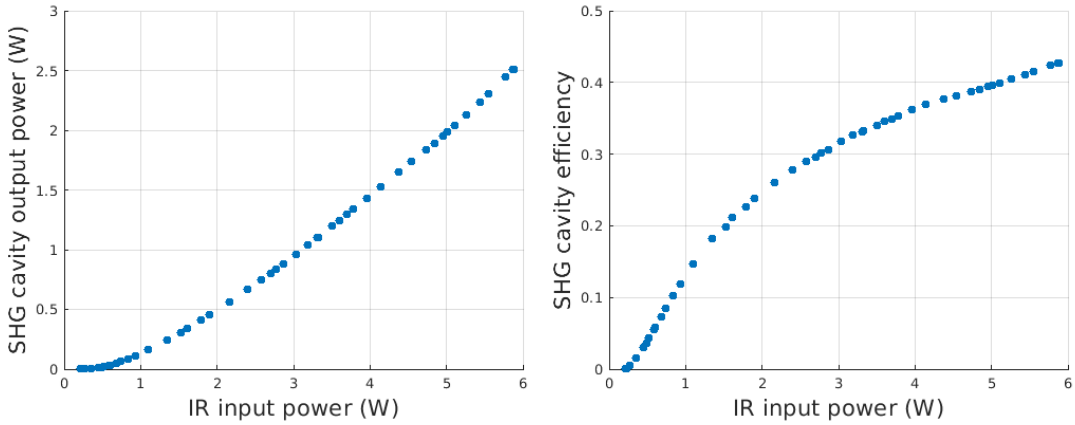

(A) (B)

FIGURE 3.8: (A) SHG output power and (B) SHG efficiency as a function of the input power for an input at 798 nm, after cavity optimization.

aspheric lens of focal distance 7.5 mm and a two-inches plano-convex lens of focal distance 150 mm). In the position of the MOT the beams have a waist of 22 mm. The drivers of the AOM splitter and the slowing beam AOM are controlled by a high-speed analog output device (*National instruments* PCIe-6738), which also allows synchronized control of the devices that are used in a typical experimental time sequence (AOMs, cameras, detectors).

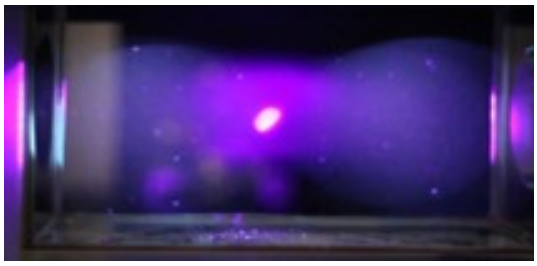

FIGURE 3.9: Photo of the magneto-optical trap obtained by the $^{174}Yb\ ^1S_0 - {}^1P_1$ (blue) transition.

Fig. 3.9 shows a typical MOT obtained in our experiment. The effect of the slowing beam can be seen in fig. 3.10, which shows the number of atoms measured by the fluorescence of the MOT as function of time. The measurements are taken for three different nozzle temperatures, while the other parameters are kept constant. The parameters used for these measurements were: $\Delta = -2\Gamma_b$, $\nabla B_z = 32\,\mathrm{G\,cm^{-1}}$, MOT beams power of 19 mW for each of the horizontal beams and 12 mW for the each of the vertical ones and the power of the slowing beam was 300 mW. In fig. 3.10, the MOT beams are turned on for 10 s (from -20 s to from -10 s) without slowing beam. The slowing beam is turned on at -10 s and then turned off at 0 s. The number of atoms typically increases by one order of magnitude when the slowing beam is on, highlighting its efficiency.

The loading rate and the stationary number of atoms for 19 different nozzle temperatures (from 285 °C to 455 °C) are shown in fig. 3.11. The loading rate and the

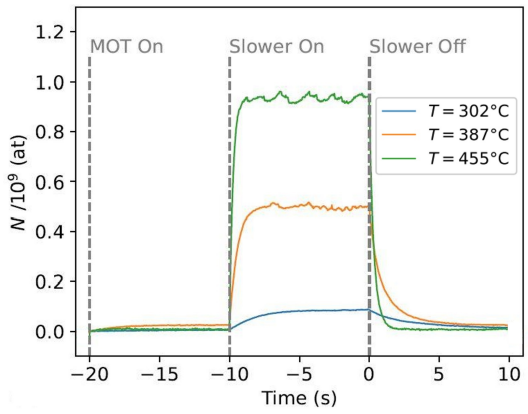

FIGURE 3.10: Number of atoms in the MOT for three different nozzle temperatures ($T_{blue} = 302\,^\circ$C, $T_{orange} = 387\,^\circ$C, $T_{green} = 455\,^\circ$C), measured by fluorescence. The other parameters were kept constant (see text). **Modified from:** [51].

number of atoms increase until around 440 °C. A detailed study of the limitations of this trap is also one of the main topics of another PhD thesis [51, 68].

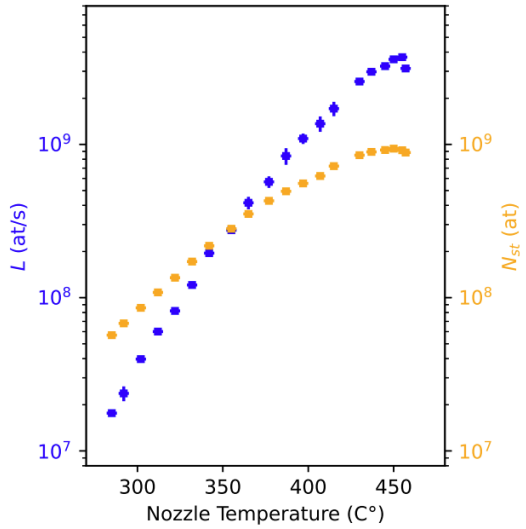

FIGURE 3.11: Loading rate (in blue) and stationary number of atoms (in orange) as a function of the nozzle temperature for 19 different temperatures. Data were taken for the same parameters as in fig. 3.10. The uncertainties are the difference between two independent measurements. **Source:** [51].

We can now compare the results shown above with previously reported results. Many results involving MOTs of Yb on the $^1S_0 - {}^1P_1$ transition reported the trapping of less than 1×10^8 atoms [69–72] with various experimental configurations. The trapping of 5×10^8 atoms with a loading rate of $1 \times 10^9\,\mathrm{s}^{-1}$ by employing a Zeeman slower followed by a 2D MOT was reported in [73]. However, the trapping of more than 1×10^9 atoms was only achieved by directly loading the MOT in the $^1S_0 - {}^3P_1$ transition either by arranging blue and green laser beams in a core-shell geometry [52] or by loading for a few seconds at high saturation intensity [30], in both cases a Zeeman slower was employed (slowing on the $^1S_0 - {}^1P_1$ transition).

One important constraint of our experimental scheme is the accumulation of ytterbium atoms on the window of the science cell that faces the entrance of the oven. Since this window is the entrance of the slowing beam into the science cell, the power of the slowing beam is attenuated in the cell window diminishing its effectiveness, and we had to incline the slowing beam by a small angle with respect to the propagation direction of the atomic beam. To maintain the slowing beam effective we regularly hit the ytterbium coating by focusing the light emitted by an array of LEDs (light-emitting diodes), that has a total output power of 15 W at 450 nm. This procedure slowly removes the undesired Yb coating.

3.4 Conclusion of the chapter

The $^1S_0 - {}^1P_1$ transition is used in a first step to decelerate and trap the maximum amount of atoms. The higher deceleration of atoms by using this transition is due to its broader linewidth. However, the minimum temperature that can be achieved by the Doppler cooling mechanism (Doppler temperature) is directly proportional to the linewidth of the transition. Therefore, the minimum temperature of a Yb MOT (in the absence of sub-Doppler cooling mechanisms) operating in the $^1S_0 - {}^1P_1$ transition is about 150 times hotter than one operating in the $^1S_0 - {}^3P_1$ transition (the values are, respectively, 670 µK and 4.4 µK). Additionally, the density of the atomic cloud does also depend on the linewidth of the atomic transition, being larger for narrower lines for the same experimental parameters (magnetic field gradient and laser detuning in units of the linewidth).

The experimental setup, chosen due to its compactness (i.e. the absence of a Zeeman slower), was presented with a detailed description of the laser system which is composed by a pump laser, a Ti:Sa laser and a SHG cavity. An algorithm for the alignment of the Ti:Sa laser input was discussed followed by data showing the Ti:Sa laser output power (at 798 nm) with respect to the input power (at 532 nm). A maximum of 6 W of output power for 18.5 W of input was obtained. The alignment of the SHG cavity was also detailed and the data showing the cavity output power and efficiency (at 399 nm) with respect to the input power shown. The maximum SHG cavity output power obtained was 2.5 W for an input of 6 W. The doubling (SHG) efficiency, when optimized, was more than 40%.

Finally, it was shown the MOT obtained with the presented setup. The use of a slowing beam (instead of a Zeeman slower) increases the number of trapped atoms and up to 1×10^9 atoms can be trapped. The loading rate at 450 °C was 3×10^9 atoms s^{-1} which allows the experiment to be performed with duty cycles of a few seconds. These results will play an important role in the next chapter when an analysis of the green MOT will be performed.

Chapter 4

Magneto-optical trapping of ^{174}Yb atoms on the $^1S_0 - ^3P_1$ intercombination transition

In chapter 1 the choice of Yb atoms for our experiment was justified, while in chapter 3 a discussion on the role of each of the transitions used for laser cooling of Yb atoms was provided. The experimental setup allowing to trap up to 1×10^9 atoms was also introduced in the previous chapter and naturally the present chapter is dedicated to the transfer of the atoms to a magneto-optical trap operating in the $^1S_0 - ^3P_1$ transition to achieve a colder and denser atomic cloud.

While in chapter 3 the main concern regarding the laser system was the total output power, which is justified by the large saturation intensity of the $^1S_0 - ^1P_1$ transition, now the frequency stabilization of the laser will be in the center of the discussion. Indeed, this is justified by the narrow linewidth of the $^1S_0 - ^3P_1$ transition ($\Gamma_g = 2\pi \cdot 182$ kHz) and by the difficulties in obtaining a proper vapour cell to perform spectroscopy directly on an Yb cell [74]. Therefore, we have chosen to use a molecular iodine ($^{127}I_2$) line as a frequency reference to our laser. A study of such line will be performed by comparing it to other lines that were previously studied in details.

The line used here is weaker than the $^{127}I_2$ transitions reported before. Therefore, we implement modulation transfer spectroscopy (MTS) alongside balanced detection. After explaining the experimental details, an analysis of the stability of the laser will be performed by means of the noise power spectral density (NPSD) and Allan deviation of the laser fractional frequency.

The third section of the chapter is dedicated to the transfer of the atoms from the blue to the green MOT. We show the results obtained by varying a set of parameters independently. To analyze the atomic cloud we performed time-of-flight measurements. We characterize the cloud's temperature, number of atoms, on-resonance optical depth (b_0) and atomic density (n_0). Spectroscopy of the magneto-optical trap was also performed to make a link between the absolute frequencies of $^{127}I_2$ hyperfine lines and the $^1S_0 - ^3P_1$ transition of ^{174}Yb, such results are detailed in the end of the chapter.

Finally, the chapter is concluded by discussing the applicability of the obtained atomic cloud to experiments aiming the observation of collective effects in cold atoms alongside perspectives to improve the MOT. A discussion on possible applications of the laser frequency stabilization scheme itself is also done by indicating other iodine lines, similar to the ones used in this work, that can be used for different applications.

4.1 Molecular Iodine as frequency reference for ^{174}Yb

Precise spectroscopy of many different $^{127}I_2$ lines were already reported. Indeed, $^{127}I_2$ are known to have transitions available over a wide range of the visible spectrum. Sub-Doppler spectroscopy of $^{127}I_2$ molecules was reported for lines at 534 nm [75], 548 nm [76], 554 nm [77], 578 nm [78], 739 nm [79], 541 nm [80], 612 nm [81], 671 nm [82], etc. Recently, laser frequency stabilization by using a hyperfine component of the P(49)24-1 $^{127}I_2$ line as reference for laser cooling of ^{174}Yb in the $^1S_0 - {}^3P_1$ transition was shown [83]. The frequency shift used to reach the resonance of the ^{174}Yb in the $^1S_0 - {}^3P_1$ transition was achieved by the use of three AOMs, two of them in double-pass configuration. Precise spectroscopy of all of the hyperfine componentes of the P(49)24-1 $^{127}I_2$ line was reported in [84]. They reported the absolute frequencies measured by using an optical frequency comb. The uncertainty of their measurements was 7 kHz. They have also reported the frequency shifts of the lines due to laser power ($-2.6\,\mathrm{kHz\,mW^{-1}}$) and pressure ($-1.8\,\mathrm{kHz\,Pa^{-1}}$).

Instead of using the P(49)24-1 $^{127}I_2$ line as a reference we have chosen the R(158)25-0 line, which has the advantage of being closer to the ^{174}Yb $^1S_0 - {}^3P_1$ transition. However, such lines are weaker than the previous one. Balanced detection was performed to cancel common-mode noise of the MTS probe and a probe beam used for linear absorption of the vapour cell. In this section the details about the spectroscopy of the R(158)25-0 $^{127}I_2$ line will be given which includes an estimation of the absolute frequency of its hyperfine components.

4.1.1 Experimental scheme

The main concern regarding the laser system used for laser cooling at the $^1S_0 - {}^3P_1$ ^{174}Yb transition was its frequency stability due to the linewidth of the transition (Γ_g) that is narrower than the one of the $^1S_0 - {}^1P_1$ transition, excluding the possibility of using the laser frequency stabilization method used for the blue laser (a PID feedback with a wavelength meter). In fact, during the present thesis work, we were able to load a ^{174}Yb MOT in the $^1S_0 - {}^3P_1$ transition by stabilizing the green laser with the commercial wavelength meter. However, the number of atoms in the obtained MOT was very small, probably because the feedback loop was not fast enough to correct frequency deviations larger than transition linewidth (Γ_g).

The system used for the laser frequency stabilization by balanced detection and MTS of the R(158)25-0 $^{127}I_2$ line is shown in fig. 4.1. The details of the laser system

(Toptica TA-SHG pro) are not depicted. The laser is composed by the fundamental diode laser that delivers up to 50 mW at 1112 nm, a tapered amplifier that amplifies to about 1.8 W and a SHG cavity that generates up to 1.3 W at 556 nm. The SHG cavity is stabilized by the Pound-Drever-Hall technique (see chapter 2).

The output of the SHG cavity is split into two inside the laser box by the addition of a $\frac{\lambda}{2}$ plate and a PBS (that are not depicted in fig. 4.1). One of the beams passes through a free-space output to perform the laser frequency stabilization by MTS. The other beam is sent to a fibered output that has AOM 2 connected (Brimrose TEM-150-9-60-556-2FP-HP). After AOM 2 the beam is split into six beams by a fibered splitter and used to load the MOT (not depicted). The free space output passes through a $\frac{\lambda}{2}$ plate and PBS 1. The transmission of PBS 1 is diffracted and modulated by AOM 1. The alignment of AOM 1 is performed to maximize the -1 diffraction order, which is transmitted by PBS 4 and passes through the iodine cell before being transmitted by PBS 3 when it is blocked by a beam dump (not depicted). This beam will be referred as "pump beam" from now on.

The reflection of PBS 1 passes through another $\frac{\lambda}{2}$ plate and PBS 2 to control its total power. Then, it is split into two beams by PBS 3. The transmission of PBS 3, that will be called "linear probe beam", passes through the iodine cell and is detected by PD+. The reflection of PBS 3, that will be called "MTS probe beam", passes through the iodine cell counterpropagating to the "pump beam" and it is reflected by PBS 4 to be detected by PD-. All the beams have a full width at $1/e^2$ of 0.75 mm at the position of the cell. PD+ and PD- are, in fact, the inputs of a free space differential photodetector (Thorlabs PDB210A/M). Therefore, the signals are subtracted and amplified before being sent to the radio frequency (RF) input of an RF mixer. AOM 1 is driven by a sinusoidal signal of frequency 80 MHz that is generated by a direct digital synthesizer (DDS, 2023A Aeroflex). The synthesizer's signal is frequency modulated by another sinusoidal signal of frequency 200 kHz (with a modulation index of 10), that is generated by a function generator (B&K Precision 4052). The output of the function generator is also sent (after adjusting its phase) to the local oscillator (LO) input of the RF mixer to perform the demodulation of the signal.

The output of the RF mixer is sent to the input of a PID controller (Fast Analog Linewidth Control, FALC 110), which has a slow output (unlimited integrator) with a bandwith of 10 kHz and a high bandwidth output with a bandwidth of ~ 10 MHz. The slow output is used to control the voltage applied to a piezo actuator that holds the laser grating, while the fast one controls the laser diode's current. It is important to highlight that the high bandwidth output is a module composed by four circuits (slow integrator, extra slow integrator, fast differentiator and fast integrator) and the gain given to the input signal is frequency-dependent and is the result of the combination of the gain applied to each circuit individually, which is manually defined by switches that can be turned on/off in the front panel of the device. The FALC configurations used in this work will be discussed later in the text.

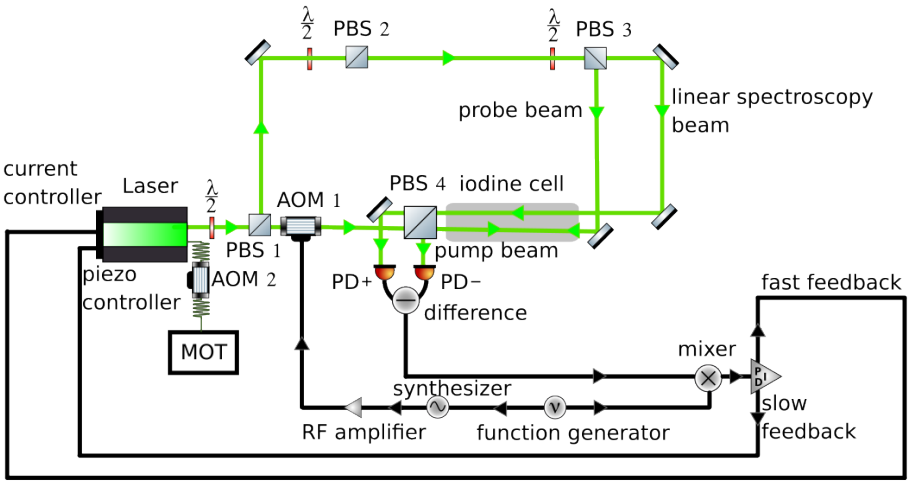

FIGURE 4.1: Representation of the laser frequency stabilization system used for laser cooling of ^{174}Yb in the $^1S_0 - {}^3P_1$ transition. The laser has two outputs (see text). One is a free-space output that is used for laser frequency stabilization, while the fibered is sent to AOM 2 to be split into the six MOT beams by a fibered splitter. The free space beam is split by PBS 1. The transmission, diffracted and modulated by AOM 1, is also transmitted by PBS 4 and is the pump beam in a modulation transfer spectroscopy (MTS) scheme. The reflection of PBS 1 passes through $\frac{\lambda}{2}$ and PBS 2 that are used to control its total power. The beam is further split by a $\frac{\lambda}{2}$ and PBS 3, the transmission is used for linear spectroscopy of $^{127}I_2$ before being transmitted by PBS 4 and detected by PD+. The reflection, counterpropagating to the pump beam, is the probe beam of the MTS and is detected by PD- after being reflected from PBS 4. AOM 1 is driven by a sinusoidal signal of frequency 80 MHz generated by a synthesizer and frequency modulated by a sinusoidal signal of frequency 200 kHz generated by a function generator. The output of the function generator is also sent to a mixer to demodulate the difference between the signals measured by PD+ and PD-. The error signal generated by the demodulation is sent to a PID controller that has a slow and a fast feedback output. The slow output is used to control a piezo actuator that controls the laser grating, while the fast output is connected to the diode controller. **Source: [85].**

4.1.2 Spectroscopy of the R(158)25-0 line

Fig. 4.2 shows the saturated absorption spectroscopy (in blue) and the MTS signal (in red) of the P(49)24-1 and R(158)25-0 $^{127}I_2$ lines for a laser frequency scan rate of 147 MHz s^{-1}. From -1500 MHz to -400 MHz the twenty-one hyperfine components of the P(49)24-1 rotational line can be seen. From about -400 MHz to 300 MHz fourteen out of the fifteen hyperfine components of the R(158)25-0 line can be seen. The data shown in fig. 4.2 was taken with a pump beam power of 300 mW and a MTS probe beam power of 1 mW in the position of the iodine cell.

Absolute frequency measurements of the hyperfine components of the P(49)24-1 line were recently reported [84] with an uncertainty of 7 kHz. Additionally, frequency shifts due to laser power (-2.6 kHz mW^{-1}) and iodine pressure (-1.8 kHz Pa^{-1}) were reported. These results were used to calibrate the laser frequency scan shown

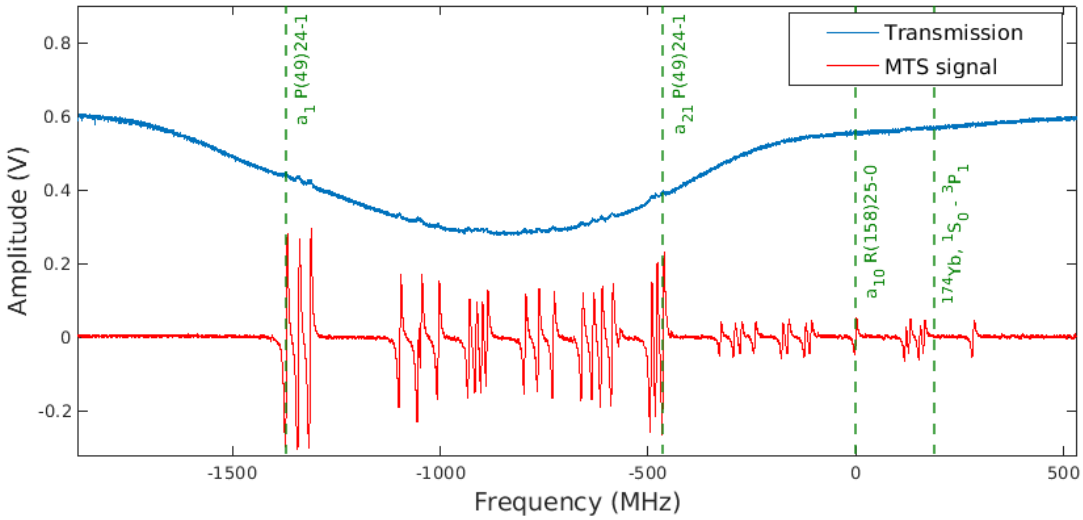

FIGURE 4.2: Saturated absorption spectroscopy (in blue) and modulation transfer spectroscopy (in red) of the P(49)24-1 and R(158)25-0 $^{127}I_2$ lines. The strong lines between -1500 MHz and -400 MHz are the hyperfine transitions of the P(49)24-1 line. Between -400 MHz and 300 MHz it is shown 14 of the 15 hyperfine components of the R(158)25-0 line. The origin of the horizontal axis is on the center of the a_{10} component of the R(158)25-0 transition. The green dashed lines indicate (from left to right) the a_1 and a_{21} hyperfine components of the P(49)24-1 line, the a_{10} hyperfine component of the R(158)25-0 line, and the ^{174}Yb $^1S_0 - {}^3P_1$ intercombination transition. **Source: [85].**

in fig. 4.2. The green dashed lines in fig. 4.2 correspond to (from left to right): the a_1 hyperfine component of the P(49)24-1 line, the a_{21} hyperfine component of the P(49)24-1 line, the a_{10} hyperfine component of the P(49)24-1 line and the frequency shift that corresponds to the ^{174}Yb $^1S_0 - {}^3P_1$ intercombination transition (accordingly to [86]).

The laser frequency scan shown in fig. 4.2 was performed by scanning the piezo actuator that controls the laser grating by a triangular function. The dependence of the laser frequency with respect to the piezo voltage is not linear and also suffers from fluctuations of the other parameters (diode's current and diode's temperature). To obtain a relatively linear scan we used the wavelength meter PID to control the laser piezo actuator. The wavelength meter continuously measure the laser frequency while performing the frequency scan, this allows a correction of the nonlinearity of the laser frequency scan with respect to the piezo voltage and also corrects drifts due to fluctuations of the laser diode current and temperature. Finally, we can rely on the absolute frequency of the a_{21} hyperfine component of the P(49)24-1 line ($\nu_{a21} = 539\,385\,938\,687(7)$ kHz) and the frequency shift between it and the a_1 hyperfine component of the same line ($\Delta\nu = 906.77(1)$ MHz) to estimate the absolute frequencies of the hyperfine components of the R(158)25-0 line.

The measured frequencies of the hyperfine components of the R(158)25-0 line are shown in table 4.1, alongside their shifts with respect to a_1 hyperfine component of

Absolute frequencies of the R(158)25-0 line		
line	Frequency (MHz)	Shift (MHz)
a_1	539385831(6)	+799(6)
a_2	539386076(6)	+1044(6)
a_3	539386111(6)	+1079(6)
a_4	539386128(6)	+1096(6)
a_5	539386161(6)	+1129(6)
a_6	539386228(6)	+1196(6)
a_7	539386242(6)	+1210(6)
a_8	539386282(6)	+1250(6)
a_9	539386297(6)	+1265(6)
a_{10}	539386406(6)	+1374(6)
a_{11}	539386527(6)	+1495(6)
a_{12}	539386539(6)	+1507(6)
a_{13}	539386562(6)	+1530(6)
a_{14}	539386573(6)	+1541(6)
a_{15}	539386694(6)	+1662(6)

TABLE 4.1: Absolute frequencies of the hyperfine components of the R(158)25-0 $^{127}I_2$ line. The third column represents the shift with respect to the a_1 hyperfine component of the P(49)24-1 line.

the P(49)24-1 line. Despite the relatively large uncertainty (6 MHz), they correspond to the first frequency measurements of such lines and can be useful to determine which line to be used as frequency reference for a given application. The frequency scan rate for these measurements was 100 MHz s^{-1}. The correction of the scan due to the feedback of the wavelength meter PID was performed at each 4 MHz of frequency scan, and it is the main source of uncertainty. Measurements with lower uncertainty could be performed by decreasing the frequency scan rate.

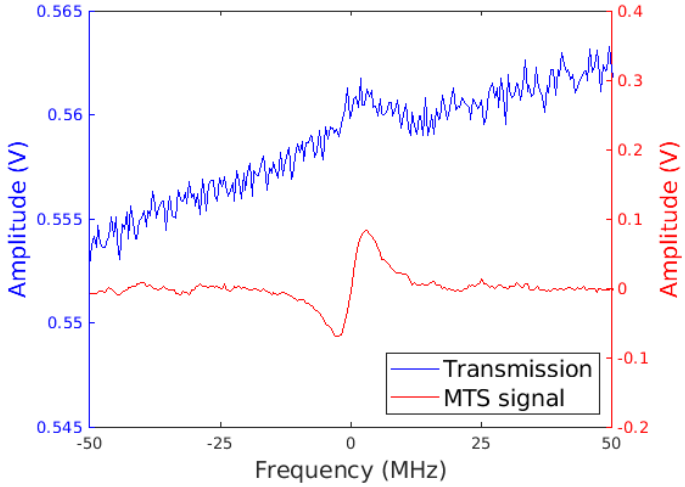

FIGURE 4.3: Saturated absorption spectroscopy (in blue) and MTS (in red) of the a_{10} hyperfine component of the R(158)25-0 line for a laser frequency scan rate of 6.65 GHz s^{-1}. The saturated absorption data is an average of 100 samples, while the MTS signal is not averaged. **Source: [85].**

The line chosen for the laser frequency stabilization was the a_{10} component of the R(158)25-0 line. As can be seen in fig. 4.2, the amplitude of the R(158)25-0 hyperfine components are smaller than the P(49)24-1 ones. Thus, to stabilize the laser frequency to one of the weak lines can be demanding. This is probably the main reason why such lines were not yet used as frequency references for laser cooling of ^{174}Yb atoms. To illustrate, fig. 4.3 shows the saturated absorption spectroscopy signal (in blue) and the MTS signal (in red) of the a_{10} component of the R(158)25-0 line. The saturated absorption signal shown is an average of 100 samples, while the MTS signal is a single-shot signal. The relative amplitude of the line, defined here as the amplitude of the peak with respect to the background divided by the background amplitude, is smaller than 1%. This small relative amplitude of such line motivated the use of balanced detection in addition to MTS. For instance, balanced detection is usually performed in combination with frequency modulation spectroscopy to generate a background free error signal. But, as MTS already provides an error signal without Doppler background (see chapter 2) the use of balanced detection in our experiment is only justified by the small amplitude of the signal. A similar experimental scheme was already used in [87], where a better laser frequency stability was achieved with balanced detection and MTS, rather than with MTS only. The choice of MTS in opposition to frequency modulation spectroscopy, is also justified by the stronger dependence of the latter with respect to fluctuations of temperature.

The MTS error signal, shown in fig. 4.3, is the one used for the laser frequency stabilization in this work. It is important to mention that vertical drifts of the error signal were observed and that we attribute this effect to temperature fluctuations in the experimental room. Indeed, such fluctuations are stronger once the elements that compose the feedback loop are turned on (when they are warming up) and we have identified the RF mixer as the main source of such drifts. Since the room temperature typically fluctuates more than 1 °C, we have inserted the RF mixer in a homemade peltier module to stabilize its temperature. Such vertical drifts are now less important and the experiment can be operated by, at least, one full day before that the drift corresponds to a laser frequency drift of the order of the ^{174}Yb $^1S_0 - {}^3P_1$ transition linewidth. It is equally important to emphasize that a 10 cm vapour cell was used during this work, which shows that this experimental configuration can be used in compact systems. However, the use of a longer iodine cell would result in an error signal with higher peak-to-valley amplitude and consequently a better laser frequency stability (that will be analyzed in the next section) could be achieved.

4.1.3 Error signal dependence

The list below points out some of the solutions to problems that can be observed in an experimental scheme as the one shown in fig. 4.1 for frequency stabilization to a relatively weak signal.

- The power balance between the two probe beams should be carefully adjusted by the waveplate that is situated between PBS 2 and PBS 3. Power imbalance increases the noise in balanced detectors. Therefore, a fine adjustement of the waveplate should be possible and such adjustments are made in a weekly basis due to mechanical drifts of its mounts. The noise introduced by small rotations of the waveplate (less than 0.1° are noticeable in the error signal).

- The polarization of the beams should be stable, due to the item mentioned above. Indeed, relevant fluctuations of the laser polarization would either cause a power imbalance between the two probe beams or cause fluctuations of the total power.

- The alignment of the pump beam should be done carefully to avoid its reflection by an element (iodine cell, PBS 4) into one of the photodiodes. In our scheme the cell was slightly tilted to avoid that the reflection of the pump beam on one of the cell's surface is sent to PD-.

- The probe beam should be collinear to the carrier of the pump beam. In fact, after passing through AOM 1 the laser beam is diffracted into several other beams, since wideband modulation (modulation index is higher than 1) of the AOM driver frequency is performed. Each diffraction order propagates with a small angle with respect to the next order. Then if the laser beams propagate through large distances it would be possible to geometrically distinguish each of the diffracted orders (see [88]). In our scheme the distance between AOM 2 and the vapour cell is small so that the carrier and the sidebands of the pump are nearly superposed inside the cell. However, if the probe beam is not collinear to the carrier beam it means that it will interact more with one class of the sidebands (positive or negative) than the other. This cause an imbalance of the error signal, making the vertical absolute amplitude of the peak with respect to the signal background different from the absolute amplitude of the valley.

- Although a careful measurement of the error signal amplitude with respect to the modulation index was not performed, it was verified that the amplitude of the error signal was considerably smaller in the narrowband frequency modulation regime (when the modulation index is smaller than 1). Therefore, the electronic devices should be chosen in order to allow the tuning of the modulation index (and modulation frequency) to facilitate the optimization of the error signal.

Most of the data shown in this thesis was obtained with a pump beam power of 300 mW, which did not imply any issue to us due to the high output power of our laser system (1.3 W). However, to show that this laser frequency stabilization scheme can be performed even if low laser power is available we have characterized the error signal for different pump beam powers (ranging from 20 mW to 300 mW).

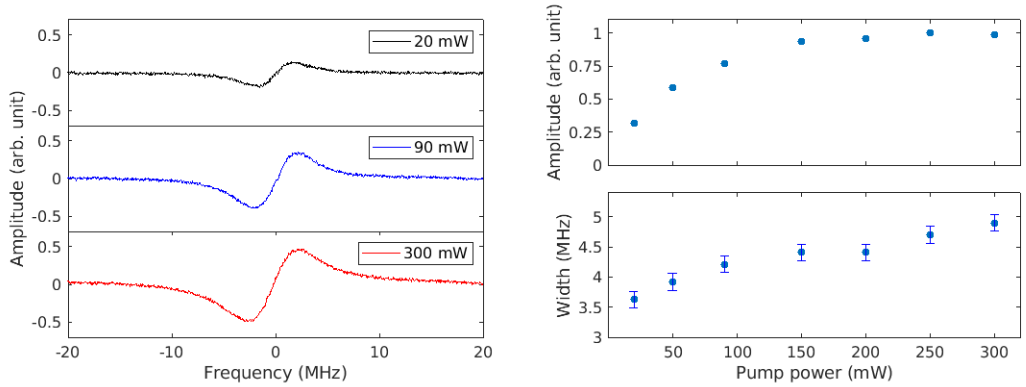

(A) (B)

FIGURE 4.4: (a) Error signal for three different values of pump beam power. (b) Amplitude and width of the error signal for different values of pump beam power. The error bars of the widths represent the uncertainty due to the resolution of the measurement, while the error bars of the amplitudes are smaller than the dots that represent the data. **Source: [85].**

In fig. 4.4a one can see the error signal for three different pump powers (20, 90 and 300 mW), the amplitude scale is arbitrary but it is the same for the three curves. The amplitude (peak-to-valley amplitude) and width of the error signals with respect to the pump beam power are shown in fig. 4.4b. The amplitude of the error signal increases until an apparent saturation, while the width also increases. The minimum measured error signal slope, defined here as the signal amplitude divided by its width, corresponds to 44% of the maximum one. This result is a good indication that robust laser frequency stabilization can also be achieved if only moderate laser power is available. In fig. 4.4b, the error bars of the amplitudes are smaller than the dots that represent the data, while the ones for the width are defined by the resolution of the measurement. In iodine spectroscopy it is typical to cool down the cold finger of the vapour cell to obtain a narrower signal [89], but the amplitude of the signal is also reduced.

4.2 Results on laser frequency stabilization by modulation transfer spectroscopy and balanced detection

After introducing the frequency reference and the characterization of the error signal, an evaluation of the laser after the stabilization will be performed. Such evaluation will be done by either analyzing the noise power spectral density (NPSD) or the Allan deviation of the laser fractional frequency. In the absence of an out-of-loop frequency discriminator (e.g. an ultrastable Fabry-Pérot cavity), we use the error signal itself to convert its amplitude fluctuations to laser frequency fluctuations (or noise). A typical slope of the discriminator used here is $0.5\,\mathrm{MHz\,mV^{-1}}$, and it corresponds to the slope of the error signal measured just after the RF mixer, i.e. before the FALC (PID). Therefore, for convenience, the measurements were performed in the output of the FALC but the gain function that characterizes the amplification

applied by the FALC to each of the spectral components of the error signal was measured to perform the conversion of the signal after the FALC to the signal before it.

In this section it will be discussed the algorithm used to obtain either NPSD or Allan deviation data. A critical analysis of the results and their implications to the experiment will be performed, alongside a discussion about the limitations of the measurements.

4.2.1 Noise power spectral density

The frequency noise power spectral density (FNPSD) is a powerful tool to describe the noise (laser frequency fluctuations). Indeed, provided that the FNPSD was measured, one can determine which are the kind of noises that are predominant in a given frequency range [91]. One can also calculate the Allan deviation of the laser fractional frequency [91] and the laser lineshape (and linewidth) [92, 93] from the FNPSD.

To measure the laser FNPSD in our system we follow the steps below:

- First, the gain curve that describes the amplification applied by the FALC to the error signal is measured. To do it, we apply a sinusoidal signal of a given frequency and amplitude to the input of the FALC and measure the amplitude of the output signal. We repeat the process by manually tuning the frequency of the signal and recording the respective output. We calculate the power of the signal (in dBm units) and finally obtain the gain (in dB units) by simply subtracting the input power from the output power. Fig. 4.5 shows a typical gain curve. In practice, the gain was measured for frequencies from 1 to 250 kHz in steps of 1 kHz.

- The error signal is recorded by a digital oscilloscope (Lecroy HDO4010A-D), which has an internal function that directly calculates the power spectrum of the signal. In other words, it calculates the square of the fast Fourier transform (FFT) of the signal's amplitude fluctuations ($FFT(\Delta A)^2$) in dBm units.

- The gain applied to the error signal by the FALC is subtracted from $FFT(\Delta A)^2$ and the remaining set of values is converted to (V^2) units.

- When the laser is frequency stabilized, fluctuations of the amplitude of the residual error signal (ΔA) can be converted to laser frequency fluctuations ($\Delta\nu$) by using the slope of the error signal (δS) as a conversion factor ($\Delta\nu = \frac{\Delta A}{\delta S}$). Therefore, $FFT(\Delta\nu)^2$ is obtained.

- Finally, the frequency noise power spectral density (FNPSD) is given by [91] $\frac{FFT(\Delta\nu)^2}{BW}$, where BW is the measurement bandwidth.

- To obtain the FNPSD for the free-running laser (when it is not stabilized), we manually tune its frequency to be on-resonance to the relevant iodine transition. Then, we record $FFT(\Delta A)^2$ before that the laser is driven out-of-resonance. Finally, we can perform the steps above mentioned.

The FALC gain function shown in fig. 4.5 is the result of the effect of its five circuits (unlimited integrator, slow integrator, extra slow integrator, fast differentiator and fast integrator). The gain applied by each circuit for a given frequency is determined by a set of switches that can be manually adjusted. The switches for the extra slow integrator are enumerated from 1 to 6, the switches for the slow integrator, fast differentiator and fast integrator are enumerated from 1 to 10. The higher the number of the switch that is turned on, the higher the frequency at which the maximum gain is applied to the signal. In other words, in order to apply a gain to the highest possible frquency, the switch number 10 should be switched on; if one needs to apply a maximum gain to the lowest possible frequency one turns on the switch number 1. Fig. 4.5 corresponds to a gain obtained when the following switches were on: extra slow integrator (none), slow integrator (none), fast differentiatior (switch 1), and fast integrator (switch 1). The obtained gain curve is maximum for lower frequencies and it decreases monotonically for higher frequency ranges, which is reasonable since we do not expect to suppress high frequency noise (higher than 200 kHz).

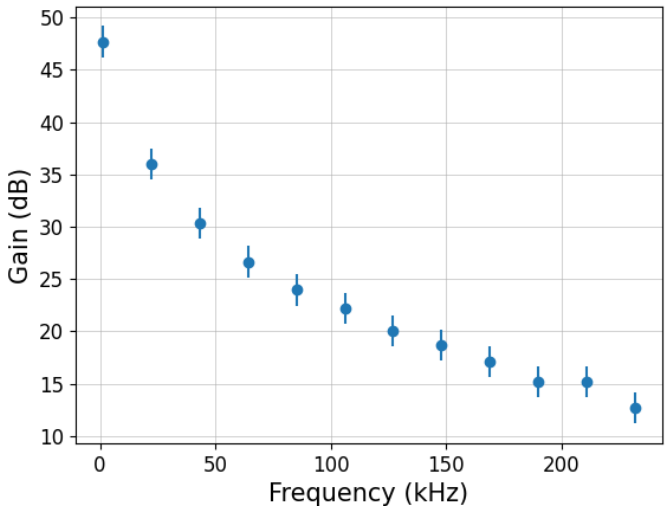

FIGURE 4.5: Typical gain applied by the Fast Analog Linewidth Control (FALC 110) to the error signal for a few frequencies (from 1 to 250 kHz).

Fig. 4.6 shows the NPSD of the laser when stabilized (in blue) and when free-running (in red) for Fourier frequencies up to 250 kHz. As the RF driver signal was frequency modulated by a sinudoidal signal of 200 kHz, we do not expect the feedback loop to suppress noise above this frequency (which was verified), this justifies the frequency upper limit. One can see that the NPSD of the stabilized laser is below

the level of the free-running one until a Fourier frequency of about 30 kHz. This decrease of the NPSD indicates that the feedback loop is effective, i.e. it reduces noise in a range of Fourier frequencies.

The NPSD curve of the free-running laser shown in fig. 4.6 has the behaviour of typical diode lasers FNPSD. The $\frac{1}{f}$ (flicker noise) for low Fourier frequencies (until about 300 Hz) is typical of diode lasers (and oscillators in general) [91, 94]. For higher Fourier frequencies, i.e. above 300 Hz, white noise is observed (characterized by a flat FNPSD). A white noise portion of a diode laser FNPSD is also expected for higher frequencies [91, 94], as shown by fig. 4.6. However, the FNPSD of the free-running laser measured by us is higher than the one measured by the laser's manufacturer [95].

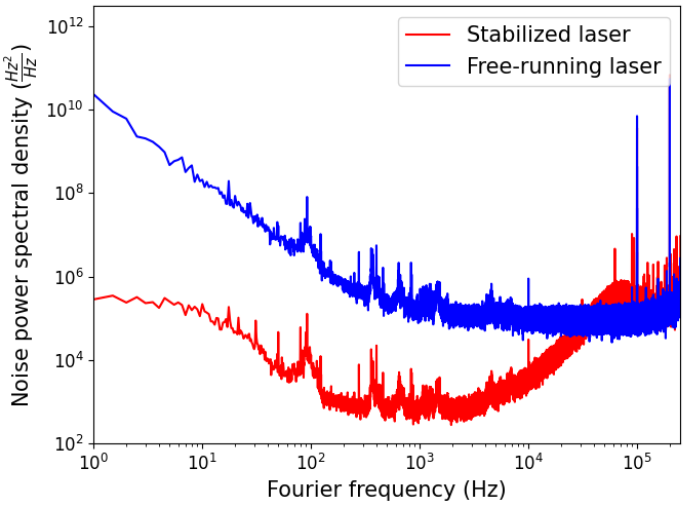

FIGURE 4.6: Laser noise power spectral density for the free-running (in blue) and stabilized (in red) cases. The data is an average of 20 samples. **Source: [85].**

The relative intensity noise (RIN) of a laser [96–98] characterizes the frequency dependence of its intensity noise. RIN measurements of the laser system used by us were previously published by the manufacturer [99]. It was shown that the RIN of the laser beam after the SHG cavity is two orders of magnitude larger than the RIN of the beam just after the diode laser. We therefore, attribute the plateau for the free-running laser FNPSD (Fourier frequencies above 300 Hz) to laser amplitude fluctuations.

In summary, due to the weakness of the frequency discriminator we cannot completely distinguish laser frequency noise from laser amplitude noise. To avoid such issue, another frequency discriminator (with a larger slope) could be used, such as a high finesse cavity. Due to this issue, we cannot apply the well know β-line method [92, 93] to extract the laser linewidth from fig. 4.6. However, the noise suppression that is shown is an indication that the laser linewidth of the free-running laser ($\approx$ 100 kHz, accordingly to the manufacturer) is further reduced by the stabilization method.

4.2.2 Allan deviation

The Allan deviation of the laser's fractional frequency measure its frequency instability in time domain [100], differently from the FNPSD described above that is a measurement performed in the frequency domain. The Allan deviation is the square root of the Allan variance, also known as two-sample variance, and it gives the information of the root mean square (RMS) value of the instability in frequency between two observations delayed by a given amount of time.

The Allan deviation is defined as [101]

$$\sigma_y(\tau) = \sqrt{\langle \frac{1}{2}(\bar{y}_{n+1} - \bar{y}_n)\rangle}, \tag{4.1}$$

where $\langle ... \rangle$ denotes the expectation value and $\bar{y}_n$ the fractional frequency average over the averaging time τ. The fractional frequency is the difference between the oscillator frequency ($\nu(t)$) and the reference frequency (ν_0) normalized by the reference frequency ($y_n = \frac{\nu(t)-\nu_0}{\nu_0}$).

A significant improve of the treatment of Allan deviation data was achieved when the use of all possible overlapping data samples at each averaging times was done. The overlapping Allan deviation is calculated for a set of M measurements for averaging times $\tau = m\tau_0$ (m is the averaging factor and τ_0 the measurement frequency interval), by the following formula [102]

$$\sigma_y(\tau) = \sqrt{\frac{1}{2m^2(M-2m+1)}\frac{1}{2}\sum_{j=1}^{M-2m+1}\left\{\sum_{n=j}^{j+m-1}(y_{n+m} - y_n)\right\}^2}. \tag{4.2}$$

Now we turn to discuss Allan deviation measurements and the treatment of such measurements:

- The residual error signal is recorded by a digital oscilloscope. Special attention should be paid to prevent the phenomenon of aliasing. In other words, the time between two data samples (τ) defines the sampling rate as $\frac{1}{\tau}$ samples/s, and the measurement cutoff frequency (Nyquist frequency) is $\nu_c = \frac{1}{2\tau}$. This is what is stated by the Nyquist-Shannon theorem [103] "*If a function f(t) contains no frequencies higher than X* Hz*, it is completely determined by giving its ordinates at a series of points spaced 1/2X seconds apart.* ". Therefore, the sampling rate should be chosen so that the respective Nyquist frequency is higher than the maximum frequency component (which is the inverse of the minimum averaging time) that one wants to measure.

- The gain curve of the FALC is used to convert the FALC's output signal to the input one.

- The error signal slope is used to convert the residual error signal fluctuations into fractional frequency fluctuations.

- A python library (*AllanTools*) is used to calculate the overlapping Allan deviation (by eq. (4.2)).

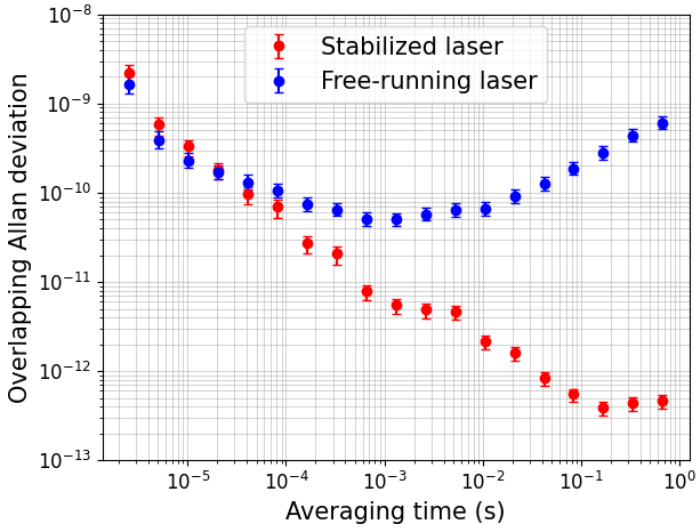

FIGURE 4.7: Overlapping Allan deviations of the laser fractional frequencies when free-running (in blue) and stabilized (in red). The error bars are determined by the uncertainty in the measurement of the FALC gain curve. The effectiveness of the frequency stabilization loop is shown by the decrease of the Allan deviation for the stabilized laser for averaging times higher than 20 µs. **Source: [85].**

The overlapping Allan deviation was measured for averaging times from 2.5 µs to 6 s. The overlapping Allan deviation of the free-running laser is shown in blue. It can be seen that the laser frequency instability decreases from 2.5 µs to 1 ms, and then it increases again for the whole range of averaging times that it was measured. For the stabilized laser it decreases until 0.17 s, at which its value is 3.9×10^{-13}, which corresponds to a frequency instability of 210 Hz. The range of averaging times was chosen to comprise the time window of typical cold atom experimental cycles (of the order of 1 s). The measuremement shown in fig. 4.7 was obtained with slightly different set of parameters with respect to the one used for the measurement of the FNPSD. The switch 1 of the slow integrator was turned on for the Allan deviation measurements.

It is important to emphasize that fig. 4.7 is also affected by laser amplitude noise for averaging times below 3 ms, as discussed for the FNPSD. However, the decrease of the laser frequency instability when the laser is stabilized and the relatively low values obtained (as low as 3.9×10^{-13}) are also a good indication that the feedback loop is effective and that the stabilized laser is suitable to perform laser cooling and trapping of ^{174}Yb atoms in the $^1S_0 - {}^3P_1$ transition, as will be shown in the next section.

4.3 MOT

In this chapter we have introduced and characterized an iodine line that is convenient to be used as a frequency reference for laser cooling of ^{174}Yb (the most abundant isotope). An experimental scheme allowing to perform robust frequency stabilization of such a line despite its relative weakness was described, and the noise properties (and frequency instability) was studied in the frequency domain by means of the frequency noise power spectral density and in time domain by overlapping Allan deviation of the laser fractional frequencies. It was concluded that the frequency stabilization achieved should allow us to use this laser system to load an ^{174}Yb MOT. Indeed, this section will be dedicated to the transfer of the atoms from the blue to the green MOT.

4.3.1 Capture range

The number of atoms that are transferred from the blue to the green MOT depends on how many atoms can be cooled down by the green MOT beams before escaping the zone at which they interact with the beams. Then, the number of atoms that are trapped in a green MOT, when this one is charged from a preloaded blue MOT, depends on the mean radiation pressure force applied by the MOT beams to the atoms (eq. (3.1)), the initial velocity distribution of the atoms (defined by the velocity distribution of the atoms trapped on the blue MOT) and the size of the MOT beams.

The number of atoms trapped on the green MOT will then depend on the maximum velocity that an atom can have and still be trapped by the MOT (capture velocity). We can qualitatively estimate the dependence of the number of trapped atoms by inspecting eq. (3.1) in the presence of the MOT magnetic field gradient. From now on, we will denote I_{tot} as the sum of the intensities of the six MOT beams. For large laser beam intensities ($I_{tot} >> I_{sat}$), as discussed in chapter 3, the force is independent of the laser beam intensity while for low beam intensities ($I_{tot} < I_{sat}$) it increases by increasing the intensity. Then, the capture velocity should increase as the total laser beam intensity is increased, until a maximum value at which it is kept constant. By eq. (3.1), we see that the force is maximized when $\Delta \pm kv \pm \gamma_J \nabla B_z z$ is zero. Therefore, it is expected that the capture velocity of the green MOT has a maximum for a given laser detuning. We have performed experiments to conclude the optimal experimental parameters, as will be discussed below.

4.3.2 MOT transfer to the $^1S_0 - {}^3P_1$ transition

The trapping of up to 1×10^9 atoms in the ^{174} $^1S_0 - {}^1P_1$ transition was discussed in chapter 3, now we turn our attention to transfer the maximum amount of atoms from the blue to the green MOT. To study the efficiency of the transfer we perform the experiment in steps that are depicted in fig. 4.8 and summarized as follows

- **Loading of the blue MOT.** The blue MOT is loaded for a time $t_b = 1\,\mathrm{s}$ using 72 mW of total MOT beams power, 22 mm of beam waist, $-2\Gamma_b$ of laser detuning and $20\,\mathrm{G\,cm^{-1}}$ of axial magnetic field gradient. The slowing beam is simultaneously turned on with a power of 200 mW and detuned by $-9.6\Gamma_b$.
- **Transfer to the green MOT.** After t_b, the blue MOT beams and slowing beam are turned off. Simultaneously, the green MOT beams (of waist 9 mm) are turned on and the magnetic field gradient is decreased.
- **Loading of the green MOT.** The green MOT beams remain on for a time $t_g = 40\,\mathrm{ms}$ an then are turned off alongside the magnetic field gradient.
- **Time of flight.** The atomic cloud expands freely for a time of flight (TOF) of 15 ms.
- **Absorption imaging.** Finally, we turn on a probe beam to perform absorption imaging of the atomic cloud on the $^1S_0 - {}^1P_1$ transition. The blue probe is resonant with the $^1S_0 - {}^1P_1$ transition and its intensity is weak (i.e. $I_{tot} << I_{sat}$).

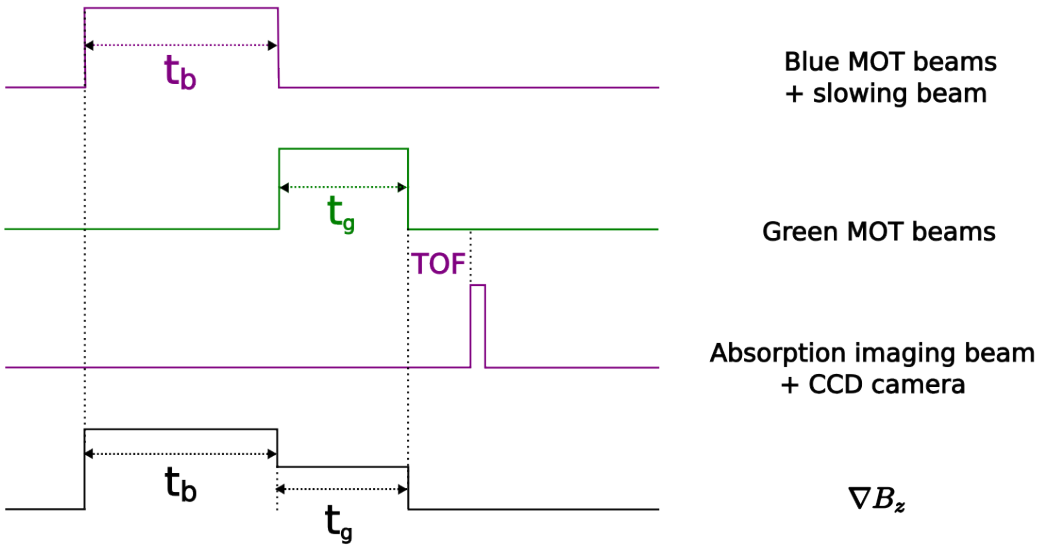

FIGURE 4.8: Experimental temporal sequence for absorption image of the atomic cloud. The sequence shows that the blue MOT beams and slowing beam (on top) are turned on for a time t_b. Simultaneously, the magnetic field gradient (∇B_z) is turned on. After t_b, the blue MOT beams and slowing beam are turned off, the intensity of ∇B_z is decreased and the green MOT beams are turned on. The green MOT is loaded for a time t_g, and then the laser beams are turned off. Finally, the atomic cloud expands for a time (TOF) until that the absorption image is taken by the absorption imaging beam and a CCD camera.

To analyze data taken from absorption images we use the Beer-Lambert law that relates the intensity of the light that is incident to the cloud (I_{in}) to the light transmitted by the cloud (I_{out})

$$I_{out} = I_{in} e^{-b(\Delta)}. \tag{4.3}$$

$b(\Delta)$ is the optical depth. If we consider that the beam propagates along the x axis, it is given by

$$b(\Delta) = \sigma(\Delta) \int_{-\infty}^{\infty} n(x,y,z)dx. \tag{4.4}$$

$\sigma(\Delta)$ is the optical cross-section, which can be written as a function of the resonant cross-section (σ_0)) as

$$\sigma(\Delta) = \frac{\sigma_0}{1 + 4\frac{\Delta^2}{\Gamma^2}}. \tag{4.5}$$

The resonant cross-section is given by [104]

$$\sigma_0 = \frac{3\lambda^2}{2\pi}. \tag{4.6}$$

We assume a Gaussian density profile of the atomic cloud with its root-mean-square sizes along the three different directions on a Cartesian coordinate system denoted by (R_x, R_y, R_z), i.e.

$$n(x,y,z) = n_0 e^{-\frac{x^2}{2R_x^2} - \frac{y^2}{2R_y^2} - \frac{z^2}{2R_z^2}}. \tag{4.7}$$

We can now, write the Beer-Lambert law by using eqs. (4.3) to (4.7) as

$$I_{out} = I_{in} e^{-\sigma_0 n_0 \int_{-\infty}^{\infty} e^{-\frac{x^2}{2R_x^2} - \frac{y^2}{2R_y^2} - \frac{z^2}{2R_z^2}} dx}. \tag{4.8}$$

Defining the on-resonance optical depth as

$$b_0 = \sigma_0 n_0 \sqrt{2\pi} R_x, \tag{4.9}$$

we derive from eq. (4.8)

$$I_{out} = I_{in} e^{b_0 e^{-\frac{x^2}{2R_z^2} - \frac{y^2}{2R_y^2}}}. \tag{4.10}$$

Eq. (4.10) describes the two-dimensional profile of the atomic cloud. Therefore, we use it to numerically fit the absorption images of the cloud, in fact we fit the ratio between the absorption image and the input beam (i.e. $\frac{I_{out}}{I_{in}}$). An illustration of a typical fit of the absorption image for a given set of parameters is shown in fig. 4.9. From the fit we retrieve b_0, R_y and R_z. Besides b_0, we are interesting in the number of atoms and the density of the atomic cloud. The number of atoms (N_{at}) can be retrieved from eq. (4.7), as below

$$\begin{aligned} N_{at} &= \int_{-\infty}^{\infty}\int_{-\infty}^{\infty}\int_{-\infty}^{\infty} n_0 e^{-\frac{x^2}{2R_x^2} - \frac{y^2}{2R_y^2} - \frac{z^2}{2R_z^2}} dxdydz, \\ &= \sqrt{8\pi^3} R_x R_y R_z n_0. \end{aligned} \tag{4.11}$$

From eqs. (4.6), (4.9) and (4.11) we can express b_0 as

$$b_0 = \frac{3\lambda^2}{(2\pi)^2} \frac{N_{at}}{R_x R_y}. \tag{4.12}$$

Therefore, by absorption imaging technique one can retrieve b_0 and N_{at}. For instance, to measure the number of atoms in an atomic cloud with $b_0 > 1$ (multiple scattering regime) this technique is more suitable than by measuring the fluorescence of the cloud, that we performed for the blue MOT. In the single scattering regime ($b_0 << 1$) the fluorescence of the MOT is proportional to the number of trapped atoms, which is not true in the multiple scattering regime. In this work we are able to retrieve the atomic density (n_0) by assuming that the dimensions of the cloud on a plane parallel to the optical table are the same, i.e. $R_x = R_y$. This is a reasonable assumption because the parameters of the MOT (beam intensities and magnetic field gradient) are the same for these two dimensions.

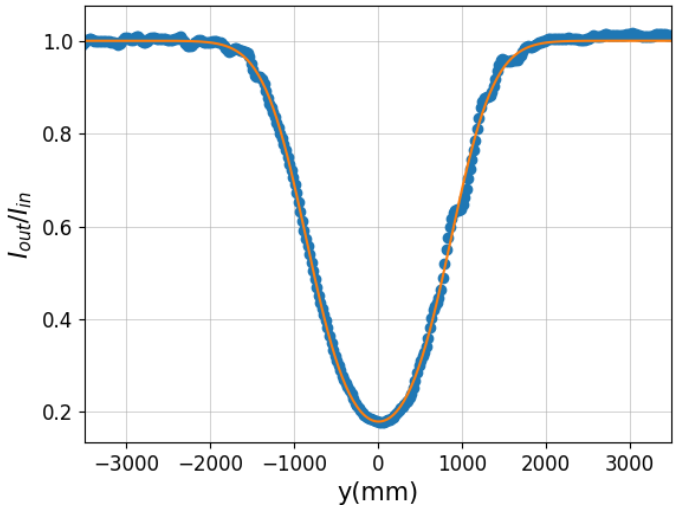

FIGURE 4.9: Typical absorption image of the atomic cloud along the horizontal (y) axis (in blue) alongside a fit (in orange) of it by eq. (4.10). The image was taken after a TOF of 15 ms and the following parameters were used: $\Delta = -4\Gamma$, $I_{tot} = 4I_{sat}$ and $\nabla B_z = 4\,\mathrm{G\,cm^{-1}}$.

To measure the number of atoms transferred from the blue to the green MOT we perform absorption imaging technique (as shown in fig. 4.8) for different values of a given parameter ($\frac{I_{tot}}{I_{sat}}$,∇B_z and laser beam detuning) while the other parameters are kept constant. The result of the optimization of the MOT beam intensity is shown in fig. 4.10 for a green MOT beams detuning of $-6\Gamma_g$ and $\nabla B_z = 4\,\mathrm{G\,cm^{-1}}$. For low intensities the number of atoms increase until $I_{tot} = 10I_{sat}$ and then it remains constant at higher intensities (within the measurement uncertainties) as expected. The error bars are retrieved from the uncertainty due to the fit of the data by eq. (4.10) and the uncertainty of the number of atoms trapped on the blue MOT. The uncertainty of the number of atoms trapped on the blue MOT is estimated by fluctuations of the spectroscopic signal shown in fig. 3.10 for a large number of trapped atoms. Such fluctuations are due to the competition between the forces applied to the atoms by the MOT, which are confining, and the repulsive interactions due to multiple scattering of light inside the atomic cloud [51, 105–107].

Fig. 4.11 shows the number of atoms transferred to the green MOT with respect

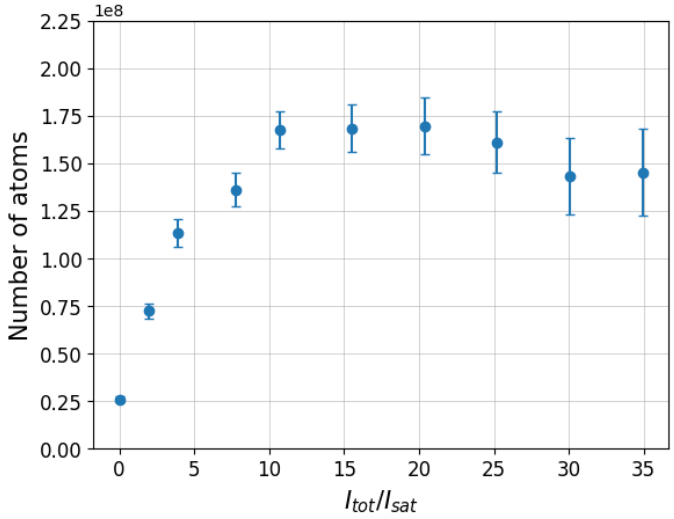

FIGURE 4.10: Number of atoms transferred to the green MOT, measured by absorption image, versus total MOT beam intensity (divided by I_{sat}) for $\Delta = -6\Gamma$ and $\nabla B_z = 4\,\mathrm{G\,cm^{-1}}$. The number of atoms increases by increasing the laser beam intensities for $I_{tot} < I_{sat}$ until a plateau is reached, as expected from Doppler theory (see text). The error bars are due to the uncertainty of the number of atoms trapped in the blue transition and the uncertainty of the fit performed to the absorption image.

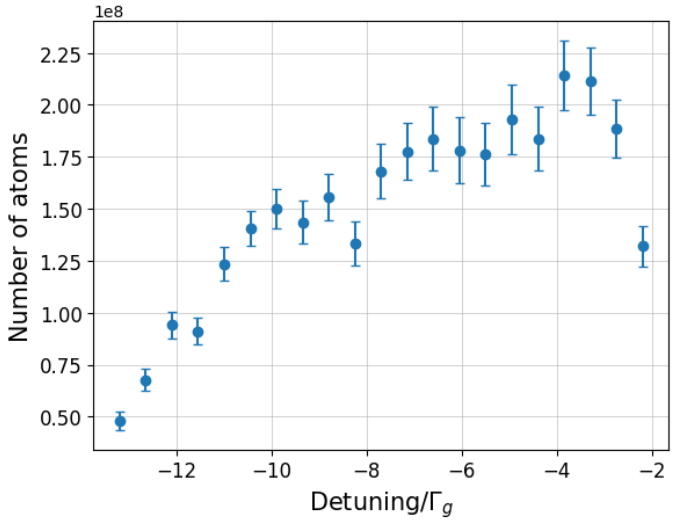

FIGURE 4.11: Number of atoms transferred to the green MOT, measured by absorption image, versus the laser detuning with respect to the $^1S_0 - {}^3P_1$ transition divided by the linewidth of the green transition (Γ_g) for $I_{tot} = 35I_{sat}$ and $\nabla B_z = 4\,\mathrm{G\,cm^{-1}}$. The number of atoms increases by increasing the detuning until a maximum (around $-4\Gamma_g$), then it decreases, which is in agreement to what is expected (see text). The error bars are due to the uncertainty of the number of atoms trapped in the blue transition and the uncertainty of the fit performed to the absorption image.

to the laser detuning for $\nabla B_z = 4\,\mathrm{G\,cm^{-1}}$ and $I_{tot} = 35I_{sat}$. A maximum is obtained for a detuning near -4Δ. The dependence of the number atoms with respect to ∇B_z is shown in fig. 4.12 for $I_{tot} = 35I_{sat}$ and MOT beams detuning of $-6\Gamma_g$. For these measurements we see that the number of atoms that are transferred increase by decreasing the magnetic field gradient. The error bars in figs. 4.11 and 4.12 are also

due to the uncertainty related to the fit of the data by eq. (4.10) and the uncertainty of the number of atoms trapped by the blue MOT.

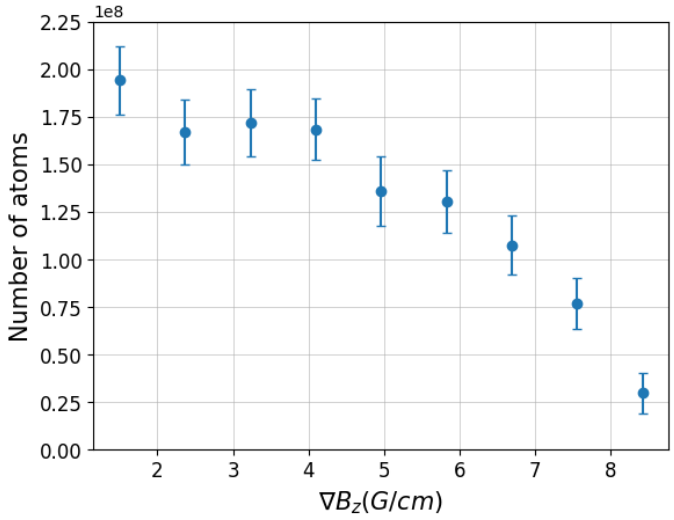

FIGURE 4.12: Number of atoms transferred to the green MOT, measured by absorption image, versus the magnetic field gradient in the axial direction (∇B_z) for $I_{tot} = 35 I_{sat}$ and $\Delta = -6\Gamma$. The number of atoms increases by decreasing the magnetic field gradient (see text). The error bars are due to the uncertainty of the number of atoms trapped in the blue transition and the uncertainty of the fit performed to the absorption image.

4.3.3 Time-of-flight

A set of parameters and a temporal sequence that allows the trapping of 2×10^8 atoms in the $^1S_0 - {}^3P_1$ transition was defined. Now we need to properly characterize the atomic cloud temperature and b_0. Therefore, we perform the so-called *time-of-flight* technique. It consists in performing the experimental temporal sequence defined in fig. 4.8 repeatedly by varying only the time-of-flight (TOF). Absorption images for four different TOFs are shown in fig. 4.13, they show the free fall of the cloud due to the action of the gravitational field and its expansion due to its residual temperature. They were taken for the following set of parameters: $I_{tot} = 35 I_{sat}$, $\nabla B_z = 4\,\mathrm{G\,cm^{-1}}$ MOT beams detuning of $-6\Gamma_g$.

To perform a quantitative analysis, we plot the square of the rms width of the MOT in the y-direction ($\sigma \equiv R_y$) as a function of the square of the TOF (t). The plot is shown in fig. 4.14 alongside a fit of the data (orange line) by the following equation [108, 109]

$$\sigma^2(t) = \frac{k_B T}{m} t^2 + \sigma_0^2. \tag{4.13}$$

The fit allows us to retrieve the temperature of the atomic cloud ($T = 60\,\mu\mathrm{K}$) and the rms width of the cloud in the y-direction at $t = 0$ ($\sigma_0 = 262\,\mu\mathrm{m}$). The number of trapped atoms was 2×10^8 atoms and the retrieved on-resonance optical depth (b_0, calculated by eq. (4.12)) 47 at $t = 0$. The relatively high value of b_0 indicates that our

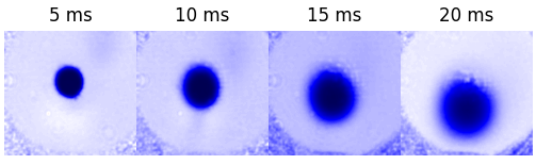

FIGURE 4.13: (a) Absorption images of the atomic cloud for four different times of flight. **Source: [85]**.

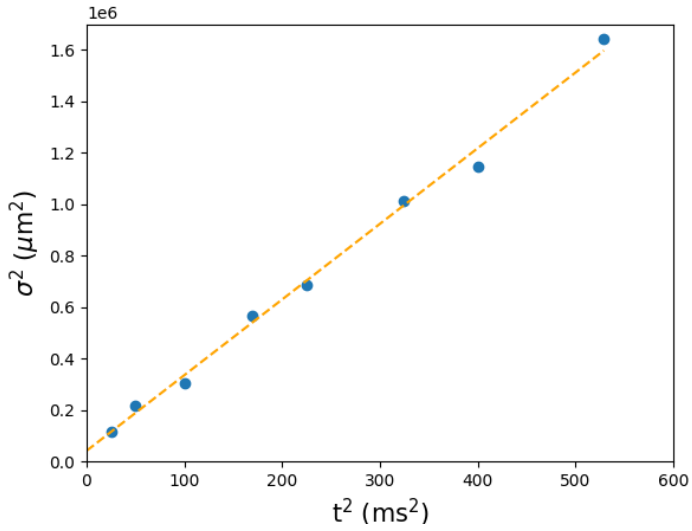

FIGURE 4.14: Square of the rms width of the MOT along the horizontal axis as a function of the square of time of flight (blue dots) and a fit of the data (in orange). The R^2 coefficient of the fit was 0.99. The number of trapped atoms is 2 $\times 10^8$, the horizontal MOT width at t=0 ms is 262 µm. From the fit we can extract an on-resonance optical depth of $b_0 = 47$ and the cloud's temperature value of 60 µK. Error bars are not included because they are smaller than the blue dots that represent the data points. **Source:** [85].

experimental setup is already suitable to perform experiments aiming the observation of collective effects by cold atoms [110, 111]. Additionally, the atomic density, considering $R_x = R_y$, of the cloud for this set of parameters is 4.7×10^{11} atoms cm^{-3} ($\rho\lambda^3 \approx 0.08$).

From eq. (3.3) and the parameters that were used ($I_{tot} = 35 I_{sat}$ and $\Delta = -6\Gamma_g$), the expected cloud's temperature is $T_{th} = 30\,\mu$K. Therefore, the temperature that was measured is twice the value expected from Doppler theory. Such difference can be either due to multiple scattering of light inside the atomic cloud [112] or to

transverse spatial intensity fluctuations of the laser profiles [113]. To obtain a colder and denser cloud an additional experimental step is going to be added. In this step I_{tot} will be decreased and an optimum trade off between the laser detuning and the magnetic field gradient will be searched.

Regardless the green MOT parameters, the number of atoms in the final cloud is limited by the number of atoms trapped in the blue MOT. There are a few solutions that would allow us to increase the number of atoms in the blue MOT. The first one is to optimize the actual setup by cleaning the layer of ytterbium that decreases the efficiency of the slowing beam and by changing the science cell for one with larger windows to allow the use of larger blue MOT beams, which can be done without decreasing the blue MOT beams intensity since we do not use the total output power of the blue laser [51]. The second idea was recently suggested and applied to strontium atoms [114]. It consists in applying a beam resonant to the $^1S_0 - {}^3P_1$ transition during the loading of the blue MOT. Since the decay rate of the $^1S_0 - {}^3P_1$ transition is larger than the one of the $^1S_0 - {}^1P_1$ transition, the population of atoms in the ^{3}P$_1$ state increases and as a consequence the population of atoms in the ground state decreases which weakens loss mechanisms in MOTs. Finally, the design of the MOT beams can be changed to a core-shell geometry [52] which allows an efficient loading of the atoms directly in the green transition.

4.3.4 Absolute frequency of the ^{174}Yb $^1S_0 - {}^3P_1$ intercombination transition

The frequency measurements of the iodine lines shown in table 4.1 together with the MOT operating in the $^1S_0 - {}^3P_1$ transition allow us to address an incongruence between two measurements of the frequency of the ^{174}Yb $^1S_0 - {}^3P_1$ transition. In [115] the authors used the $^5S_{\frac{1}{2}} - {}^5P_{\frac{3}{2}}$ transition of the D_2 line of ^{85}Rb as a frequency reference for a laser, which is used as a reference for a ring-cavity. A second laser is stabilized on the line whose absolute frequency is to be measured and is coupled to the same ring-cavity as the first laser. The difference between the frequency of the reference and the unknown frequency is then determined by the ratio of the respective cavity mode numbers [116]. A frequency shift of 954.832(60) MHz of ^{174}Yb with respect to an absolute value of 539 385 606(10) MHz for the ^{176}Yb transition was reported. Therefore, accordingly to [115], the absolute frequency of the ^{174}Yb $^1S_0 - {}^3P_1$ transition (with an uncertainty of 10 MHz due to the dispersion inside the cavity) is

$$\nu_1 = 539\,386\,560(10)\,\text{MHz}.$$

In another work [86] sub-Doppler fluorescence spectroscopy of an Yb atomic beam was performed. The SHG of a master laser was frequency stabilized to the Yb transition and the beat between the master laser and a frequency comb referenced to a hydrogen maser was used to retrieve the absolute frequency of the unknown Yb transition. The authors reported a shift of 954.734(31) MHz between the ^{176}Yb and

the ^{174}Yb isotopes. They also reported a value of 539 385 645 457(87) kHz for the absolute frequency of the $^1S_0 - {}^3P_1$ transition of ^{176}Yb, where the uncertainty was only due to statistics of the data (sample standard deviation). Therefore, the absolute frequency of the ^{174}Yb $^1S_0 - {}^3P_1$ transition accordingly to [86] is

$$\nu_2 = 539\,386\,600\,191(92)\ \text{kHz}.$$

The two values have a shift of 40 MHz, which taking into account the uncertainties, characterize a disagreement between them. The results shown in table 4.1 also enable us to perform a measurement of the frequency of the ^{174}Yb $^1S_0 - {}^3P_1$ transition. To perform this measurement we added a 10:90 fiber splitter before AOM 2 (that is shown in fig. 4.1). The 90% output of the splitter is connected to AOM 2 (and is used as the MOT beams), while the 10% output is sent to another AOM that is driven by an independent DDS. The frequency of the output sinusoidal signal of the DDS is controlled by a function generator that is synchronized with the experimental sequence by the high-speed analog output device (*National instruments* PCIe-6738). The first diffracted order of the AOM is split into two beams, one is sent to an input of a balanced photodetector (Thorlabs PDB230A) and the other (which will be called *green probe*) is aligned to pass through the center of the atomic cloud after 12 ms of TOF. We scan the frequency of the laser around the resonance of the $m_J = 0 \rightarrow m_{J'} = 0$ transition of the ^{174}Yb $^1S_0 - {}^3P_1$ line. Fig. 4.15 show the signal generated by the balanced photodetector (i.e. the difference between the two beams after amplification) alongside a fit of the data by a Voigt profile. The coefficient of determination of the fit (R^2) is 0.993 and its full width at half maximum (FWHM) is 331(2) kHz. The probe beam intensity was $I = 0.6 I_{sat}$. The total frequency shift between the a_{10} hyperfine component of the R(158)25-0 line and the ^{174}Yb $^1S_0 - {}^3P_1$ line is 191 MHz (which includes the frequency shift applied to the green probe and the frequency shift due to AOM 1). Then, the frequency of the ^{174}Yb line (ν_{174}) is given by $\nu_{174} = 539386406 + 191$ MHz, which results in

$$\nu_{174} = 539\,386\,597(6)\ \text{MHz}.$$

This result shows that ν_{174} is in agreement to ν_2, but it is not in agreement to ν_1. Finally, we have shown that despite the large uncertainty of our measurement (6 MHz), we are able to address the discrepancy between the values reported in [115], which is in disagreement with our result, and in [86] that is in agreement with our result. The uncertainty is defined by the uncertainty of the frequency measurement of the iodine line.

4.4 Conclusion of the chapter

A frequency stabilization scheme based on MTS and balanced detection that allows robust laser frequency stabilization using a relatively weak iodine line as

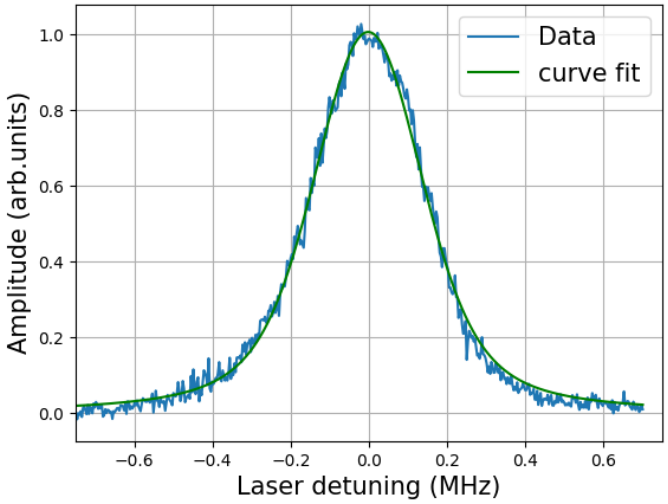

FIGURE 4.15: Amplitude of the signal generated by the transmission of a probe beam through the atomic cloud (see text) versus the laser detuning with respect to the frequency of the transition $m_J = 0 \rightarrow m_{J'} = 0$ of the ^{174}Yb $^1S_0 - {}^3P_1$ line. The measurement was performed after 12 ms of TOF with a laser frequency scan rate of 2 MHz ms^{-1}.

reference was shown. The frequency reference (a_{10} hyperfine component of the R-(158)25-0 line of $^{127}I_2$) is convenient due to its small frequency shift with respect to the $^1S_0 - {}^3P_1$ transition of ^{174}Yb (191 MHz), which can be simply reached by the combination of two AOMs. The dependence of the generated error signal with respect to laser power was characterized and the frequencies of the fifteen hyperfine components of the R-(158)25-0 line was measured. The stabilized laser was characterized by its noise power spectral density and the Allan deviation of its fractional frequencies (i.e. frequency instability). A minimum frequency instability of 3.9×10^{-13} (which corresponds to 210 Hz) was measured for an averaging time of 0.17 s.

It is important to highlight that the frequency stabilization technique that was used in this work to stabilize the frequency of the laser to a relatively weak line can be applied to other weak molecular (or atomic) lines. Indeed, the a_{15} hyperfine component of the R-(158)25-0 line is the closest reported line to the $^1S_0 - {}^3P_1$ transition of the ^{172}Yb, with a shift of 910(6) MHz between them. It is known that MTS signals depend on the internal atomic (molecular) structure, i.e. the amplitude of the MTS signal is not directly proportional to the amplitude of the respective saturated absorption signal [117]. Neglecting the effects due to the molecular internal structure, we anticipate that an iodine line indicated in [118] with a wavenumber of 17 288.5915 cm^{-1} should have a relative amplitude similar to the components of the R-(158)25-0 line shown in this thesis and can be used as frequency reference for the clock transition ($^1S_0 - {}^3P_0$) of ^{171}Yb, which has an absolute frequency of 518 295 836 590 863.75(14) Hz [119]. Another weak iodine line, reported in [118] with an wavenumber of 15 972.4149 cm^{-1} could be suitable as a reference for laser

cooling of Dy [120] in a narrow transition [121]. A different technique used to stabilize lasers to weak atomic transitions consists in the use of cavities to enhance a FM spectroscopy signal. In [90] this method was introduced to use a molecular gas at low pressure as a frequency reference. In their case the transit-time broadening ($\Delta\nu_{tt} = \frac{\sqrt{\frac{2k_bT}{m}}}{4w_0}$), where w_0 is the waist of the beam, is the most important source of linewidth broadening. The authors show that in such conditions the saturation power of the transition can be as high as 50 W.

An optimization of the parameters for the transfer of the atoms from the blue to the green MOT was performed by analyzing absorption images of the atomic cloud for different parameters (magnetic field gradient, MOT beam intensities and MOT beams detuning). A temperature of the cloud of 60 µK was retrieved by time-of-flight experiments for a cloud with 2×10^8 atoms, $b_0 = 47$ and $n_0 = 4.7 \times 10^{11}$ atoms cm^{-3}. It is important to mention that these are the first systematic measurements of the green MOT properties in this system, therefore we expect that after further optimization these values will be improved. But the on-resonance optical depth (b_0) that was obtained indicates that experiments on collective effects in cold atomic samples can already be performed.

To improve the MOT, we can add a step on the sequence shown in fig. 4.8 during which we increase the intensity of the green MOT beams, which accordingly to eq. (3.10) does not affect the atomic density, decrease the laser beam detuning to obtain a lower cloud temperature (given by eq. (3.4)), and simultaneously increase the magnetic field gradient (∇B_z) to compensate the decrease of the atomic density due to the laser detuning. Two additional techniques to either increase the number of atoms trapped in the blue transition [114] or to load the MOT directly on the green transition [52] will be used to improve the number of trapped atoms. However, one can already compare the results shown in this chapter with the Yb MOT with larger number of atoms that have already been reported. Indeed, laser cooling and trapping of more than 1×10^9 atoms Yb atoms in the $^1S_0 - {}^3P_1$ transition was reported by directly loading the atoms in a green MOT (i.e. without a blue MOT) for longer loading times (more than 5 s). The trapping of more than 1×10^9 atoms Yb atoms in the green transition was also achieved by directly loading the atoms in the green transition by spatially arranging the laser beams in a core-shell geometry [52]. The authors arranged the laser beams in a geometry where the green beams are in the center of the MOT (core) and the blue beams (shell) surround this core. I believe that a proper implementation of this core-shell geometry in the experiment would improve the current system, since the number of atoms in the blue MOT would not be a limitation anymore.

Chapter 5

Predictions of the self-consistent theory for 2D Anderson localization of light

When it comes to experiments aiming the observation of localization effects one important issue is to obtain a clear signature of such effect. Therefore, in the project in which this thesis was developed (*Anderson localization of light by cold atoms*), besides the construction of the experiment, obtaining a clear signature of localization is a priority. One approach developed in the group established a connection between 3D Anderson transition and intensity fluctuations of the light scattered by an atomic sample [122]. However, it is desired to obtain an even simpler type of signature not depending on detecting the fluctuations of the scattered light, which requires long integration times.

The so called "transverse localization" [123] is a well-known signature of localization that links the spread of the spatial mode of an optical beam when propagating through a sample to the Anderson transition. Two theoreticians, Romain Bachelard and João Vítor Ferreira, from the Federal University of São Carlos (UFSCAR) are developing, in collaboration with our group, simulations based on the so-called coupled dipole model [124] to study transverse localization of light in cold atomic samples. However, simulating a large number of atoms and high densities in three dimensions is not feasible due to computational power. The simulations are, therefore, being performed in two dimensions. In parallel, we have been developing a theoretical work based on the self-consistent theory of localization to compare its predictions to the results obtained by the simulations. This theoretical work is being developed in collaboration with Sergey Skipetrov from the Laboratoire de Physique et Modélisation des Milieux Condensés (Grenoble).

The self-consistent theory of localization was introduced in [125] to extend the limits of the results obtained by perturbation theory, that is not valid at the vicinity of the Anderson transition. More recently, a theory based on the self-consistent theory predicted a position dependence of the diffusion coefficient [126]. Such theory was successfully implemented for quasi-1D [127] and 3D systems [128]. The goal of this chapter is to calculate the position-dependent diffusion coefficient for

two-dimensional systems by numerically solving the self-consistent equation for the diffusion coefficient and the respective diffusion equation.

5.1 Self-consistent theory for localization of light in 2 dimensions

The goal of this chapter is to solve the self-consistent equations for the diffusion coefficient $D(\mathbf{r}, \Omega)$ and the average intensity Green's function defined below

$$C(\mathbf{r}, \mathbf{r}', \Omega) = \frac{4\pi}{v_E} \langle G^*(\mathbf{r}, \mathbf{r}', \Omega_0 + \frac{\Omega}{2}) G(\mathbf{r}, \mathbf{r}', \Omega_0 - \frac{\Omega}{2}) \rangle, \tag{5.1}$$

where $G(\mathbf{r}, \mathbf{r}', \Omega)$ is the Green's function of a disordered Helmholtz equation.

Eq. (5.2) is the self-consistent diffusion equation in 2D and eq. (5.3) is the self-consistent equation for the position-dependent diffusion coefficient $(D(\mathbf{r}, \Omega))$. These equations, for the case of a position-dependent diffusion coefficient were introduced in [126] and derived in [129]. The self-consistent equation for the position-dependent diffusion coefficient (eq. (5.3)) was already applied to study localization in disordered waveguides [127]. Eq. (5.4) specifies the boundary conditions for a border that divides a diffuse medium and vacuum [130]. v_E represents the energy transport velocity, $\mathbf{r}'$ is the position of the light emission inside the sample, $\delta(\mathbf{r} - \mathbf{r}')$ represents Dirac delta function, l is the mean free path, k represents the wave number and $\mathbf{n}$ is a unit vector normal to the border of the sample pointing to its interior.

$$[-i\Omega - \nabla_r \cdot D(\mathbf{r}, \Omega) \nabla_r] C(\mathbf{r}, \mathbf{r}', \Omega) = \delta(\mathbf{r} - \mathbf{r}'), \tag{5.2}$$

$$\frac{1}{D(\mathbf{r}, \Omega)} = \frac{1}{D_B} + \frac{4}{kl} C(\mathbf{r}, \mathbf{r}, \Omega), \tag{5.3}$$

$$C(\mathbf{r}, \mathbf{r}', \Omega) - \frac{2l}{3} \frac{D(\mathbf{r}, \Omega)}{D_B} (\mathbf{n} \cdot \nabla) C(\mathbf{r}, \mathbf{r}', \Omega) = 0, \tag{5.4}$$

where D_B is the diffusion coefficient in the absence of localization effects, which in 2D is

$$D_B = \frac{v_E l}{2}. \tag{5.5}$$

For the results shown in this chapter it will be assumed that $v_E = c$, where c is the speed of light in vacuum. This assumption is in agreement to off-resonance scattering. For resonant scatters v_E can differ from c by almost 5 orders of magnitude (in 3D) [131]. Therefore, v_E will be modified to match the case of a (2D) atomic system in the future of the project. But as in this chapter most of the results will be normalized by D_B, the conclusions will not depend on the exact expression of D_B. $C(\mathbf{r}, \mathbf{r}', t)$ defined as

$$C(\mathbf{r}, \mathbf{r}', t) = \frac{1}{2\pi} \int_{-\infty}^{\infty} C(\mathbf{r}, \mathbf{r}', \Omega) e^{-\Omega t} d\Omega \tag{5.6}$$

is interpreted as the probability density that a wave packet can be observed in the position $\mathbf{r}$ at time t given that it was emitted in the position $\mathbf{r}'$ at time t' [128, 129]. All along this chapter it will be assumed $\Omega = 0$, implying that eq. (5.18) describes stationary diffusion flow. Within the second term on the right side of eq. (5.3), $C(\mathbf{r}, \mathbf{r}')$ represents the average "return probability", established by constructive interference of reciprocal paths at the designated position.

Solutions of eqs. (5.2) and (5.4) with the self-consistent correction of the diffusion coefficient (eq. (5.3)) were already found for 3D systems [128]. The equations were solved by discretizing them and solving the remaining system of linear equations. Before the discretization, eq. (5.2) was Fourier transformed in two spatial directions, and the medium was assumed to be infinitely large in these directions. The goal of the chapter is to calculate the position-dependent diffusion coefficient in 2D. We are interested in calculating the transverse profile of the transmission of a laser beam incident into the medium. Differently from the 3D case, there is no Anderson transition in two dimensions, at least not in the scalar model [132]. Indeed, it is argued in the famous "gang of four" article [8] that there is not a truly "conductor" behaviour in 2D. A small 2D system behaves like a conductor, but it will be an insulator if the system is large enough [133]. In other words, for infinitely large 2D systems all states are localized. Indeed, a previously reported correction to the (position-independent) diffusion coefficient in 2D shows a dependence with the size of the sample [134]. Preliminary analytical results (see appendix B), indicate a correction to the position-independent diffusion coefficient of a 2D slab of the form $D = D_B \left[1 - \frac{\ln \frac{\mu W}{l}}{2\pi k l}\right]$, where W is the longest slab's length. Therefore, we also expect that the width of the transversal intensity beam profile will depend on the dimensions of the system. As this behaviour is not expected in the 3D case, it may prevent the use of results obtained in 2D to interpret experimental results in 3D which was the main goal of this project, however localization of light in two dimensions remains a topic that attracts interest [132] making the results that are sought in this chapter interesting for different types of systems. 2D Anderson localization was already reported for different kinds of waves, including microwaves [135], ultrasound [134], matter-waves [136, 137] and light [138, 139]. But, no theoretical results including a position-dependent diffusion coefficient was reported for 2D samples.

5.1.1 Diffusion coefficient in 2D (self-consistent)

Originally, the self-consistent theory of localization assumed a (self-consistent) dependence of eq. (5.2) (for a position independent diffusion coefficient) to eq. (5.3). Accordingly, efforts were directed towards finding analytical solutions for $D(\Omega)$. After the concept of a position-dependent diffusion coefficient ($D(\mathbf{r}, \Omega)$) was introduced [126], the search began for numerical solutions to the self-consistent equations. The numerical solutions were advantageous because they could be applied

to a large variety of geometries. The implementation of the discretization and the solution of the resultant system of linear equations is detailed below:

1. Eqs. (5.2) to (5.4) are discretized in grids on x and z. The positions of the grids are indicated by the indices i ($i = 1, 2...I$) and j ($j = 1, 2...J$), resulting in I terms for the x direction and J for z. Then, $x_i = (i-1)\Delta x$ where $\Delta x = \frac{W}{I-1}$ is the width of the grid in the x direction and $z_j = (j-1)\Delta z$ where $\Delta z = \frac{L}{J-1}$ is the width of the grid in the z direction. The discretization is performed by using the following relations

$$\delta(\mathbf{r}-\mathbf{r}') = \frac{1}{\Delta x \Delta z}\delta_{ii'}\delta_{jj'} \tag{5.7}$$

$$\left.\frac{\partial u}{\partial x}\right|_{x=i,z=j} = \frac{u_{(i+1)j} - u_{(i-1)j}}{2\Delta x}, \tag{5.8}$$

$$\left.\frac{\partial u}{\partial z}\right|_{x=i,z=j} = \frac{u_{i(j+1)} - u_{i(j-1)}}{2\Delta z}, \tag{5.9}$$

$$\left.\frac{\partial^2 u}{\partial x^2}\right|_{x=i,z=j} = \frac{u_{(i+1)j} - 2u_{ij} + u_{(i-1)j}}{\Delta x^2}, \tag{5.10}$$

$$\left.\frac{\partial^2 u}{\partial z^2}\right|_{x=i,z=j} = \frac{u_{i(j+1)} - 2u_{ij} + u_{i(j-1)}}{\Delta z^2}. \tag{5.11}$$

Where $\delta_{ii'}$ indicates the Kronecker delta, defined as

$$\delta_{ab} = \begin{cases} 0 & \text{for} \quad a \neq b \\ 1 & \text{for} \quad a = b \end{cases}. \tag{5.12}$$

2. Write the system of equations that results from step 1.

$$\begin{aligned} -\frac{\delta_{ii'}\delta_{jj'}}{\Delta x \Delta z} =& \frac{1}{(2\Delta x)^2}[D_{(i+1)j} - D_{(i-1)j}][C_{(i+1)j,i'j'} - C_{(i-1)j,i'j'}] \\ &+ \frac{D_{ij}}{(\Delta x)^2}[C_{(i+1)j,i'j'} - 2C_{ij,i'j'} + C_{(i-1)j,i'j'}] \\ &+ \frac{1}{(2\Delta z)^2}[D_{i(j+1)} - D_{i(j-1)}][C_{i(j+1),i'j'} - C_{i(j-1),i'j'}] + \\ &+ \frac{D_{ij}}{(\Delta z)^2}[C_{i(j+1),i'j'} - 2C_{ij,i'j'} + C_{i(j-1),i'j'}], \end{aligned} \tag{5.13}$$

$$C_{1j,i'j'} - \frac{2lD_{1j}}{3D_B\Delta x}[C_{2j,i'j'} - C_{1j,i'j'}] = 0 \tag{5.14}$$

$$C_{Ij,i'j'} + \frac{2lD_{Ij}}{3D_B\Delta x}[C_{Ij,i'j'} - C_{(I-1)j,i'j'}] = 0 \tag{5.15}$$

$$C_{i1,i'j'} - \frac{2lD_{i1}}{3D_B\Delta z}[C_{i2,i'j'} - C_{i1,i'j'}] = 0 \tag{5.16}$$

$$C_{iJ,i'j'} + \frac{2lD_{iJ}}{3D_B\Delta z}[C_{iJ,i'j'} - C_{i(J-1),i'j'}] = 0, \tag{5.17}$$

$$\frac{1}{D_{ij}} = \frac{1}{D_B} + \frac{4}{kl} C_{ij,ij}. \tag{5.18}$$

In $C_{ij,i'j'}$ the indices indicates the probability density that a wave packet can be measured at position (i, j) given that it was emitted at position (i', j'). A geometrical representation of the discretized sample is shown in fig. 5.1.

3. Eqs. (5.13) to (5.17) can be written in matrix form for given values of i' and j' as

$$\begin{pmatrix} A_{11} & \cdots & A_{1(IxJ)} \\ \vdots & \ddots & \vdots \\ A_{(IxJ)1} & \cdots & A_{(IxJ)(IxJ)} \end{pmatrix} \begin{pmatrix} C_{11} \\ \vdots \\ C_{ij} \\ \vdots \\ C_{IJ} \end{pmatrix} = \frac{\delta_{ii'}\delta_{jj'}}{\Delta x \Delta z} \begin{pmatrix} 1 \\ \vdots \\ 1 \end{pmatrix}, \tag{5.19}$$

where the elements of the A matrix are the coefficients that multiply the C elements. By inspection of eqs. (5.13) to (5.17) we realize that the matrix A is a sparse matrix (most of its elements are equal to zero). Eq. (5.19) defines a system of $I \times J$ linear equations (for a fixed source position $\{i', j'\}$). The matrix A is formed by its main diagonal, that is composed by the elements that multiply C_{ij} for the $i \times j$ equation in eq. (5.13), and in one of eqs. (5.14) to (5.17) once $i = I$, $i = 1$, $j = 1$ or $j = J$; two lower diagonals, that are composed by the elements that multiply $C_{(i-1)j}$ or $C_{i(j-1)}$ in eq. (5.13) for the $i \times j$ equation or in eqs. (5.15) and (5.17) if $i = I$ or $j = J$; and two upper diagonals, that are composed by the elements that multiply $C_{(i+1)j}$ and $C_{i(j+1)}$ in eq. (5.13) for the $i \times j$ equation or in eqs. (5.14) and (5.16) if $i = 1$ or $j = J$. Therefore, we can write the A matrix as follows

$$A = \begin{pmatrix} A_{11} & A_{12} & 0 & \cdots & 0 & A_{1(J+1)} & 0 & \cdots & \cdots & 0 \\ A_{21} & A_{22} & A_{23} & 0 & \cdots & 0 & A_{2(J+2)} & \ddots & & \vdots \\ 0 & \ddots & \ddots & \ddots & \ddots & \ddots & \ddots & \ddots & \ddots & \vdots \\ \vdots & \ddots & \ddots & \ddots & \ddots & \ddots & \ddots & \ddots & \ddots & 0 \\ 0 & \ddots & \ddots & \ddots & \ddots & \ddots & \ddots & \ddots & \ddots & A_{(IxJ-J)(IxJ)} \\ A_{(I+1)1} & \ddots & \ddots & \ddots & \ddots & \ddots & \ddots & \ddots & \ddots & 0 \\ 0 & A_{(I+2)1} & \ddots & \ddots & \ddots & \ddots & \ddots & \ddots & \ddots & \vdots \\ \vdots & \ddots & \ddots & \ddots & \ddots & \ddots & \ddots & \ddots & \ddots & 0 \\ \vdots & & \ddots & \ddots & \ddots & \ddots & \ddots & \ddots & \ddots & A_{(IxJ-1)(IxJ)} \\ 0 & \cdots & \cdots & 0 & A_{(IxJ)(IxJ-I)} & 0 & \cdots & 0 & A_{(IxJ)(IxJ-1)} & A_{(IxJ)(IxJ)} \end{pmatrix}.$$

4. Eq. (5.19) should be solved $I \times J$ times for different (point) source positions (i.e. for all possible values of (i', j')), for given grid dimensions $(\Delta x, \Delta z)$. Initially for a constant value of the diffusion coefficient ($D_{i,j} = D_B$). From each of the $I \times J$ solutions, the value of $C_{ij,ij}$ (the return probability density) will be retrieved. In other words, after solving eq. (5.19) for one given source position $\{i, j\}$, just

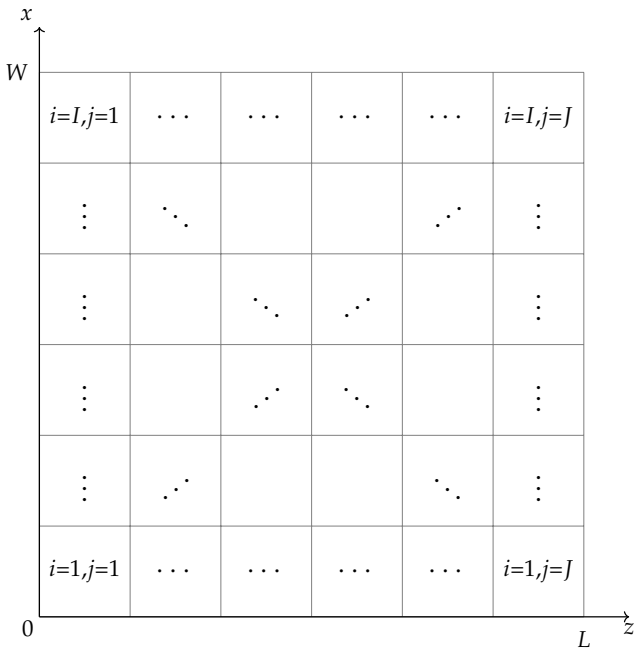

FIGURE 5.1: Representation of the discretization of a 2D sample of size L in the z direction and W in x direction with the values of the grids' indices (i and j). The dots indicate that there may be more grids than shown in the figure.

one value is stored ($C_{ij,ij}$).

5. The values of $C_{ij,ij}$ are inserted in eq. (5.18) to calculate the renormalized position-dependent diffusion coefficient (D_{ij}).

6. D_{ij} calculated in the previous step is used to solve eqs. (5.13) to (5.17) again and new values of $C_{ij,ij}$ are retrieved. These results are again inserted in eq. (5.18) to calculate the new values of the position-dependent diffusion coefficient D_{ij}^{new}. The difference between the previous diffusion coefficient and the new one is calculated ($D_{ij} - D_{ij}^{new}$) and the largest element (ΔD_{max}) is retrieved. The procedure is repeated until ΔD_{max} satisfies a criterion of convergence. In this work we assume that the calculation converged if ΔD_{max} is less than 10^{-3}% of the diffusion coefficient (at the same position of ΔD_{max}) calculated in the previous iteration. This results in a number of iterations ranging from 5 to 100 for the data shown in this thesis, depending on the value of kl and the geometry of the sample.

5.1.2 Solution of the discretized diffusion equation in 2D

The solution of eq. (5.19) is retrieved by a software written in python that uses the package *scipy.sparse* to efficiently solve the system of linear equations defined in eq. (5.19). Initially, the system of equations is solved for $D_{ij} = D_B$. Fig. 5.2a shows a heat map of of the solution ($C(\mathbf{r}, \mathbf{r'})$) for a square medium of sizes $L = W = 40l$, $kl = 3$ and a point source in its center. Fig. 5.2b is a plot of the solution along z for

a value of $x = x'$ for different grid sizes. The solution in the vicinity of the source's position ($C(\mathbf{r'}, \mathbf{r'})$) increases when the length of the grid (the grid length is in units of l) is decreased. This divergence arises from the fact that the fundamental solution of eq. (5.18) for $\Omega = 0$ and $D(\mathbf{r}) = D_B$ is $C(\mathbf{r}, \mathbf{r'}) = \frac{1}{2\pi} \ln |\mathbf{r} - \mathbf{r'}| +$ constant. Fig. 5.2c is a zoom of fig. 5.2b that highlights the divergence, and fig. 5.2d shows $C(\mathbf{r}, \mathbf{r'})$ for a grid length of $0.2l$ with the horizontal axis in log scale to show that the solution obtained has a logarithmic behaviour far from the source position.

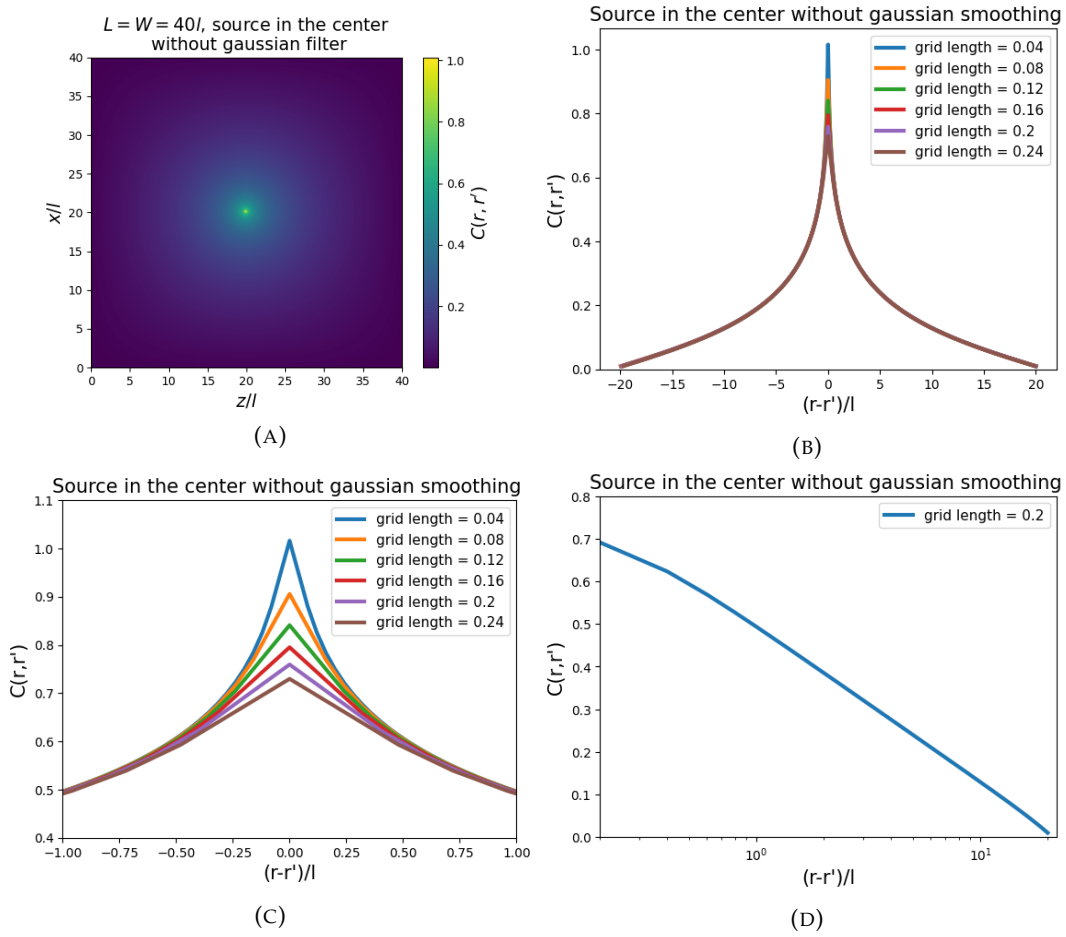

FIGURE 5.2: **(a)** 2D heatmap of C(**r**, **r'**) for a sample of dimensions $L = W = 40l$, $D = D_B$ and source at the center of the square. **(b)** C(**r**, **r'**) in z direction for a value of x on the center of the sample ($x = x'$), the plot is made for different values of grid size (in units of l) to show that $C(\mathbf{r'}, \mathbf{r'})$ increases for smaller grid sizes. **(c)** Zoom of (b) to highlight the increase of $C(\mathbf{r}, \mathbf{r'})$ when the grid size is decreased. **(d)** $C(\mathbf{r}, \mathbf{r'})$ in z direction for a value of x on the center of the sample ($x = x'$) with respect to the source point in semi-log scale, showing its logarithmic dependence away from the source.

To resolve this divergence, taking into account that eq. (5.18) does not hold, physically, for length scales smaller than l we apply a gaussian filter (also known as Weierstrass transform) to the result shown in fig. 5.2a. The application of a filter to the matrix C_{ij} is given by the operation [140]

$$C_{ij,filt} = \sum_{(k,l) \in R_H} C_{(i+k)(j+l)} \cdot H_{kl}, \tag{5.20}$$

where H corresponds to the filter kernel and R_H denotes the set of coordinates covered by the filter. The elements of a gaussian filter in 2D are defined by the 2D gaussian function

$$H(x,z) = \frac{1}{2\pi\sigma^2} e^{-\frac{x^2+z^2}{2\sigma^2}}. \tag{5.21}$$

σ denotes the standard deviation of the filter (assumed equal for both directions). H is a square matrix with an odd number of columns and rows. The indices of the matrix are defined so that $k = l = 0$ at the center of the matrix, therefore they assume negative values as well. Below is shown one example of a H matrix that is truncated for $|k| = 1$ and $|l| = 1$

$H_{(-1)(-1)}$	$H_{(-1)0}$	$H_{(-1)1}$
$H_{0(-1)}$	H_{00}	H_{01}
$H_{1(-1)}$	H_{10}	H_{11}

.

The filter is numerically implemented by the package *scipy.ndimage* and the heat map of $C(\mathbf{r},\mathbf{r'})$ after filtering (smoothing) is shown in fig. 5.3a. The standard deviation of the filter was l and the filter was truncated at distances larger than $2l$. Fig. 5.3b is a plot of the solution along z for a value of $x = x'$, and fig. 5.3c is a zoom of fig. 5.3b around z' that highlights the small differences between the values of $C(\mathbf{r'},\mathbf{r'})$ for different grid sizes (in units of l). Fig. 5.3d shows that $C(\mathbf{r},\mathbf{r'})$ remains logarithmic for $|\mathbf{r}-\mathbf{r'}| > 2l$.

5.2 Results

5.2.1 Position-dependent diffusion coefficient in 2D

After the application of the Gaussian filter, the matrix $C_{ij,filt}$ is stored and used to calculate the position-dependent diffusion coefficient (D_{ij}) by eq. (5.3). The new diffusion coefficient is subtracted from the diffusion coefficient before the iteration. The process is repeated until the maximum difference between two consecutive diffusion coefficients for a given position (that is at least l far from the border) is less than 10^{-3}% of the diffusion coefficient calculated in the previous iteration. Due to the difficulty on handling the filtering of points on the border of the sample, we redefine them. For the points that are at a distance smaller than l from the points that

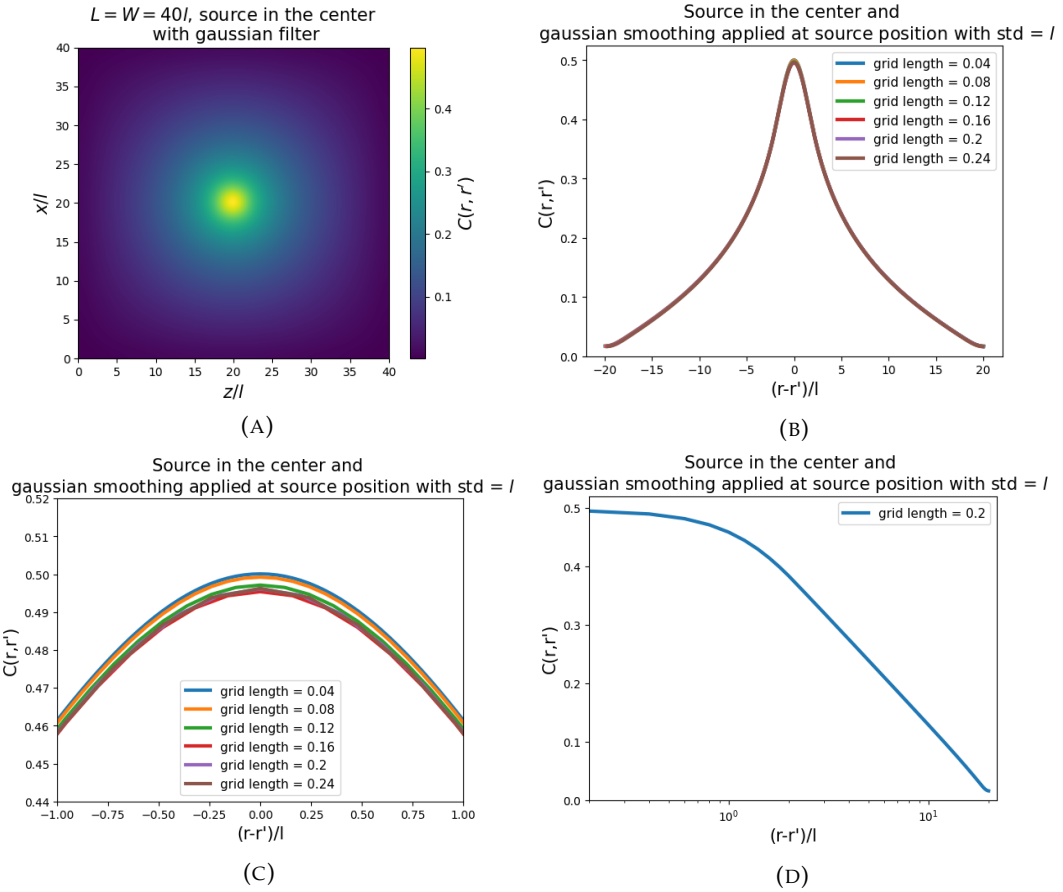

FIGURE 5.3: **(a)** 2D heatmap of C(**r**, **r'**) for a sample of dimensions $L = W = 40l$, $D = D_B$ and source at the center of the square after the application of a gaussian filter with standard deviation l and truncated for points that are at a distance $2l$ from the source. **(b)** $C(\mathbf{r}, \mathbf{r'})$ in z direction for a value of x on the center of the sample ($x = x'$), the plot is made for different values of grid size to show that $C(\mathbf{r'}, \mathbf{r'})$ does not increase as without the application of the filter. **(c)** Zoom of (a) to highlight the behaviour of $C(\mathbf{r}, \mathbf{r'})$ with the application of the gaussian filter. **(d)** $C(\mathbf{r}, \mathbf{r'})$ in z direction for a value of x on the center of the sample ($x = x'$) with respect to the source point in semi-log scale and after the application of a gaussian filter, showing its logarithmic dependence away from the source.

are exactly on the border of the matrix D_{ij} (the point at the border included) a linear extrapolation is performed, i.e. $D_{ij} = 2D_{(i+1)j} - D_{(i+2)j}$ for points in the vicinity of the border at $i = 1$; $D_{ij} = 2D_{(i-1)j} - D_{(i-2)j}$ for points in the vicinity of the border at $i = I$; $D_{ij} = 2D_{i(j+1)} - D_{i(j+2)}$ for points in the vicinity of the border at $j = 1$ and $D_{ij} = 2D_{i(j-1)} - D_{i(j-2)}$ for points in the vicinity of the border at $j = J$. The whole calculation was performed for $kl = 3$ for five different values of W and the results are shown in fig. 5.4. One can see that the higher the value of W, the smaller the minimum value of $D(x, z)$ is. Fig. 5.5 is a plot of $D(x, z)$ along z for $x = \frac{W}{2}$.

Calculations for different values of kl for square media ($L = W = 40l$) were also performed. As expected, the results depicted in fig. 5.6 show that the position dependent diffusion coefficient decreases by decreasing kl. D_B depends on l as shown in eq. (5.5), therefore for each value of kl we normalize $D(x, z)$ by the value of D_B that corresponds to its kl ($D_B = \frac{v_E l}{2}$). A plot of the diffusion coefficient along z for

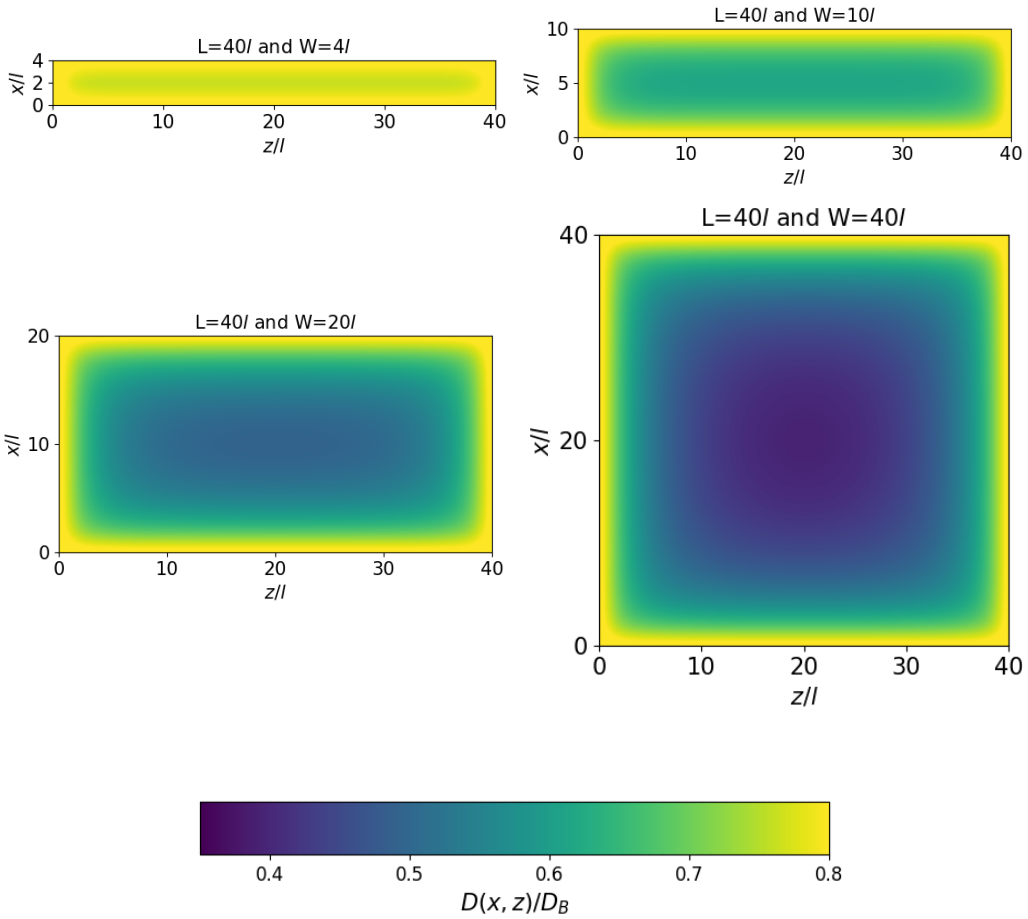

FIGURE 5.4: Heat maps of the position-dependent diffusion coefficient obtained by self-consistent theory of localization for $kl = 3$, $L = 40l$ and varying the transverse width of the medium (W). The color scale for the diffusion coefficient is shown on the bottom of the figure.

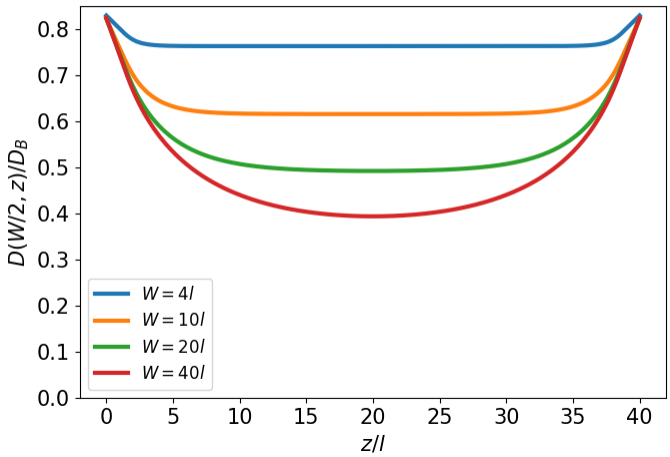

FIGURE 5.5: Position-dependent diffusion coefficient along the z direction in the center of the x axis ($x = \frac{W}{2}$) for different values of W, for $L = 40l$ and $kl = 3$.

$x = \frac{W}{2}$ is shown in fig. 5.7a, with the vertical axis in log scale and normalized by the same value (D_B for $kl = 100$). We can observe a difference of about 6 orders of magnitude in $D(x, z)$ from $kl = 100$ to $kl = 0.9$ at the center of the square.

To illustrate the exponential convergence (which is relatively fast) of the calculations, fig. 5.8a shows the value of the maximum difference between two diffusion coefficients calculated from subsequent iterations (ΔD_{max}), and fig. 5.8b the value of the diffusion coefficient at the same position of ΔD_{max} (D_{max}). The results shown are for a sample of size $L = 40l$ and $W = 10l$. We can see that the number of iterations depends on kl. Indeed, it was verified that the larger kl is, the fewer iterations are needed.

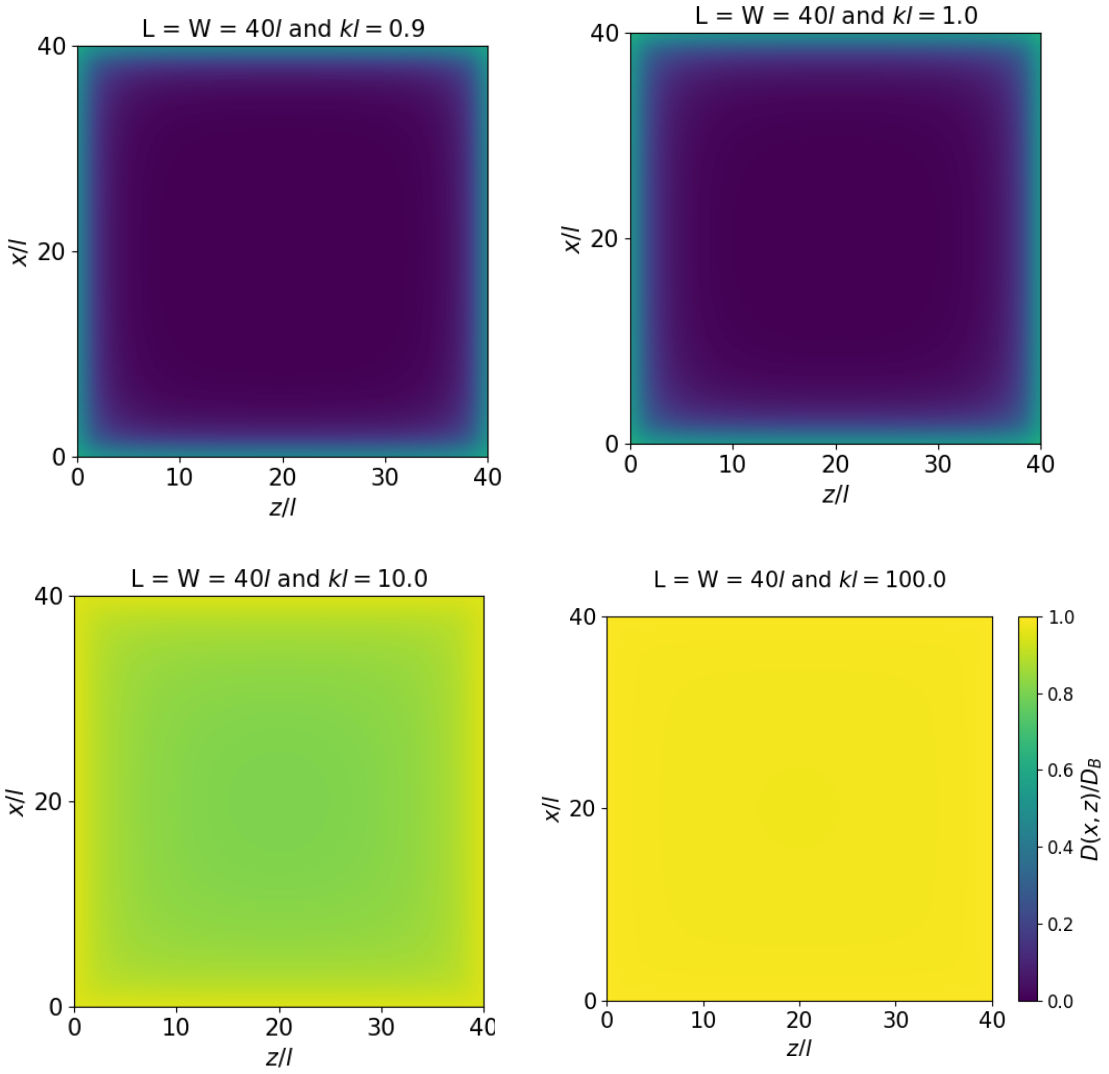

FIGURE 5.6: Heat maps of the position-dependent diffusion coefficient obtained by self-consistent theory of localization for $L = W = 40l$ and varying kl. The color scale for the diffusion coefficient is shown on the right side of the last heat map and is the same for the four maps that are shown.

It can be noticed from fig. 5.7, that $D(x, z)$ with respect to kl varies much more in

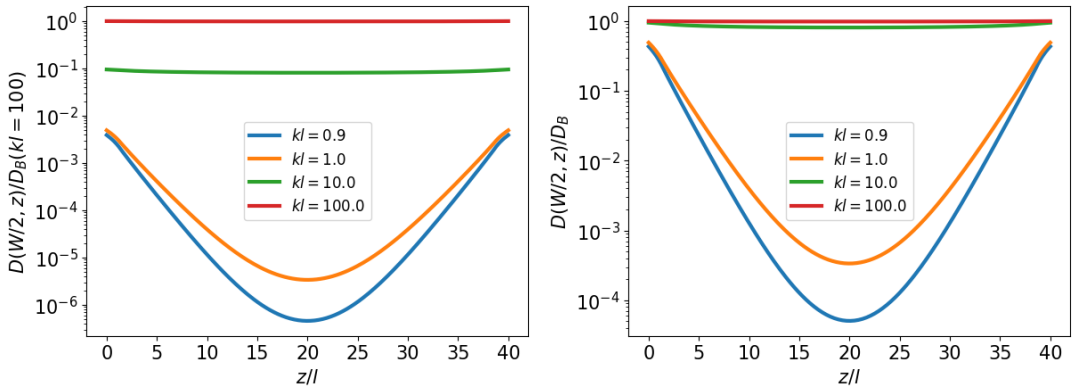

(A) (B)

FIGURE 5.7: Position-dependent diffusion coefficient, divided by the value of D_B for $kl = 100$, along the z direction in the center of the x axis ($x = \frac{W}{2}$) for different values of kl, and for $L = W = 40l$.(B) Position-dependent diffusion coefficient, divided by the value of D_B for each different value of kl, i.e. for $kl = 100$ the value of D_B is 10 times larger than the one for $kl = 10$.

the center of the sample than in the borders. So, in fig. 5.9 we plot the minimum values of $D(W/2, L/2)/D_B$ (the values at the center of the medium) and $D(Border)/D_B$ for four different values of kl and $L = W = 40l$. From $kl = 1$ to $kl = 3$ the diffusion coefficient in the center of the sample varies by three orders of magnitude, while at the borders it changes by less than 50%.

5.3 Conclusion of the chapter

In this chapter the calculation of the position-dependent diffusion coefficient in two dimensions was developed based on the self-consistent theory of localization. The calculation is based on the discretization of the diffusion equation and the self-consistent correction of the diffusion coefficient. The details about each step on the solution of such set of discretized equations was provided. The position-dependent diffusion coefficients that were obtained for different values of size of the medium along the x axis and kl are going to be used to calculate predictions of transverse localization experiments in two dimensions. An additional perspective is the generalization of the method to finite-size three dimensional systems and include the time dependence of the average intensity Green's function. A possible application of such 3D results would be a self-consistent analysis of a 3D disordered medium that is excited in its center (instead of in its borders). The excitation in the center of a cold atomic system is possible and its implementation is currently being performed on the experimental setup described in chapters 3 and 4.

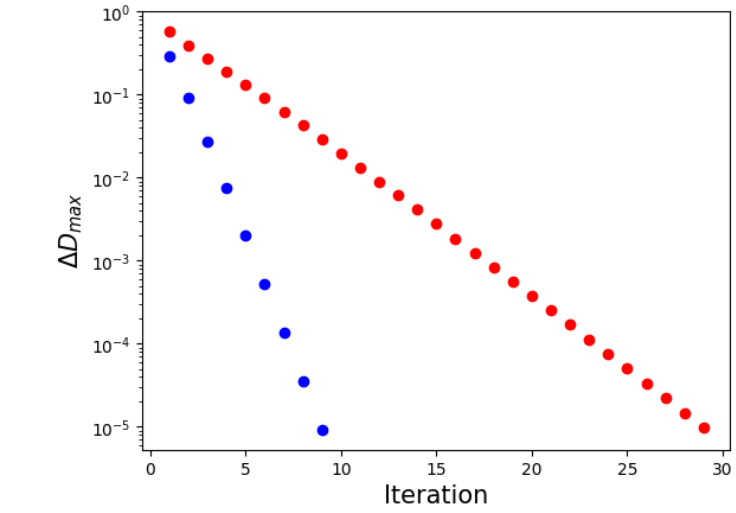

(A)

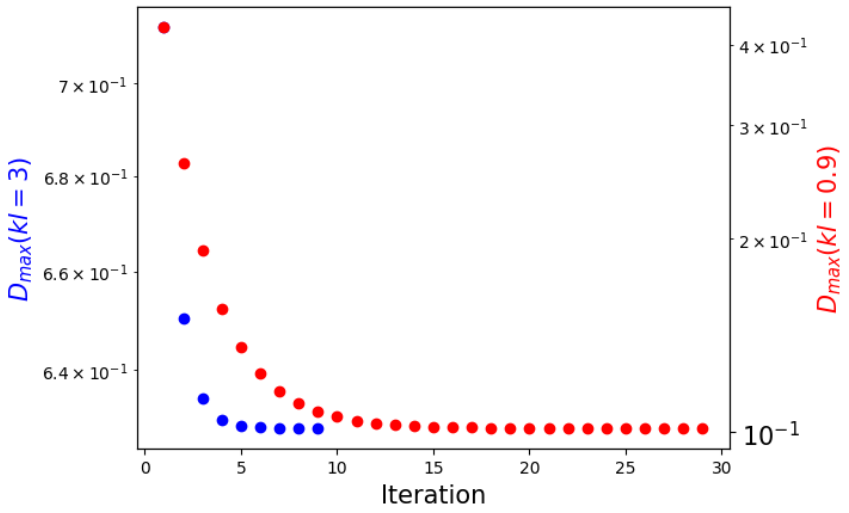

(B)

FIGURE 5.8: (A) Maximum difference between two diffusion coefficients calculated from subsequent iterations (ΔD_{max}). And (B) The value of the diffusion coefficient at the same position of ΔD_{max}. The calculations shown were performed for a sample of size $L = 40l$ and $W = 10l$.

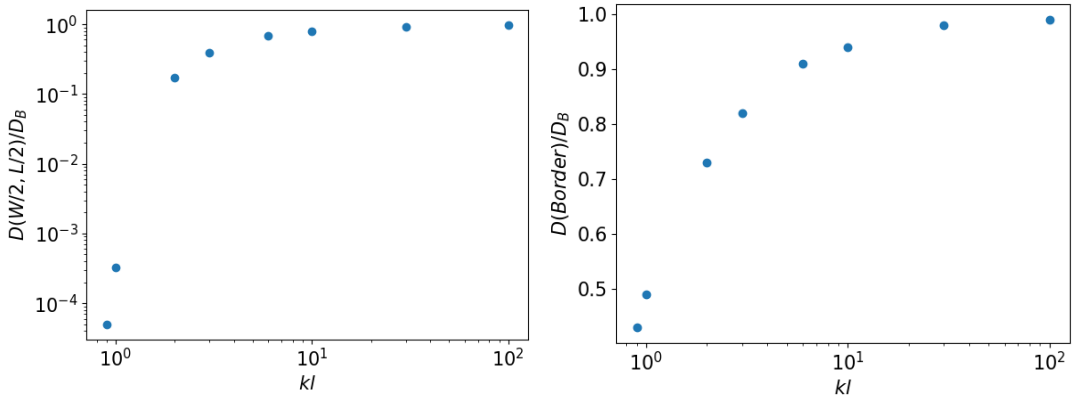

(A) (B)

FIGURE 5.9: (A) Position-dependent diffusion coefficient in the center of the sample with respect to kl. (B) Position-dependent diffusion coefficient in the border of the sample with respect to kl. The data are for samples of size $L = W = 40l$.

Chapter 6

Conclusion and perspectives

6.1 Conclusion

The construction of a magneto-optical trap (MOT) of ^{174}Yb was performed. The first step was the loading of a MOT in the $^1S_0 - {}^1P_1$ transition, with up to 1×10^9 atoms and a maximum loading rate of 3×10^9 atoms s^{-1}. Details on the laser system that provides up to 2.5 W at 399 nm are discussed. The 555.8 nm laser was frequency stabilized by balanced detection and modulation transfer spectroscopy of molecular iodine ($^{127}I_2$). The frequency reference was a hyperfine component of the R-(158)25-0 line of $^{127}I_2$. This line is weaker than the lines used in previous works, however it is convenient due to its small frequency shift with respect to the $^1S_0 - {}^3P_1$ ^{174}Yb transition (191 MHz). Sub-Doppler spectroscopy of all the hyperfine components of the R-(158)25-0 line was reported, alongside a measurement of the frequency of the $^1S_0 - {}^3P_1$ ^{174}Yb transition. The achieved laser frequency stability was characterized by means of the laser frequency noise power spectral density and the Allan deviation of the fractional frequencies. The laser frequency stabilization scheme used in the present thesis, and introduced in [87], can be applied to different lines of molecular iodine or other atoms/molecules.

The atoms were transferred to a MOT on the $^1S_0 - {}^3P_1$ transition. 2×10^8 atoms were obtained at a temperature of 60 µK and with an on-resonance optical depth (b_0) of 47. This value of b_0 is sufficient to perform experiments on collective effects in cold atomic samples. Additionally, an atomic density of 4.7×10^{11} atoms cm^{-3} was measured. This value is below the critical value for observation of magnetic-field-driven localization by four orders of magnitude. Therefore, ideas for the optimization of the atom number and density are discussed. However, a transfer to a dipole trap or Bose-Einstein condensation may be needed to achieve densities of the order of 1×10^{15} atoms cm^{-3} [32, 33].

The calculation of the position-dependent diffusion coefficient for a 2D sample, based on the self-consistent theory of localization, was discussed. It was shown that a solution to the (self-consistent) diffusion equation and the self-consistent correction to the position-dependent diffusion coefficient can be retrieved by numerically solving the system of linear equations obtained by the discretization of them. The

steps to obtain the solution are explained and a set of position-dependent diffusion coeficients for different parameters (kl and size of the sample) is shown.

6.2 Perspectives

The long-term goal of the project is to obtain a clear experimental signature of localization of light in 3D. The system is currently being prepared to realize experiments with diagonal disorder [22]. To do so, we have a laser system composed by a distributed-feedback laser (DFB), that generates 2 W at 1539 nm (NKT, Koheras BoostiK E15 PM FM). The frequency of the laser can be tuned close to the resonance frequency of the $^3P_1 - {}^3D_1$ transition. This laser was also installed and calibrated during the present thesis, initially by myself and Anaïs Dorne, who performed a master's internship in the experiment; and more recently by Apoorva Singh, who is currently a PhD student working on the experiment. To generate the diagonal disorder, the laser beam intensity profile will be randomly shaped before that it passes through the atomic cloud. The randomly distributed laser intensity profile will generate randomly distributed light-shifts in the $^3P_1$ energy level, which mimics the diagonal disorder of the original Anderson model.

A doubtless experimental signature of localization of light in 3D is still under investigation by collaborators (theoreticians). One part of the project is to study the spread of an excitation generated in the center of the atomic cloud (instead of the propagation of a laser beam through the cloud). This excitation, which is not the excitation by a single photon but the excitation of atoms confined in a volume in the interior of the cloud, will be generated by the application of two beams of the 1539 nm (which will be called 'light-shifter beams') laser orthogonal to each other and a beam generated by the 556 nm laser (which will be called 'green probe'). The light-shifter beams will have the $1/e^2$ width smaller than the width of the atomic cloud. The light-shifter will shift the $^3P_1$ state by a given amount that depends on its frequency and intensity (which are fine-controlled by AOMs) and the green probe will have the exact frequency to excite the atoms that experience the light-shift in the intersection of the two light-shifter beams. In summary, the atoms that will be excited to the $^3P_1$ state will be the ones that are in the intersection between the three beams. The time evolution of this excitation in the center will be studied and it can give information about the existence of localized states. The effect of the light-shifter beam can be (qualitatively) seen in fig. 6.1, which shows an atomic cloud loaded by a green MOT with the application of one light-shifter beam.

The theory developed in chapter 5 will be used to study 'transverse localization' in 2D, i.e. the study of the dependence of the transverse intensity profile of a laser beam that propagates through the sample. The results will be compared to theoretical simulations performed by collaborators. However, an extension of the theory to

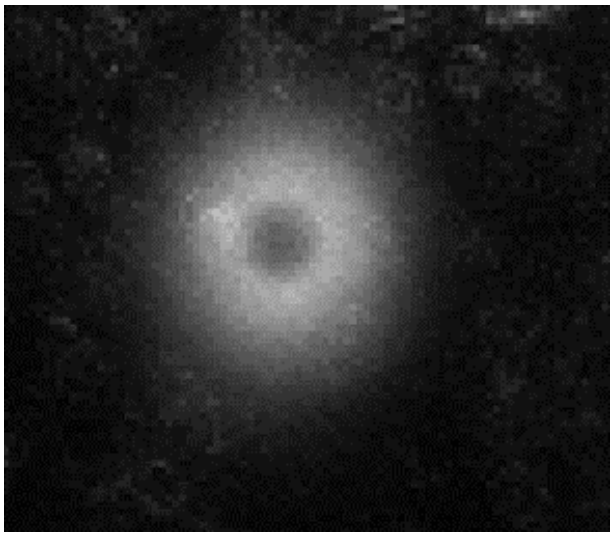

FIGURE 6.1: image of the atomic cloud loaded by a MOT in the ${}^1S_0 - {}^3P_1$ transition with the application of the light-shifter beam in the center of the cloud. The image was taken by the application of a beam near-resonant to the ${}^1S_0 - {}^3P_1$ transition. The ${}^3\mathrm{P}_1$ level of the atoms in the center of the cloud are light-shifted, therefore the imaging beam is not resonant to the ${}^1S_0 - {}^3P_1$ transition of the atoms in the center of the cloud

.

include time dependence is envisaged, as well as its formulation to finite-size samples in 3D. This would allow a study of the 'excitation in the center' by means of the self-consistent theory of localization.

Appendix A

On the indistinguishability of frequency and phase modulation

Modulation is the changing of a carrier signal's ($S(t)$) property by another signal that carries a given information ($m(t)$). When the amplitude of the carrier signal is held constant and its phase is modulated this technique is called, in a general way, *angle modulation*. If the phase of the carrier signal varies linearly with respect to the message signal $m(t)$ this is called *phase modulation (PM)* and if the the first time derivative of the phase varies linearly with respect to $m(t)$ this is called *frequency modulation (FM)*. These types of modulation are mathematically defined below, based in [141], for the case of sinusoidal carrier ($S(t)$) and message ($m(t)$) signals.

Considering

$$S(t) = A\cos\left(2\pi f_c t + \phi(t)\right). \tag{A.1}$$

The definition of phase (Θ) and instantaneous frequency (f_i) are

$$\Theta(t) = 2\pi f_c t + \phi(t) \tag{A.2}$$

$$f_i(t) = \frac{1}{2\pi}\frac{\mathrm{d}\Theta(t)}{\mathrm{d}t} = f_c + \frac{1}{2\pi}\frac{\mathrm{d}\phi(t)}{\mathrm{d}t} \tag{A.3}$$

A.1 Phase modulation

In phase modulation, the phase varies linearly with respect to $m(t)$, i.e.

$$\Theta(t) = 2\pi f_c t + \beta m(t) + B, \tag{A.4}$$

where β and B are constants. Therefore, if $m(t) = A_m\cos\left(\omega_m t\right)$ the output of the PM process will be

$$S_{PM}(t) = A\cos\left(2\pi f_c t + B + \beta A_m\cos\left(\omega_m t\right)\right). \tag{A.5}$$

A.2 Frequency modulation

In FM the first derivative of the phase, and therefore the instantaneous frequency, varies linearly with respect to $m(t)$, i.e.

$$\frac{\mathrm{d}\phi}{\mathrm{d}t} = \alpha m(t), \tag{A.6}$$

where α is a constant. Therefore, if $m(t) = A_m \cos(\omega_m t)$

$$\phi(t) = \alpha \int_{t_0}^{t} A_m \cos(\omega_m t) dt, \tag{A.7}$$

And, the output of the FM process will be

$$S_{FM}(t) = A \cos\left(2\pi f_c t + \alpha \int_{t_0}^{t} A_m \cos(\omega_m t)\right), \tag{A.8}$$

$$= A \cos\left(2\pi f_c t + \alpha \frac{A_m}{\omega_m} \sin(\omega_m t) - \alpha \frac{A_m}{\omega_m} \sin(\omega_m t_0)\right). \tag{A.9}$$

It can be seen from eq.(A.5) and eq.(A.9) that it is not possible, by just measuring the output of the modulation (S_{PM} or S_{FM}) when the modulating signal ($m(t)$) is sinusoidal, to distinguish between FM and PM without further information of $m(t)$ itself [141, 142].

Appendix B

Position-independent diffusion coefficient for a 2D slab

It can be shown that for a disordered (3D) slab confined by the planes $z = 0$ and $z = L$ of a Cartesian reference frame, the (position-independent) diffusion coefficient is given by [128]

$$D(0) = D_B \left[1 - \frac{3\mu}{(kl)^2}\right], \tag{B.1}$$

μ is a constant that arises from the fact that eq. (5.2) does not hold for length scales smaller than l.

The calculation of the 2D case will be performed in the Fourier space, in steady state (i.e. $\Omega \to 0$)

$$C(\mathbf{r}, \mathbf{r}') = \frac{1}{(2\pi)^2} \int d^2\mathbf{q} C(\mathbf{q}) e^{-iq(\mathbf{r}-\mathbf{r}')}. \tag{B.2}$$

From eq. (5.2) we obtain

$$C(q) = \frac{1}{q^2 D}, \tag{B.3}$$

where $q^2 = \mathbf{q} \cdot \mathbf{q}$. ($C(\mathbf{r}, \mathbf{r})$) is

$$C(\mathbf{r}, \mathbf{r}) = \frac{1}{(2\pi)^2} \int d^2\mathbf{q} C(q). \tag{B.4}$$

Eq. (B.4) will be performed considering the geometry of a 2D slab confined by the planes $z = 0$ and $z = L$ (following [128]), which results in

$$\begin{aligned} C(\mathbf{r}, \mathbf{r}) &= \frac{1}{(2\pi)^2} \int_{-\infty}^{\infty} dq_z \int dq_x C(q_x, q_z) \\ &= \frac{1}{(2\pi)^2 D} \int_{-\infty}^{\infty} dq_z \int dq_x \frac{1}{(q_x^2 + q_z^2)} \end{aligned} \tag{B.5}$$

Performing the integral in z,

$$C(\mathbf{r}, \mathbf{r}) = \frac{1}{(4\pi) D} \int_{q_{min}}^{q_{max}} \frac{dq_x}{q_x}. \tag{B.6}$$

A cutoff $q_{max} = \frac{\mu}{l}$ is introduced in the integral over q_x because eq. (5.2) does not hold for length scales smaller than l. The lower cutoff (q_{min}) is due to the divergence

of the integral eq. (B.6) at $q_x = 0$. The need of a lower cutoff in eq. (B.6) implies that the system size at the x direction is relevant for the calculation of $D(0)$ and cannot be assumed infinite as it is done for the 3D case [128]. This is a striking difference between 2D and 3D, and it emphasizes that the size of the sample in 2D plays an important role in the diffusion properties of the medium as discussed in the beginning of chapter 5. We assume $q_{min} = \frac{1}{W}$, where W is the size of the rectangular plate in the x direction, which leads to

$$C(\mathbf{r}, \mathbf{r}) = \frac{1}{(4\pi D)} \ln\left(\frac{q_{max}}{q_{min}}\right) = \frac{1}{(4\pi D)} \ln\frac{\mu W}{l}. \tag{B.7}$$

Inserting eq. (B.7) into eq. (5.3) we retrieve for the diffusion coefficient

$$D = D_B \left[1 - \frac{\ln\frac{\mu W}{l}}{\pi k l}\right]. \tag{B.8}$$

Eq. (B.8) states that the diffusion coefficient in a 2D slab confined by the planes $z = 0$ and $z = L$ has a correction, due to the self-consistent theory, that depends (logarithmically) of the size of the medium on the transverse (x) direction W.

Appendix C

Code to obtain the position-dependent diffusion coefficient in 2D due to the self-consistent theory

```
import numpy as np
import scipy
import matplotlib.pyplot as plt
import gc
from scipy.ndimage import gaussian_filter
import time
import math
import joblib

#Defining the function that displays the heatmap of a 2D array
def heatmap2d(arr: np.ndarray):
    # Ok
    plt.imshow(arr, cmap='viridis',extent=(0,h,0,w))
    plt.colorbar(label="C(r,r')")
    plt.xlim([0,h])
    plt.ylim([0,w])
    plt.xlabel('z axis')
    plt.ylabel('x axis')
    plt.title('Square lattice with source in the center and gaussian
        smoothing')
    plt.show()

#Defining the function that calculates the matrix of the coefficients A
def New_Coefficients(nz,nx,z0,D0):
```

```
# Initializing the matrices that will be used as diagonals of the
    matrix of the coefficients
    DFirstSuper = np.zeros((nx,nz))
    DFirstSub = np.zeros((nx,nz))
    DSecondSuper = np.zeros((nx,nz))
    DSecondSub = np.zeros((nx,nz))
    DMain = np.zeros((nx,nz))
    # Constructing the diagonals of the matrix
    for i in range(nx):
        for j in range(nz):
            if j == 0:
                DMain[i,j] = 1 + ((z0*D0[i,j])/(D*dz))
                DFirstSuper[i,j] = -((z0*D0[i,j])/(D*dz))
            elif j==(nz-1):
                DMain[i,j] = 1 + ((z0*D0[i,j])/(D*dz))
                DFirstSub[i,j] = -((z0*D0[i,j])/(D*dz))
            elif i==0:
                DMain[i,j] = 1 + ((z0*D0[i,j])/(D*dx))
                DSecondSuper[i, j] = -((z0*D0[i,j])/(D*dx))
            elif i==(nx-1):
                DMain[i,j] = 1 + ((z0*D0[i,j])/(D*dx))
                DSecondSub[i,j] = -((z0*D0[i,j])/(D*dx))
            else:
                DMain[i,j] = 2*((dz/dx) + (dx/dz))* D0[i,j]
                DFirstSuper[i,j] = -(dx/(4*dz))*(D0[i,j+1] - D0[i,j-1] +
                    4*D0[i,j])
                DFirstSub[i,j] = (dx/(4*dz))*(D0[i,j+1] - D0[i,j-1] - 4*
                    D0[i,j])
                DSecondSuper[i,j] = -(dz/(4*dx))*(D0[i+1,j] - D0[i-1,j] +
                     4*D0[i,j])
                DSecondSub[i,j] = (dz/(4*dx))*(D0[i+1,j] - D0[i-1,j] - 4*
                    D0[i,j])

# Transform the matrices in single vectors that will be the diagonals
    of the matrix of the coefficients
    DMainFlat = DMain.flatten()
# Bulding the first superdiagnonal matrix
    DFirstSuperFlat = DFirstSuper.flatten()
# Creating the first subdiagonal
    DFirstSubFlat = DFirstSub.flatten()
# Creating the second superdiagonal
    DSecondSuperFlat = DSecondSuper.flatten()
```

```
# Creating the second subdiagonal
    DSecondSubFlat = DSecondSub.flatten()
    DFirstSubFlat_ = DFirstSubFlat
# Shifting the elements inside the array to fit correctly when the
    matrix 'A' is created (see 16 lines below)
    for i in range(nx*nz):
         DFirstSuperFlat[(nx*nz)-i-1] = DFirstSuperFlat[(nx*nz)-i-2]
         DSecondSuperFlat[(nx*nz)-i-1] = DSecondSuperFlat[(nx*nz)-i-nz
             -1]
         if i < nx*nz-1:
             DFirstSubFlat_[i] = DFirstSubFlat_[i+1]
         if i < nx*nz-nz:
            DSecondSubFlat[i] = DSecondSubFlat[i+nz]
# Creating a matrix whose rows are the five diagonals of the matrix of
    the coefficients
    diagonals = np.zeros((5, nx*nz))
    diagonals[0,:] = DMainFlat
    diagonals[1,:] = DFirstSuperFlat
    diagonals[2,:] = DFirstSubFlat
    diagonals[3,:] = DSecondSuperFlat
    diagonals[4,:] = DSecondSubFlat
# Creating the matrix of the coefficients
    A = scipy.sparse.spdiags(diagonals, [0,1,-1,nz,-nz], nx*nz, nx*nz,
        format='csc')
    return A

# Defining the function that solves the system of linear equations for
    a point source in position r=(x0,z00) and returns C(r,r) with AND
    without gaussian filtering
def SolveSparse(A1,nxsolve,nzsolve,x0,z00):
    B = np.zeros((nxsolve,nzsolve))
    B[x0,z00] =1
    b = np.reshape(B, (nxsolve * nzsolve))
    x = scipy.sparse.linalg.spsolve(A1,b)
    Coefficients = np.reshape(x,(nxsolve,nzsolve))
    Coefficients2= gaussian_filter(Coefficients, sigma=(l)/dx,truncate
        =2,mode='nearest')
    CrprimerprimeGaussian = Coefficients2[x0,z00]
    Crprimerprime = Coefficients[x0,z00]
    return [CrprimerprimeGaussian,Crprimerprime]

print(time.perf_counter())
```

```
# Deffining the mean free path
l=300
# Defining the size of the plate in z(h) and x(w) direction
h, w = 6*l, 6*l
# Indicate the value of z0 (with respect to l)
z0 = (2/3)*l
# Initial diffusion coefficient (assuming v_E=c)
D=1.5*(10**8)*l
print(D)
# size of the grids in x-, z- directions, mm
dx, dz = 0.2*l, 0.2*l
# stating the number of grids in each direction x and z
nz, nx = int(h/dz) , int(w/dx)
# Wavenumber
k=0.1
# Defining kl
kl = k*l
# Defining a matrix for the initial (position-independent) Boltzmann
    diffusion coefficient
D00 = D * np.ones((nx, nz))
tempo1 = time.perf_counter()
print(time.perf_counter())

# Creating two matrices that represent the (calculated) position-
    dependent diffusion coefficient (see loop below)
DNewFiltered, DOldFiltered = D00, D00
# Creating the counter for the number of loops and an initial
    arbitrarily large value for the loop condition (to guarantee that
    the loop continues after the first loop)
number, MaxDifference = 0, 1e10

# starting a loop to calculate the matrix C(r,r)
while MaxDifference>1e-5:
# Calculating the matrix of the coefficients for the position-dependent
     diffusion coefficient calculated in the previous iteration
    MatrixCoeff = New_Coefficients(nz,nx,z0,DNewFiltered)
# Calculating C(r,r) for 1/4 of the plate, P.S: In this version of the
    code C(r,r) is calculated for 1/4 of the plate and the result is
    reflected to obtain the final C(r,r), due to symmetry of the system
    ReturnCoeff = joblib.Parallel(n_jobs=6,max_nbytes='100M')(joblib.
        delayed(SolveSparse)(MatrixCoeff,nx,nz,k,l) for k in range(int(
        nx/2),nx) for l in range(int(nz/2)))
```

```
# Creating the arrays that will represent C(r,r) filtered and not
    filtered
    ReturnArrFiltered, ReturnArr = [], []
    for i in ReturnCoeff:
        ReturnArrFiltered.append(i[0])
        ReturnArr.append(i[1])
    ReturnArrFiltered = np.array(ReturnArrFiltered)
    ReturnArr = np.array(ReturnArr)
# Reflecting the calculated C(r,r), for 1/4 of the plate to obtain the
    full matrix
    CoefficientsFinalFiltered = np.reshape(ReturnArrFiltered,(int(nx/2)
        ,int(nz/2)))
    CoefficientsFinal = CoefficientsFinalFiltered.copy()
    CoefficientsFinal0 = np.flip(CoefficientsFinal,0)
    CoefficientsFinalHalf=np.concatenate((CoefficientsFinal0,
        CoefficientsFinal),axis=0)
    CoefficientsFinalSecondHalf = np.flip(CoefficientsFinalHalf,1)
    CoefficientsFinalTotal=np.concatenate((CoefficientsFinalHalf,
        CoefficientsFinalSecondHalf),axis=1)
# Calculating the position-dependent diffusion coefficient
    DNewFiltered = np.divide((kl)*D00,kl+(4*np.multiply(D00,
        CoefficientsFinalTotal)))
# Calculating the diffusion coefficient in the borders of the sample
    for i in range(0,int((l)/dx)+1):

        DNewFiltered[int((l)/dx)-i,:] = 2*DNewFiltered[int((l)/dx)-i
            +1,:]-DNewFiltered[int((l)/dx)-i+2,:]
        DNewFiltered[:,int((l)/dx)-i] = 2*DNewFiltered[:,int((l)/dx)-i
            +1]-DNewFiltered[:,int((l)/dx)-i+2]
        DNewFiltered[nx-1-int((l)/dx)+i,:] = 2*DNewFiltered[nx-2-int((l)
            /dx)+i,:]-DNewFiltered[nx-3-int((l)/dx)+i,:]
        DNewFiltered[:,nz-1-int((l)/dx)+i] = 2*DNewFiltered[:,nz-2-int((
            l)/dx)+i]-DNewFiltered[:,nz-3-int((l)/dx)+i]
# Calculating a matrix that represents the difference between the
    diffusion coefficient calculated in the present iteraction and the
    previous one (excluding the borders)
    Difference = DOldFiltered[int((l)/dx)+1:-(int((l)/dx)+1),int((l)/dx
        )+1:-(int((l)/dx)+1)] -DNewFiltered[int((l)/dx)+1:-(int((l)/dx)
        +1),int((l)/dx)+1:-(int((l)/dx)+1)]
# Retrieving the maximum difference
    MaxDifference = np.amax(abs(Difference[:,:]))
# Calculating the position of the maximum difference
```

```
    indices = np.where(Difference == MaxDifference)
# Calculating the ratio between the maximum difference and the
    diffusion coefficient (in the same position) calculated in the
    previous loop
    MaxDifference = MaxDifference/DOldFiltered[indices[0][0],indices
        [1][0]]
# Redefining the diffusion coefficient (in the same position)
    calculated in the previous loop
    DOldFiltered =DNewFiltered
    number = number+1
    print(number)
    print(MaxDifference)
    print(DNewFiltered[indices[0][0],indices[1][0]]/D)



print(time.perf_counter())
tempo2 = time.perf_counter()
print('dt=',tempo2-tempo1)
print('Max', np.max(DNewFiltered)/D)
print('Min', np.min(DNewFiltered)/D)

# saving the matrix of the position-dependent diffusion coefficient
np.savetxt("DiffusionCoefficients"+str(kl)+".csv", DNewFiltered,
    delimiter=",")

# Plotting the heatmap of the obtained diffusion coefficient, divided
    by the Boltzmann (position-independent) diffusion coefficient.
heatmap2d(DNewFiltered/D)
del z0,D,D00
gc.collect()
```

References

1. P. W. Anderson, "Absence of diffusion in certain random lattices," *Phys. Rev.* 109, 1492–1505 (1958).
2. A.F. Ioffe and A.R. Regel, in Progress in Semiconductors, edited by A. F. Gibson, Vol. 4 (Wiley, New York, 1960), pp. 237–291.
3. H. Hu, A. Strybulevych, J. H. Page, S. E. Skipetrov, and B. A. van Tiggelen, "Localization of ultrasound in a three-dimensional elastic network," *Nat. Phys.* 4(12), 945–948 (2008).
4. S. S. Kondov, W. R. McGehee, and J. J. Zirbel, et al., "Three-dimensional Anderson localization of ultracold matter," *Science* 334(6052), 66–68 (2011).
5. F. Jendrzejewski, A. Bernard, and K. Müller, et al., "Three-dimensional localization of ultracold atoms in an optical disordered potential," *Nat. Phys.* 8(5), 398–403 (2012).
6. G. Roati, C. D'Errico, L. Fallani, M. Fattori, C. Fort, M. Zaccanti, G. Modugno, M. Modugno, and M. Inguscio, "Anderson localization of a non-interacting Bose-Einstein condensate," *Nature* 453(7197), 895–898 (2008).
7. J. Chabé, G. Lemarié, and B. Grémaud, et al., "Experimental observation of the Anderson metal-insulator transition with atomic matter waves," *Phys. Rev. Lett.* 101(25), 255702 (2008).
8. E. Abrahams, P. W. Anderson, and D. C. Licciardello, et al., "Scaling theory of localization: absence of quantum diffusion in two dimensions," *Phys. Rev. Lett.* 42(10), 673–676 (1979).
9. S. John, "Electromagnetic absorption in a disordered medium near a photon mobility edge," *Phys. Rev. Lett.* 53, 2169–2172 (1984).
10. P. W. Anderson, "The question of classical localization: a theory of white paint?" *Philos. Mag.* 52(3), 505–509 (1985).
11. D. S. Wiersma, P. Bartolini, A. Lagendijk, and R. Righini, "Localization of light in a disordered medium," *Nature* 390(6661), 671–673 (1997).
12. F. Scheffold, R. Lenke, R. Tweer, and G. Maret, "Localization or classical diffusion of light?" *Nature* 398(6724), 206–207 (1999).
13. T. Van Der Beek, P. Barthelemy, P. M. Johnson, D. S. Wiersma, and A. Lagendijk, "Light transport through disordered layers of dense gallium arsenide submicron particles," *Phys. Rev. B* 85, 115401 (2012)
14. . M. Störzer, P. Gross, and C. M. Aegerter, et al., "Observation of the critical regime near Anderson localization of light," *Phys. Rev. Lett.* 96(6), 063904 (2006).
15. S. John, "Strong localization of photons in certain disordered dielectric superlattices," *Phys. Rev. Lett.* 58(23), 2486–2489 (1987).
16. T. Sperling, W. Buhrer, C. Aegerter, and G. Maret, "Direct determination of the transition to localization of light ¨ in three dimensions," Nat. Photonics 7, 48 (2013).
17. F. Scheffold and D. Wiersma, "Inelastic scattering puts in question recent claims of Anderson localization of light," *Nat. Photonics* 7, 934 (2013).
18. T. Sperling, L. Schertel, M. Ackermann, et al., "Can 3D light localization be reached in 'white paint'?" *New J. Phys.* 18(1), 013039 (2016).
19. S. E. Skipetrov and I. M. Sokolov, "Absence of Anderson localization of light in a random ensemble of point scatterers," *Phys. Rev. Lett.* 112, 023905 (2014).
20. S. E. Skipetrov and I. M. Sokolov, "Magnetic-Field-Driven Localization of Light in a Cold-Atom Gas," *Phys. Rev. Lett.* 114(5), 053902 (2015).
21. Skipetrov, S. E. "Localization transition for light scattering by cold atoms in an external magnetic field." *Phys. Rev. Lett.* 121, 093601 (2018).
22. L. G. Celardo, M. Angeli, F. Mattiotti, R. Kaiser, "Localization of light in three dimensions: A mobility edge in the imaginary axis in non-Hermitian Hamiltonians," *Europhys. Lett.* 145, 35002 (2024).
23. C. E. Wieman and L. Hollberg, "Using diode lasers for atomic physics," *Rev. Sci. Instrum.* 62(1), 1–20 (1991).
24. T. Kurosu and F. Shimizu, "Laser cooling and trapping of calcium and strontium," *Jpn. J. Appl. Phys.* 29, L2127-L2129 (1990).

25. K. Sengstock, K. Sterr, J.H. Müller, V. Rieger, D. Bettermann, and W. Ertmer, "Optical Ramsey spectroscopy on laser-trapped and thermal Mg atoms," *Appl. Phys. B* 59, 99–115 (1994).
26. J. R. Guest, N. D. Scielzo, I. Ahmad, K. Bailey, J. P. Greene, R. J. Holt, Z.-T. Lu, T. P. O'Connor, and D. H. Potterveld, "Laser Trapping of ^{225}Ra and ^{226}Ra with Repumping by Room-Temperature Blackbody Radiation," *Phys. Rev. Lett.* 98, 093001 (2007).
27. S. De, U. Dammalapati, K. Jungmann, and L. Willmann, "Magneto-optical trapping of barium," *Phys. Rev. A* 79, 041402(R) (2009).
28. K. Honda, Y. Takahashi, T. Kuwamoto, M. Fujimoto, K. Toyoda, K. Ishikawa, and T. Yabuzaki,"Magneto-optical trapping of Yb atoms and a limit on the branching ratio of the $^1P_1$ state," *Phys. Rev. A* 59, R934(R) (1999).
29. K. R. Vogel, T. P. Dinneen, A. Gallagher, and J. L. Hall, "Narrow-line Doppler cooling of strontium to the recoil limit," *IEEE Trans. Instrum. Meas.* 48(2), 618–621 (1999).
30. A. Guttridge, S. A. Hopkins, S. L. Kemp, D. Boddy, R. Freytag, M. P. A. Jones, M. R. Tarbutt, E. A. Hinds, and S. L. Cornish, "Direct loading of a large Yb MOT on the $^1S_0 \rightarrow {}^3P_1$ transition," *J. Phys. B: At. Mol. Opt. Phys.* 49 145006 (2016).
31. J. P. Covey, A. Sipahigil, S. Szoke, N. Sinclair, M. Endres, and O. Painter, "Telecom-Band Quantum Optics with Ytterbium Atoms and Silicon Nanophotonics," *Phys. Rev. Applied* 11, 034044 (2019).
32. Takasu, Y.; Honda, K.; Komori, K.; Kuwamoto, T.; Kumakura, M.; Takahashi, Y.; Yabuzaki, T. "High-Density Trapping of Cold Ytterbium Atoms by an Optical Dipole Force," *Phys. Rev. Lett.* 2003, 90, 023003.
33. Scholl, M. "Probing an ytterbium Bose-Einstein condensate using an ultranarrow optical line : towards artificial gauge fields in optical lattices," *PhD Thesis.* Université Pierre et Marie Curie - Paris 6 (2014).
34. R. W. P. Drever, J. L. Hall, F. V. Kowalski, J. Hough, G. M. Ford, A. J. Munley, and H. Ward, "Laser phase and frequency stabilization using an optical resonator." *Appl. Phys. B* 31, 97–105 (1983).
35. R. V. Pound, "Electronic Frequency Stabilization of Microwave Oscillators." *Rev. Sci. Instrum.* 17(11), 490–505 (1946).
36. C. Cahillane and G. Mansell, "Review of the advanced LIGO gravitational wave observatories leading to observing run four." *Galaxies* 10, 36 (2022).
37. E. D. Black, "An introduction to Pound–Drever–Hall laser frequency stabilization," *Am. J. Phys.* 69(1), 79–87 (2001).
38. T. W. Hänsch and B. Couillaud, "Laser frequency stabilization by polarization spectroscopy of a reflecting reference cavity," *Opt. Commun.* 35, 441–444 (1980).
39. R.C. Jones, "New calculus for the treatment of optical systems: VIII. Electromagnetic theory," *J. Opt. Soc. Am.* 46, 126-131 (1956).
40. J. C. Bergquist, H. Hemmati, and W. M. Itano, "High power second harmonic generation of 257 nm radiation in an external ring cavity," *Opt. Comm.* 43, 437–442 (1982).
41. G. C. Bjorklund, "Frequency-modulation spectroscopy: a new method for measuring weak absorptions and dispersions," *Opt. Lett.* 5(1), 15–17 (1980).
42. G. C. Bjorklund, M. D. Levenson, W. Lenth, and C. Ortiz, "Frequency modulation (FM) spectroscopy: Theory of lineshapes and signal-to-noise analysis," *Appl. Phys. B* 32(3), 145–152 (1983).
43. G. Camy, Ch. Borde, and M. Ducloy, "Hererodyne saturation spectroscopy through frequency modulation of the saturating beam," Opt. Commun. 41, 325 (1982)
44. M.Ducloy, D.Bloch, "Theory of degenerate four-wave mixing in resonant Doppler-broadened media.- II. Doppler-free heterodyne spectroscopy via collinear four-wave mixing in two- and three-level systems," *J.Phys. France* 43,57(1982).
45. M. Ducloy and D. Bloch, "Theory of degenerate four-wave mixing in resonant doppler-broadened systems - i. angular dependence of intensity and lineshape of phase-conjugate emission," *J.Phys. France* 42, 711–721 (1981).
46. Boyd, R.W.: Nonlinear Optics, 3rd edn. Academic Press, Boston (2008).
47. Abramowitz, M. and Stegun, I. A., Handbook of Mathematical Functions (Dover, New York) 1965, p. 297-329.

48. J. H. Shirley, "Modulation transfer processes in optical heterodyne saturation spectroscopy," *Opt. Lett.* 7, 537-539 (1982).
49. J. J. Snyder, R. K. Raj, D. Bloch, et al., "High-sensitivity nonlinear spectroscopy using a frequency-offset pump," *Opt. Lett.* 5(4), 163–165 (1980).
50. F. D. Valle, E. Milotti, A. Ejlli, U. Gastaldi, G. Messineo, L.Piemontese, G. Zavattini, R. Pengo, and G. Ruoso, "Extremely long decay time optical cavity," *Opt. Express* 22, 11570 (2014).
51. H. Letellier, Á. M. G. de Melo, A. Dorne, and R. Kaiser, "Loading of a large Yb MOT on the 1S0 →1 P1 transition," *Rev. Sci. Instrum.* 94, 123203 (2023).
52. J. Lee, J. H. Lee, J. Noh, and J. Mun, "Core-shell magneto-optical trap for alkaline-earth-metal-like atoms," *Phys. Rev. A* 91, 053405 (2015).
53. E. L. Raab, M. Prentiss, A. Cable, S. Chu, and D. E. Pritchard, "Trapping of neutral sodium atoms with radiation pressure," *Phys. Rev. Lett.* 59, 2631–2634 (1987).
54. C.-W. Chou, J. Laurat, H. Deng, K. S. Choi, H. D. Riedmatten, D.Felinto, and H. J. Kimble, "Functional quantum nodes for entanglement distribution over scalable quantum networks," *Science* 316, 1316–1320 (2007).
55. X. Wu, Z. Pagel, B. S. Malek, T. H. Nguyen, F. Zi, D. S. Scheirer, and H. Müller, "Gravity surveys using a mobile atom interferometer," *Sci. Adv.* 5(9), eaax0800 (2019).
56. Q. Bodart, S. Merlet, N. Malossi, F. Pereira Dos Santos, P. Bouyer, and A. Landragin, "A cold atom pyramidal gravimeter with a single laser beam," *Appl. Phys. Lett.* 96, 134101 (2010).
57. M. H. Anderson, J.R. Ensher, M.R. Matthews, C. E. Weiman, and E. A. Cornell, "Observation of Bose-Einstein condensation in a dilute atomic vapor," *Science* 269(5221), 198–201 (1995).
58. K. D. Davis, M. O. Mewes, M. R. Andrews, N. J. vanDruten, D. S. Durfee, D. M. Kurn, and W. Ketterle, "Bose-Einstein condensation in a gas of sodium atoms," *Phys. Rev. Lett.* 75(22), 3969–3973 (1995).
59. T. Walker, D. Sesko, and C. Wieman, "Collective Behavior of Optically Trapped Neutral Atoms," *Phys. Rev. Lett.* 64, 408-411 (1990).
60. T. W. Hänsch and A. L. Schawlow, "Cooling of gases by laser radiation," *Opt. Commun.* 13(1), 68–69 (1975)
61. A. Ashkin, "Atomic-beam deflection by resonance-radiation pressure," *Phys. Rev. Lett.* 25(19), 1321–1324 (1970)
62. P. D. Lett, W. D. Phillips, S. L. Rolston, C. E. Tanner, R. N. Watts, and C. I. Westbrook, "Optical molasses," *J. Opt. Soc. Am. B* 6(11), 2084 (1989).
63. Jean Dalibard, "Une brève histoire des atomes froids," Collège de France (2015).
64. W. D. Phillips and H. Metcalf, "Laser deceleration of an atomic beam," *Phys. Rev. Lett.* 48(9), 596–599 (1982).
65. Álvaro Mitchell Galvão de Melo, "Forward four-wave mixing via recoil-induced resonances in cold cesium atoms," *Master's thesis*, Federal University of Pernambuco (2019).
66. D. W. Sesko, T. G. Walker, and C. E. Wieman, "Behavior of neutral atoms in a spontaneous force trap," *J. Opt. Soc. Am. B* 8, 946–958 (1991).
67. J. Dalibard, "Atomes ultra-froids," Lecture Notes (ENS, Paris, 2006).
68. H. Letellier. "Piégeage magnéto-optique de l'ytterbium sur la transition 1S0 → 1P1," PhD Thesis. Université Côte d'Azur (in preparation).
69. T. Loftus, J.R. Bochinski, R. Shivitz, T.W. Mossberg, "Power-dependent loss from an ytterbium magneto-optic trap," *Phys. Rev. A* 61, 051401 (2000)
70. U. D. Rapol, A. Krishna, A. Wasan, and V. Natarajan, "Laser cooling and trapping of Yb from a thermal source," *Eur. Phys. J. D* 29, 409 (2013).
71. Zhao P, Xiong Z, Liang J, He L and Lü B, "Magneto-Optical Trapping of Ytterbium Atoms with a 398.9 nm Laser," *Chin. Phys. Lett.* 25, 3631 (2008).
72. Junia Nomura, Tomohiko Momma, Yuki Kojima, Yusuke Hisai, Takumi Kobayashi, Daisuke Akamatsu and Feng-Lei Hong, "Direct loading of Yb atoms into a 3D magneto-optical trap from a dispenser atomic source," *AIP Advances* 13 (2) 025361 (2023).
73. E. Wodey, R.J. Rengelink, C. Meiners, E.M. Rasel and D. Schlippert, "A robust, high-flux source of

laser-cooled ytterbium atoms," *J. Phys. B: At. Mol. Opt. Phys.* 54 (2021) 035301.

74. A. Jayakumara, B. Plotkin-Swing, A. O. Jamison, and S. Gupta, "Dual-axis vapor cell for simultaneous laser frequency stabilization on disparate optical transitions," *Review of Scientific Instruments* 86, 073115 (2015).
75. Feihu Cheng, Ke Deng, Kui Liu, Hongli Liu, Jie Zhang, and Zehuang Lu, "Absolute frequency measurement of molecular iodine hyperfine transition at 534 nm," *J. Opt. Soc. Am. B* 36, 1816-1822 (2019).
76. Yu-Chen Hsiao, Cheng-Yang Kao, Hsuan-Chen Chen, Shih-En Chen, Jin-Long Peng, and Li-Bang Wang, "Absolute frequency measurement of the molecular iodine hyperfine transitions at 548 nm," *J. Opt. Soc. Am. B* 30, 328-332 (2013).
77. Y.T. Chen, N.C. Xin, H.R. Qin, S.N. Miao, Y. Zheng, J.W. Zhang, L.J. Wang, "Absolute frequency measurement of molecular iodine hyperfine transitions at 554 nm and its application to stabilize a 369 nm laser for Yb+ ions cooling," *Chinese Journal of Physics* 88, 485-492 (2024).
78. Feng-Lei Hong, Hajime Inaba, Kazumoto Hosaka, Masami Yasuda, and Atsushi Onae, "Doppler-free spectroscopy of molecular iodine using a frequency-stable light source at 578 nm," *Opt. Express* 17, 1652-1659 (2009).
79. Hao Wu, Pengfei Lu, Yang Liu, Jiangyong Hu, Qifeng Lao, Xinxin Rao, Lunhua Deng, Feng Zhu, and Le Luo, "Frequency stabilization of a 739 nm laser to an I2 spectrum for trapped ytterbium ions," *J. Opt. Soc. Am. B* 39, 1457-1461 (2022).
80. P. Cancio Pastor, P. Zeppini, A. Arie, P. De Natale, G. Giusfredi, G. Rosenman, and M. Inguscio, "Sub-Doppler spectroscopy of molecular iodine around 541 nm with a novel solid state laser source," *Opt. Commun.* 176, 453–458 (2000).
81. G. Galzerano, F. Bertinetto, and E. Bava, "Characterization of the modulation transfer spectroscopy method by means of He-Ne lasers and 127I2 absorption lines at λ = 612 nm," *Metrologia* 37, 149–154 (2000).
82. Yao-Chin Huang, Hsuan-Chen Chen, Shih-En Chen, Jow-Tsong Shy, and Li-Bang Wang, "Precise frequency measurements of iodine hyperfine transitions at 671 nm," *Appl. Opt.* 52, 1448-1452 (2013).
83. A. Dareau, "Manipulation cohérente d'un condensat de Bose-Einstein d'ytterbium sur la transition "d'horloge" : de la spectroscopie au magnétisme artificiel," PhD Thesis. École Normale Superieure (2015).
84. Yuto Tanabe, Yuma Sakamoto, Takuya Kohno, Daisuke Akamatsu, and Feng-Lei Hong, "Frequency references based on molecular iodine for the study of Yb atoms using the 1S0 – 3P1 intercombination transition at 556 nm," *Opt. Express* 30, 46487-46500 (2022)
85. Álvaro M. G. de Melo, Hector Letellier, Apoorva Apoorva, Antoine Glicenstein, and Robin Kaiser, "Laser frequency stabilization by modulation transfer spectroscopy and balanced detection of molecular iodine for laser cooling of 174Yb," *Opt. Express* 32, 6204-6214 (2024)
86. P. E. Atkinson, J. S. Schelfhout, and J. J. McFerran, "Hyperfine constants and line separations for the $^1S_0 - ^3P_1$ intercombination line in neutral ytterbium with sub-Doppler resolution," *Phys. Rev. A* 100, 042505 (2019).
87. T. Hori, A. Araya, S. Moriwaki, and N. Mio, "Formulation of frequency stability limited by laser intrinsic noise in feedback systems," *Appl. Opt.* 48, 429-435 (2009).
88. M. Aldous, J. Woods, A. Dragomir, R. Roy, and M. Himsworth, "Carrier frequency modulation of an acousto-optic modulator for laser stabilization," *Opt. Express* 25, 12830-12838 (2017).
89. H. Fang, S.C. Wang, and J. Shy, "Pressure and power broadening of the a10 component of R(56) 32-0 transition of molecular iodine at 532nm," *Opt. Commun.* 257, 76–83 (2006).
90. L.-S. Ma, J. Ye, P. Dubé, and J. L. Hall, "Ultrasensitive frequency-modulation spectroscopy enhanced by a high-finesse optical cavity: theory and application to overtone transitions of C2H2 and C2HD," *J. Opt. Soc. Am. B* 16(12), 2255–2268 (1999).
91. F. Riehle, "Frequency Standards," *John Wiley & Sons Ltd.* (2003).
92. G. Di Domenico, S. Schilt, and P. Thomann, "Simple approach to the relation between laser frequency noise and laser line shape," *Appl. Opt.* 49(25), 4801–4807 (2010).
93. Q. Zhou, J. Qin, W. Xie, Z. Liu, Y. Tong, Y. Dong, and W. Hu, "Power-area method to precisely

estimate laser linewidth from its frequency-noise spectrum," *Appl. Opt.* 54(28), 8282–8289 (2015).
94. L. Turner, K. Weber, C. Hawthorn, and R. Scholten, "Frequency noise characterisation of narrow linewidth diode lasers," *Opt. Commun.* 201, 391–397 (2002).
95. *Private communication.*
96. G. E. Obarski and J. D. Splett, "Transfer standard for the spectral density of relative intensity noise of optical fiber sources near 1550 nm," *J. Opt. Soc. Am. B* 18, 750–761 (2001).
97. Obarski, G. and Hale, P. (1999), "How to Measure Relative Intensity Noise in Lasers", *Laser Focus World* (Accessed March 29, 2024).
98. G. Agrawal, "Noise in semiconductor lasers and its impact on optical communication systems," *SPIE Laser Noise* 1376, 224–235 (1990).
99. U. Eismann, M. Enderlein, K. Simeonidis, F. Keller, F. Rohde, D. Opalevs, M. Scholz, W. Kaenders, and J. Stuhler, "Active and passive stabilization of a high-power UV frequency-doubled diode laser," Conference on Lasers and Electro-Optics, OSA Technical Digest (online) (Optica Publishing Group, 2016), paper JTu5A.65.
100. D. W. Allan, "Statistics of atomic frequency standards," Proceedings of the IEEE, vol. 54, no. 2, pp. 221-230 (1966).
101. D. A. Howe, D. U. Allan, and J. A. Barnes, "Properties of Signal Sources and Measurement Methods," in Proceedings of the 35th Annual Frequency Control Symposium (IEEE, 1981), pp. 669–716.
102. W. Riley, P. L. U. Time, and F. Division, "Handbook of Frequency Stability Analysis," NIST special publication (U.S.Department of Commerce, National Institute of Standards and Technology, 2008).
103. C. E. Shannon, "Communication in the presence of noise," *Proc. IRE*, vol. 37, no. 1, pp. 10–21, 1949.
104. W. Guerin, M. Rouabah, and R. Kaiser, "Light interacting with atomic ensembles: collective, cooperative and mesoscopic effects," *J. Mod.Opt.* 64, 895–907 (2017).
105. G. Labeyrie, F. Michaud, and R. Kaiser, "Self-sustained oscillations in a large magneto-optical trap," *Phys. Rev. Lett.* 96, 023003 (2006).
106. M. Gaudesius, R. Kaiser, G. Labeyrie, Y.-C. Zhang, and T. Pohl, "Instability threshold in a large balanced magneto-optical trap," *Phys. Rev. A* 101, 053626 (2020).
107. M. Gaudesius, Y.-C. Zhang, T. Pohl, R. Kaiser, and G. Labeyrie, "Phase diagram of spatiotemporal instabilities in a large magneto-optical trap," *Phys. Rev. A* 103, L041101 (2021).
108. K. R. Overstreet, P. Zabawa, J. Tallant, A. Schwettmann, and J. P. Shaffer, "Multiple scattering and the density distribution of a Cs MOT," *Opt. Express* 13, 9672-9682 (2005).
109. T.M. Brzozowski, M. Maczynska, M. Zawada, J. Zachorowski, and W. Gawlik, "Time-of-flight measurement of the temperature of cold atoms for short trap-probe beam distances," *J. Opt. B: Quantum Semiclass. Opt.* **4**, 62 (2002).
110. G. Labeyrie, F. de Tomasi, J.-C. Bernard, C. A. Müller, C. Miniatura, and R. Kaiser, "Coherent Backscattering of Light by Cold Atoms," *Phys. Rev. Lett.* 83, 5266 (1999).
111. M. O. Araújo, I. Krešić, R. Kaiser, and W. Guerin, "Superradiance in a Large and Dilute Cloud of Cold Atoms in the Linear-Optics Regime," *Phys. Rev. Lett.* 117, 073002 (2016).
112. M. Drewsen, P. H. Laurent, A. Nadir, G. Santarelli, A. Clairon, Y. Castin, D. Grison, and C. Salomon, "Investigation of sub-Doppler cooling effects in a cesium magneto-optical trap," *Appl. Phys. B* 59, 283–298 (1994).
113. T. Chanelière, J. Meunier, R. Kaiser, C. Miniatura, and D. Wilkowski, "Extra-heating mechanism in Doppler cooling experiments," *J. Opt. Soc. Am. B* 22, 1819-1828 (2005).
114. J. Höschele, S. Buob, A. Rubio-Abadal, V. Makhalov, and L. Tarruell, "Atom-Number Enhancement by Shielding Atoms From Losses in Strontium Magneto-Optical Traps," *Phys. Rev. Applied* 19, 064011 (2023).
115. K. Pandey, A. K. Singh, P. V. Kiran Kumar, M. V. Suryanarayana, and V. Natarajan, "Isotope shifts and hyperfine structure in the 555.8-nm $^1S_0 \rightarrow {}^3P_1$ line of Yb," *Phys. Rev. A* 80, 022518 (2009).
116. D. Das, A. Banerjee, S. Barthwal, and V. Natarajan, "A rubidiumstabilized ring-cavity resonator for optical frequency metrology: precise measurement of the D1 line in 133Cs," *Eur. Phys. J. D* 38, 545–552 (2006).
117. A.D. Innes, P.Majumder, H.R. Noh, and S.L. Cornish, "Modulation transfer spectroscopy of the D_1

transition of potassium: theory and experiment," *J. Phys. B: At. Mol. Opt. Phys.* 57 075401 (2024).
118. S. Gerstenkorn, P. Luc, J. Verges, and J. Chevillard, *Atlas Du Spectre d'absorption de La Molécule d'iode,* Atlas Du Spectre d'absorption de La Molécule d'iode No. vol. 1 (Laboratoire Aimé Cotton, 1978).
119. H. Kim, M.-S. Heo, C. Y. Park, D.-H. Yu and W. K. Lee, "Absolute frequency measurement of the 171Yb optical lattice clock at KRISS using TAI for over a year," *Metrologia*, 58, 055007 (2021).
120. M. E. Wickliffe, J. E. Lawler, and G. Nave, "Atomic transition probabilities for Dy I and Dy II," *J. Quant. Spectrosc. Radiat. Transf.* 66, 363–404 (2000).
121. P. Ilzhöfer, G. Durastante, A. Patscheider, et al., "Two-species five-beam magneto-optical trap for erbium and dysprosium," *Phys. Rev. A* 97(2), 023633 (2018).
122. Cottier, F.; Cipris, A.; Bachelard, R.; Kaiser, R. "Microscopic and macroscopic signatures of 3D Anderson localization of light," *Phys. Rev. Lett.* 2019, 123, 083401.
123. H. de Raedt, A. Lagendijk, and P. de Vries, "Transverse localization of light," *Phys. Rev. Lett.* 62(1), 47–50 (1989).
124. R. Lehmberg, "Radiation from an N-atom system. I. General formalism," *Phys. Rev. A* 2(3), 883–888 (1970).
125. Vollhardt, D, and P. Wölfle (1980), "Diagrammatic, selfconsistent treatment of the anderson localization problem in d $\leq$ 2 dimensions," *Phys. Rev. B* 22, 4666–4679.
126. B. A. van Tiggelen, A. Lagendijk, and D. S. Wiersma, "Reflection and transmission of waves near the localization threshold," *Phys. Rev. Lett.* 84, 4333–4336 (2000).
127. B. Payne, A. Yamilov, and S. E. Skipetrov, "Anderson localization as position-dependent diffusion in disordered waveguides," Phys. Rev. B 82, 024205 (2010).
128. Cobus, L. A., Hildebrand, W. K., Skipetrov, S. E., van Tiggelen, B. A. & Page, J. H. "Transverse confinement of ultrasound through the Anderson transition in three-dimensional mesoglasses," *Phys. Rev. B* 98, 214201 (2018).
129. N. Cherroret and S. E. Skipetrov, "Microscopic derivation of self-consistent equations of anderson localization in a disordered medium of finite size," *Phys. Rev. E* 77, 046608 (2008).
130. R. Carminati and J. C. Schotland, Principles of Scattering and Transport of Light (Cambridge University Press, 2021)
131. G. Labeyrie, E. Vaujour, C. A. Muller, D. Delande, C. Miniatura, D. Wilkowski, and R. Kaiser, "Slow Diffusion of Light in a Cold Atomic Cloud," Phys. Rev. Lett. 91, 223904 (2003).
132. C. E. Máximo, N. Piovella, P. W. Courteille, et al., "Spatial and temporal localization of light in two dimensions," *Phys. Rev. A* 92(6), 062702 (2015).
133. A. Lagendijk, B. A. van Tiggelen, and D. S. Wiersma, "Fifty years of anderson localization," *Phys. Today* 62(8), 24–29 (2009).
134. R. L. Weaver, "Anderson localization of ultrasound," *Wave Motion* 12, 129-142 (1990).
135. D. Laurent, O. Legrand, P. Sebbah, C. Vanneste, and F. Mortessagne, "Localized modes in a finite-size open disordered microwave cavity," *Phys. Rev. Lett.* 99(25), 253902 (2007).
136. I. Manai, J.-F. Clément, and R. Chicireanu, et al., "Experimental observation of two-dimensional Anderson localization with the atomic kicked rotor," *Phys. Rev. Lett.* 115(24), 240603 (2015)
137. White, D H, T. A. Haase, D. J. Brown, M. D. Hoogerland, M. S. Najafabadi, J. L. Helm, C. Gies, D. Schumayer, and D. A. W. Hutchinson, "Observation of two-dimensional Anderson localisation of ultracold atoms," *Nature Communications* 11 (1), 4942 (2020).
138. T. Schwartz, G. Bartal, S. Fishman, and M. Segev, "Anderson localization in disordered two-dimensional photonic lattices," *Nature* 446, 52–55 (2007).
139. F. Riboli, P. Barthelemy, S. Vignolini, F. Intonti, A. D. Rossi, S. Combrie, and D. S. Wiersma, "Anderson localization of near-visible light in two dimensions," *Opt. Lett.* 36, 127–129 (2011).
140. Burger, W. & Burge, M. J. Digital Image Processing: An Algorithmic Introduction Using Java (Springer, 2016).
141. Rodger E. Ziemer, William H. Tranter, Principles of communication : systems, modulation, and noise. *Wiley* Seventh edition.
142. Faruque, Saleh. Radio Frequency Modulation Made Easy. *Springer* (2017).